Extracting x rays, γ rays, and relativistic e^-e^+ pairs from supermassive Kerr black holes using the Penrose mechanism

Reva Kay Williams
Department of Astronomy, University of Florida, Gainesville, Florida 32611
(Received 6 August 1993; revised manuscript received 7 October 1994)

Monte Carlo computer simulations of Compton scattering and e^-e^+ pair production processes, in the ergosphere of a supermassive ($\sim 10^8 M_\odot$) rotating black hole, are presented. Particles from an accretion disk surrounding the black hole fall into the ergosphere and scatter off particles that are in bound orbits. In this paper, the equations that govern the orbital trajectory of a particle about a Kerr black hole (KBH) are used to derive analytical expressions for the conserved energy and angular momentum of material and massless particles that have orbits not confined to the equatorial plane. The escape conditions to determine whether or not a particle escapes from the potential well of the KBH are applied to the scattered particles. The Penrose mechanism, in general, allows rotational energy of a KBH to be extracted by scattered particles escaping from the ergosphere to large distances from the black hole. The results of these model calculations, presented in this paper, show that the Penrose mechanism is capable of producing the astronomically observed high energy particles ($\sim$ GeV) emitted by quasars and other active galactic nuclei (AGN). This mechanism can extract hard x-ray and γ-ray photons, from Penrose Compton scatterings of initially low energy UV and soft x-ray photons by target orbiting electrons in the ergosphere; such low energy infalling photons, and high energy scattered escaping photons, are consistent with observations and popular theoretical accretion disk, black hole models. The Penrose pair production processes ($\gamma\gamma \rightarrow e^-e^+$), presented here, allow relativistic e^-e^+ pairs to escape with energies up to $\sim$ 2 GeV; these pairs are produced when infalling low energy photons collide with bound target, highly blueshifted photons at the *photon orbit*. This process may very well be the origin of the relativistic electrons inferred, from observations, to emerge from the cores of AGN. Overall, these Penrose processes can apply to any mass size black hole, more or less, and suggest a complete theory for the extraction of energy from a black hole.

PACS number(s): 97.60.Lf, 95.30.Sf, 98.70.Qy, 98.70.Rz

I. INTRODUCTION

The presence of black holes in nature is a widely accepted concept by the astrophysical community. In particular, they are believed to be the power source of quasars and other active galactic nuclei (AGN), where, in these cases, the black holes are assumed to be supermassive ($M \sim 10^8 M_\odot$). Black holes have been termed by relativists as having "no hair" [1,2]. This means theoretically that black holes can be described at most by three parameters: mass, angular momentum, and electric charge. The term no hair is another way of saying that the black hole has left no evidence as to what the progenitor was prior to its formation—we do not know, for example, in the case of a supermassive black hole, if it were initially a cluster of stars or a single supermassive star. Smaller black holes, say $\sim 15 M_\odot$, are believed to exist also; however, their observational detections are difficult.

A main reason for this difficulty, other than the black hole being isolated, is that hitherto we do not have a developed theory for the extraction of energy from a black hole, a theory that should predict what features are to be detected observationally, features that are intrinsic to the identification of the black hole. In this paper, I present such a theory, with emphasis on the mechanism by which energy is extracted from a rotating black hole, i.e., the Penrose mechanism, and on comparing the resulting energy-momentum spectra, predicted by this model, with observations of celestial objects we believe to be powered by black holes, in particular AGN.

I begin with a discussion of some fundamental characteristics of stellar black holes. The plasma around black holes will be in some dynamical state. Close to the black hole, much of the plasma will presumably be accreting into it. Spherical accretion results if the plasma has no angular momentum; however, if the plasma initially has angular momentum, an accretion disk forms, straddling the equatorial plane of the event horizon. If the black hole has angular momentum, i.e., rotation, referred to as a Kerr black hole (KBH), particles from the accretion disk fall into a region called the ergosphere (meaning energy sphere), before reaching the event horizon.

A mechanism, suggested by Penrose [3], permits rotational energy to be extracted from a KBH. The *classical* Penrose process utilizes the existence of retrograde particle orbits (with respect to the rotation of the KBH) in the ergosphere, for which the energy, as would be measured by an observer at infinity (far away from the KBH), is negative [3,4]. Such orbits do not come out to infinity, because if they did, an observer there would measure a negative energy, which is physically impossible. There-

fore, these negative energy particles never leave the ergosphere. However, it is possible for a particle, say p_1, that has fallen inwardly from infinity into the ergosphere to scatter off another particle, say p_2, initially in a direct orbit in the ergosphere. If the orbit of the scattering particle p_2 changes into a retrograde orbit (of negative energy), then the scattered particle p_1 can escape to infinity with more mass-energy than the sum of the initial energies of p_1 and p_2. Since the orbit of the initially bound particle p_2 is dependent on the angular momentum of the KBH and the curvature of spacetime defined by the mass M of the black hole, then, consequently, when p_2 gives up energy to the escaping particle p_1 and falls into the event horizon, the KBH loses energy in the form of rotational energy. This can be seen in the equation for the mass-energy of a black hole of angular momentum j, which in geometrical units ($G = c = 1$) is

$$M^2 = M_{\rm ir}^2 + \frac{j^2}{4M_{\rm ir}^2} \tag{1.1}$$

[5], where $M_{\rm ir}$ is the irreducible mass. Since $M_{\rm ir}$ can never decrease, but can only increase or remain the same, a decrease in the mass-energy of a KBH can only result from a decrease in its rotational energy.

Another possible class of Penrose processes occurs when particles already inside the ergosphere (say particles belonging to an accretion disk) undergo local relativistic scatterings [6]. Such types are investigated in this paper. If one of the scattering particles is initially in a bound orbit, then it is possible for the other initially unbound scattered particle to escape to infinity with a portion of the rotational energy of the KBH. This process allows scattered ergospheric particles to (1) escape to infinity with more mass-energy than they would have had if the scattering occurred outside the ergosphere and (2) escape to infinity with mass-energy initially trapped by the KBH, mass-energy that possibly had no other way of escaping, save only by processes occurring near the horizon; otherwise, this mass-energy would eventually be accreted onto the black hole.

In this paper, I present model calculations using the Monte Carlo method to treat Penrose processes in the ergosphere of a KBH: for inverse Compton scattering, γ-ray–proton pair production ($\gamma p \rightarrow e^- e^+ p$), and γ-ray–γ-ray pair production ($\gamma\gamma \rightarrow e^- e^+$). These processes are assumed to occur in material falling into the ergospheric region of a rotating black hole from a surrounding accretion disk. (The Monte Carlo method is a technique for obtaining an approximate solution to certain mathematical and physical problems, characteristically involving the replacement of a probability distribution by sample values.) The model calculations presented in this paper require multidimensional integrations for large distributions of particles; such integrations are best done using a computer code based on the Monte Carlo method. For definiteness, a canonical KBH is used, with its limiting value $a/M = 0.998$, as defined in Ref. [7], in the investigation of an accretion disk around a KBH, where a is the angular momentum per unit mass parameter of the KBH. It is found that, if a/M is initially very close to 1 ($0.999 \leq a/M \leq 1$), a small amount of accretion ($\Delta M/M \leq 0.05$) through a disk quickly spins the hole down to a limiting state $a/M \simeq 0.998$. Conversely, if a/M is initially below this limiting value, accretion spins the hole up toward it. Note that, in general, these present calculations show that, using a larger a/M closer to 1 has little effect (if any) on improving the amount of energy that can be extracted.

A Monte Carlo simulation near a KBH, similar to the one presented in this paper, for inverse Compton scattering in the ergosphere [sometimes referred to as *Penrose Compton scattering* (PCS)] was previously computed by Piran and Shaham [4,8–10]. They used equatorial target electrons to calculate emission spectra. Here, I present energy and momentum spectra from using equatorial and nonequatorial targets to show how emitted PCS photons can contribute to the emission spectrum, and how they may acquire the necessary momenta to serve as catalysts for other Penrose processes, which can extract even higher energies (Sec. IV C 2).

A. Inverse Compton scattering

In the PCS process of these present model calculations, photons are emitted from material that has fallen inward from infinity and scatter off tangentially (equatorial or nonequatorial) orbiting electron rings, of completely ionized plasma, revolving near the event horizon. The effects of local thermal random motions superimposed on the orbiting velocity of the electrons are also investigated, to simulate a finite electron temperature. Now, some of the photons, after being scattered by the electrons, eventually escape to infinity. An observer at infinity sees a low-energy (in most cases $< \mu_e$, where μ_e is the electron rest mass-energy) photon being scattered by a direct orbiting electron, after which the photon comes out with a higher energy (inverse Compton scattering). Subsequently, the target electron may recoil to another direct orbit of lesser energy, or the electron may be put on a retrograde orbit of negative energy; in both cases, the target electron gives up energy as measured by an observer at infinity. However, to a particular local frame observer this is just a normal Compton scattering process in which the photon loses energy to the electron, since the photon arrives at the local frame with initial energy higher than $\sim \mu_e$. The infall of the final electron results in an observer at infinity measuring a decrease in the rotational energy of the KBH. This inverse Compton scattering process is different from its flat spacetime counterpart. In the flat spacetime process, cold photons are heated by hot electrons to the temperature of the electrons. In the Penrose process, which occurs in the ergosphere, generally, photons are heated by the rotational energy of the black hole and the curvature of spacetime [4].

B. γ-ray–proton pair production

The model calculations of the $\gamma p \rightarrow e^- e^+ p$ process in the ergosphere proceed along a similar path to that of the

Compton scattering discussed above. The initial conditions of the γ-ray photon are basically the same as for the PCS. Here, however, the photon collides with a proton instead of an electron, and the γ ray must have an initial energy in the local frame greater than $2m_ec^2 = 1.022$ MeV, which is the threshold energy of the $\gamma p \rightarrow e^-e^+p$ reaction. This is the energy needed to form an electron-positron (e^-e^+) pair when a γ ray passes through the Coulomb field of a nucleus of charge eZ. Note that the negatively charged electron will be sometimes referred to as the negatron.

The accretion disk assumed in these calculations is of the form found to occur in Lightman's [11] investigation of a thin, time-dependent disk around a black hole. His calculations showed that as time progress, density and thermal instabilities develop in the thin disk, causing a corona region to form. Astrophysicists call such accretion disks *thin disk/ion corona* models. The ions (p) in the region of instability will have temperatures $T_p \sim 10^{12}$ K, which allow for the existence of γ rays with sufficiently high energies, that are needed for these *Penrose pair production* (PPP) processes to occur. These high energy γ rays will exist because of the following: At $T_p \sim 10^{12}$ K, the most energetic ions will collide with one another resulting in nuclear reactions, which create neutral pions π^0, by the process $p_1p_2 \rightarrow p_1'p_2'\pi^0$ [12,13]. (The threshold energy for this nuclear reaction is 290 MeV; therefore, at $T_p \sim 10^{12}$ K, equivalent to ~ 100 MeV, only particles belonging to the high energy tail of the Maxwellian velocity distribution will undergo such a reaction.) A π^0 subsequently decays into two energetic γ-ray photons, with energies ~ 50 MeV, by the process $\pi^0 \rightarrow \gamma\gamma$ [13].

Now, near the event horizon, at the marginally bound orbit (Sec. III A 1) these γ rays are blueshifted by a factor ~ 30, to energies of the order of the proton rest mass-energy $\simeq 938$ MeV [14]. It has been suggested that energies up to $\sim$ GeV can be extracted from a KBH by this PPP ($\gamma p \rightarrow e^-e^+p$) [12,15], involving these blueshifted γ rays. In this paper, I investigate what happens to the γ rays (~ 50 MeV) resulting from π^0 decays that scatter off initially bound, direct orbiting protons in the ergosphere, thus testing the validity of this suggested process, i.e., to see if this PPP process is a possible source of the relativistic electron fluxes, inferred from the presence of synchrotron radiation in the observations of AGN.

C. γ-ray–γ-ray pair production

This PPP process ($\gamma\gamma \rightarrow e^-e^+$) consists of collisions inside the ergosphere between radially infalling photons and circularly orbiting photons bound at the radius of the *photon orbit* [see Eqs. (2.22) and (2.23)]. If we define the energy of the infalling photon and orbiting photon as $\varepsilon_{\gamma 1}$ and $\varepsilon_{\gamma 2}$, respectively, as measured by a local observer, then an e^-e^+ pair may be created in the collision, provided that

$$\varepsilon_{\gamma 1} + \varepsilon_{\gamma 2} > 2\mu_e \ , \qquad \varepsilon_{\gamma 1}\varepsilon_{\gamma 2} > \mu_e^2 \tag{1.2}$$

[16,17]. The initial energies used in these calculations, as measured by an observer at infinity, for the infalling photon and the orbiting photon, $E_{\gamma 1}$ and $E_{\gamma 2}$, are in the following ranges: 3.5 keV$\leq E_{\gamma 1} \leq$ 1 MeV and 3.4 MeV$\leq E_{\gamma 2} \leq$ 2.146 GeV. These ranges are consistent with those produced by thin disk/ion corona models, as described above. The high energy range for $E_{\gamma 2}$ is chosen based on the expected blueshift in photon energy at the photon orbit. The blueshift factor $e^{-\nu}$ of Eq. (2.8d) at the photon orbit is $\simeq 52$. The γ rays produced in Eilek's hot accretion disk model [12,13], with energies ~ 50 MeV, referred to in Sec. I B, can very well be seed photons, bound at the photon orbit, for these $\gamma\gamma \rightarrow e^-e^+$ reactions [18]. In addition, the PCS processes of this paper show that some of the scattered photons could also be seed particles for these reactions. Moreover, these photon collisions can occur at other radii in addition to the photon orbit, say at a turning point, thereby increasing the probability of collision with another particle; however, such scatterings are not considered here.

Overall, in this paper, I calculate the energy-momentum spectra of the resulting scattered particles produced by the above-described Penrose processes. These energy-momentum spectra are then examined and compared with the observations of AGN. The results of these model calculations show that the Penrose mechanism, occurring in the ergosphere of a supermassive KBH, is capable of producing the necessary high energy spectra observed from AGN. The remaining structure of this paper is as follows. In Sec. II, I present the general formalism, which contains properties of the Kerr metric spacetime, the escape conditions, and the efficiency of the Penrose mechanism. Next, the methods of these Monte Carlo model calculations are presented in Sec. III, and the results are presented in Sec. IV [in this Section, the energy-momentum four-vector (or the four-momentum) components of the scattered escaping particles are presented]. Finally, Sec. V contains a summary, a discussion of how well these results agree with astronomical observations, in particular, of AGN, and Sec. VI contains the conclusions with suggestions for further investigations.

II. GENERAL FORMALISM

A. The Kerr metric

The Kerr metric [19], a stationary, axially symmetric, asymptotically flat spacetime solution to the vacuum Einstein field equations, describes the geometry outside of a rotating massive body. This metric can be used to define the spacetime separation between events near a rotating (Kerr) black hole. The Kerr metric written in Boyer-Lindquist coordinates [20] and in geometrical units ($G = c = 1$) is

$$ds^2 = -\left(1 - \frac{2Mr}{\Sigma}\right) dt^2 - \frac{4Mar \sin^2 \Theta}{\Sigma} dt\, d\Phi + \frac{\Sigma}{\Delta} dr^2 + \Sigma d\Theta^2 + \left(r^2 + a^2 + \frac{2Ma^2 r \sin^2 \Theta}{\Sigma}\right) \sin^2 \Theta d\Phi^2 , \tag{2.1a}$$

or, in component notation,

$$ds^2 = g_{tt} dt^2 + g_{t\Phi} dt\, d\Phi + g_{rr} dr^2 + g_{\Theta\Theta} d\Theta^2 + g_{\Phi\Phi} d\Phi^2 , \tag{2.1b}$$

where a is the angular momentum per unit mass parameter and M is the mass of the black hole. Σ and Δ are defined by

$$\Delta \equiv r^2 - 2Mr + a^2 \tag{2.2}$$

and

$$\Sigma \equiv r^2 + a^2 \cos^2 \Theta , \tag{2.3}$$

respectively. In general, the parameter a can have values $0 \leq (a/M) \leq 1$, values which allow for the existence of an event horizon. For a KBH, the event horizon is located at $r = r_+ = M + (M^2 - a^2)^{1/2}$, the larger root of the equation $\Delta = 0$. When $a = 0$, Eq. (2.1) reduces to the form of the Schwarzschild metric for a nonrotating massive body. Then $\Delta = 0$ gives the event horizon known as the Schwarzschild or gravitational radius.

Upon approaching a KBH from infinity, a limit or a region is reached where the angular momentum of the KBH causes inertial frames to be dragged around in the direction that the black hole rotates. That is, it is impossible for an observer inside this so-called stationary limit to remain at rest relative to distant observers. This limit is characterized by the vanishing of the g_{tt} component in Eq. (2.1):

$$g_{tt} = -\left(1 - \frac{2Mr}{\Sigma}\right) = 0 . \tag{2.4}$$

More precisely, the stationary limit is the larger root of g_{tt}, given analytically by

$$r = r_0 = M + (M^2 - a^2 \cos^2 \Theta)^{1/2} . \tag{2.5}$$

The region between this stationary limit and the event horizon is called the ergosphere.

Inside the ergosphere, the Kerr metric in the Boyer-Lindquist coordinate frame (BLF) does not allow an observer to be stationary (in the sense of the observer being at rest with r, Θ, Φ = const) because of the dragging of inertial frames. Moreover, physical processes are difficult to describe in the BLF, because (1) for physical observers inside the ergosphere, the dragging of inertial frames becomes so severe that the time coordinate basis vector changes from timelike to spacelike and (2) the nondiagonal Kerr metric characteristically introduces algebraic complexity when raising and lowering tensor indices. In order to examine physical processes inside the ergosphere, Bardeen, Press, and Teukolsky [21] devised a frame of reference called the local nonrotating frame (LNRF). Observers in this frame rotate with the KBH in such a way that the frame dragging effect of the rotating black hole is canceled as much as possible. In the LNRF, special relativity applies since locally spacetime has Lorentz or flat spacetime geometry. That is, one can use the LNRF as a convenient inertial frame to describe physical processes inside the ergosphere.

On the other hand, it is better to use the BLF when describing the general orbits of particles (including photons) near the KBH. The BLF admits three constants of motion as measured by an observer at infinity [22]. In terms of the covariant components of the particles four-momentum $[P_\mu = (P_r, P_\Theta, P_\Phi, P_t); (\mu = r, \Theta, \Phi, t)]$ at some instant of time, the conserved quantities are

$E = -P_t \equiv$ total energy ,

$L = P_\Phi \equiv$ component of the angular momentum parallel to the symmetry axis ,

and

$$Q = P_\Theta^2 + \cos^2 \Theta \left[a^2(\mu_0^2 - E^2) + \frac{L^2}{\sin^2 \Theta}\right] , \tag{2.6}$$

where μ_0 is the rest mass-energy of the particle, which is a trivial fourth constant of motion. The value of Q is zero for particles whose motions are confined to the equatorial plane. The nonzero values of Q belong to particles which are moving in the Θ direction and/or are not confined to the equatorial plane.

The transformation laws, for the covariant components of a four-momentum, between the BLF and the LNRF $\{p_\mu = [p_r, p_\Theta, p_\Phi, p_t(= -\varepsilon)]$; with $p^\mu = \eta^{\mu\nu} p_\nu; \eta^{\mu\nu} \equiv$ Minkowski metric components$\}$ read

$$P_r = e^{\mu_1} p_r , \tag{2.7a}$$
$$P_\Theta = e^{\mu_2} p_\Theta , \tag{2.7b}$$
$$L = e^{\psi} p_\Phi , \tag{2.7c}$$
$$E = e^{\nu} \varepsilon + \omega e^{\psi} p_\Phi , \tag{2.7d}$$
$$p_r = e^{-\mu_1} P_r , \tag{2.8a}$$
$$p_\Theta = e^{-\mu_2} P_\Theta , \tag{2.8b}$$
$$p_\Phi = e^{-\psi} L , \tag{2.8c}$$
$$\varepsilon = e^{-\nu}(E - \omega L) , \tag{2.8d}$$

[4], where the coefficients are found from the standard metric valid for any stationary, axisymmetric, asymptotically flat spacetime geometry (vacuum or nonvacuum):

$$ds^2 = -e^{2\nu}dt^2 + e^{2\psi}(d\Phi - \omega dt)^2 + e^{2\mu_1}dr^2 + e^{2\mu_2}d\Theta^2 \ . \tag{2.9}$$

The standard metric becomes Kerr if the coefficients are expressed by

$$e^{2\nu} = \frac{\Sigma\Delta}{A} \ , \tag{2.10a}$$

$$e^{2\psi} = \sin^2\Theta\frac{A}{\Sigma} \ , \tag{2.10b}$$

$$e^{2\mu_1} = \frac{\Sigma}{\Delta} \ , \tag{2.11a}$$

$$e^{2\mu_2} = \Sigma \ , \tag{2.11b}$$

$$\omega = \frac{2Mar}{A} \ , \tag{2.12}$$

where

$$A \equiv (r^2 + a^2)^2 - a^2\Delta\sin^2\Theta \ , \tag{2.13}$$

and ω gives the frame dragging velocity.

B. The escape conditions

After the scattering events, not all of the particles escape to infinity. There are certain conditions that a particle must satisfy in order for it to be on an outgoing orbit, which leads to its escape. We now take a look at these conditions.

It is known that outside the horizon, the orbit of a photon (or an unbound material particle with $E/\mu_0 > 1$), may have one or no radial turning points for which $P_r = 0$ [4]. If E/L for that particle lies in the range

$$\frac{E}{L} \leq \Lambda \ , \tag{2.14}$$

for a prograde or direct orbit, there will be one turning point; otherwise, there will be none. As explained in the next paragraph, Λ is defined as the E/L of the isoenergy orbit at constant radii. For photons, as we shall see later, Λ is directly related to the impact parameter, which describes the trajectory of the particle as seen by an observer at a large distance from the KBH. Particles scattered by a local source near the KBH must have a turning point to escape to infinity if they are scattered inward with $P_r' < 0$ (the primes indicate final conditions); however, if the particles have $P_r' > 0$, a turning point means they will be trapped.

The following explains how Λ must be defined in order to determine whether or not a particle escapes to infinity. Let $E_{\rm orb}$ and $L_{\rm orb}$ (the conserved orbital energy and angular momentum as measured by an observer at infinity) be defined such that

$$\Lambda = \frac{E_{\rm orb}}{L_{\rm orb}} \tag{2.15}$$

for a circular orbit at constant radius, $r = r_{\rm orb}$, where $E_{\rm orb}$ and $L_{\rm orb}$ are obtained from the equations governing the orbital trajectory of a particle about a KBH. These conserved parameters are given by

$$\frac{E_{\rm orb}}{\mu_0} = \frac{r^{3/2} - 2Mr^{1/2} + aM^{1/2}}{r^{3/4}(r^{3/2} - 3Mr^{1/2} + 2aM^{1/2})^{1/2}} \tag{2.16}$$

and

$$\frac{L_{\rm orb}}{\mu_0} = \frac{M^{1/2}(r^2 - 2aM^{1/2}r^{1/2} + a^2)}{r^{3/4}(r^{3/2} - 3Mr^{1/2} + 2aM^{1/2})^{1/2}} \tag{2.17}$$

[21] for circular orbits confined to the equatorial plane [$Q = 0$; see Eq. (2.6)], and they are given by Eqs. (A20) and (A21) of Appendix A for nonequatorial ($Q > 0$) "spherical-like" orbits [23]. The relevant algebra to determine the conserved energy and angular momentum of Eqs. (2.16) and (2.17) for these nonequatorial spherical-like orbits can be found in Appendix A. One of these spherical-like orbits consists of a particle repeatedly passing through the equatorial plane while tracing out a helical belt lying on a sphere at constant radius. The belt width or the maximum and minimum latitudes that the particle achieves increase with increasing Q, where Q is given by Eq. (2.6). When a scattered material particle has its energy E', as measured by an observer at infinity, equal to $E_{\rm orb}$ (the isoenergy orbit $\equiv$ the circular orbit of equal energy at constant radius), the radius corresponding to $E_{\rm orb}$, namely, $r_{\rm orb}$, represents a possible turning point for that particle [9]. For photons, $r_{\rm orb}$ is equal to $r_{\rm ph}$, the radius of the photon orbit [the circular orbit of infinite energy per unit rest mass-energy; see Eq. (2.23)].

Looking generally at the escape conditions, there are two. The first is this: If the particle is moving outwardly with $P_r' > 0$ at the point of emission and if it is to escape to infinity, its angular momentum L' must be less than $L_{\rm orb}$, or $E_{\rm orb}$ must not exist. This guarantees that the particle has no radial turning point outside the horizon and, thus, can escape to infinity. This set of inequalities,

$$P_r' > 0 \ , \tag{2.18a}$$

$$E'/L' > \Lambda \ \text{ or } E_{\rm orb} \text{ does not exist} \ , \tag{2.18b}$$

is referred to as the "radial momentum condition" for escape [4]. Note that the particle trajectories that do not have turning points, i.e., satisfying Eq. (2.18b), are independent of the radius of emission: ingoing particles are trapped, outgoing particles escape. On the other hand, particle trajectories that do have turning points are dependent on the radius of emission: both ingoing and outgoing particles will escape if $r > r_{\rm orb}$; conversely, both ingoing and outgoing particles will be trapped if $r < r_{\rm orb}$. Now the second condition is this: If at the point of emission ($r > r_{\rm orb}$) the particle is moving with $P_r' \leq 0$ or $P_r' > 0$, and if it has an angular momentum $L' > L_{\rm orb}$ (guaranteeing a turning point outside the horizon), the particle will escape to infinity. This set of inequalities,

$$P_r' \leq 0 \text{ or } P_r' > 0 \ , \tag{2.19a}$$

$$E'/L' < \Lambda \text{ at } r > r_{\rm orb} \ , \tag{2.19b}$$

is called the "angular momentum condition" for escape [see Eq. (2.14)]. If either of the two sets of conditions Eq. (2.18) or (2.19) is satisfied, the particle will escape to infinity if it is (1) a photon escaping along the equatorial plane (photons not confined to escape along the equatorial plane require an additional condition, as we shall see later) or (2) a material particle with $E'/\mu_0 > 1$; if, however, $E'/\mu_0 \leq 1$, the material particle will be trapped by the KBH.

In the following, we investigate specifically the escape conditions for particles, material and massless, not confined to escape along the equatorial plane: the nonequatorial escape conditions. It is found that the nonequatorial escape conditions for material particles depend on the angular momentum parameter a, the scattered particle energy E', its azimuthal angular momentum L', and its Q value, Q' [related to the polar angular momentum as in Eq. (2.6)]; and these conditions depend on the parameter a and the ratio Q'/E'^2 for scattered massless particles. In these calculations, the nonequatorial escape conditions for massless and material particles are employed.

1. The photon (or any massless particle)

The escape conditions for photons escaping along the equatorial plane, with $Q'_{\rm ph} = 0$, and those for photons escaping not confined to the equatorial plane, with $Q'_{\rm ph} > 0$ are presented here separately for clarity (and for practical purposes) only.

First, $\Lambda = \Lambda_{\rm ph}$ is described for photons escaping along the equatorial plane. In the gravitational potential well of a KBH, $\Lambda_{\rm ph}$ depends only on the angular momentum per unit mass parameter a and is independent of the scattered photon energy $E'_{\rm ph}$. This independence occurs because the path of a photon in a gravitational field is governed by its direction (i.e., its momentum) and not by its energy. For this reason, photons that are bound to the KBH exist only in unstable circular orbits at the radius of the so-called photon orbit, regardless of the differences in their energy values. Now, ordinarily, the Λ's are found from Eqs. (2.15) through (2.17). But in the limit $\mu_0 \to 0$, the quantities

$$E/\mu_0 \ ,$$
$$L/\mu_0 \ ,$$

individually go to infinity; however, their ratio goes to a finite value [2]:

$$\lim_{\mu_0 \to 0} \frac{L/\mu_0}{E/\mu_0} = b_{\rm ph} = \frac{1}{\Lambda_{\rm ph}} \ , \tag{2.20}$$

where $b_{\rm ph}$ is the impact parameter of the photon orbit. In general, this impact parameter is given by

$$b = \left(\frac{\text{angular momentum}}{\text{linear momentum}} \right) = \frac{L}{(E^2 - \mu_0^2)^{1/2}} \ , \tag{2.21}$$

where $c = 1$. (Note that, unless for clarity, the velocity of light is set $c = 1$ throughout this paper.) In the above equation, b is the impact parameter for hyperbolic orbits. It is the distance at which a particle would pass the origin if it were moving in ordinary Minkowski space with no gravitational field. The radius of the photon orbit $r_{\rm ph}$ is given by the root of the denominator of Eq. (2.16) or (2.17):

$$r^{3/2} - 3Mr^{1/2} + 2aM^{1/2} \geq 0 \tag{2.22}$$

[21]. It follows that

$$r_{\rm ph} = 2M\{1 + \cos[(2/3)\arccos(-a/M)]\} \ , \tag{2.23}$$

where, again, $r_{\rm ph}$ represents an unstable circular orbit. This orbit is the innermost boundary of circular orbits for particles. We sometimes refer to $r_{\rm ph}$ as the orbit that has infinite energy and angular momentum per unit rest mass [see Eqs. (2.16) and (2.17) with $\mu_0 = 0$]. For a KBH with $a = 0.998M$, $r_{\rm ph} \simeq 1.074M$. When $r_{\rm ph}$ is substituted into the ratio of Eq. (2.16) to (2.17), an analytical expression for $\Lambda_{\rm ph}$ of the photon orbit confined to the equatorial plane can be found:

$$\Lambda_{\rm ph} = 2(Mr_{\rm ph})^{-1/2}\left(3 + \frac{r_{\rm ph}}{M}\right)^{-1} = \frac{1}{b_{\rm ph}} \tag{2.24}$$

[9]. This value of $\Lambda_{\rm ph}$ is then substituted into the escape conditions of Eqs. (2.18) and (2.19) to determine which of the scattered photons escape moving in the equatorial plane.

Now we will determine the value of $\Lambda = \Lambda^*_{\rm ph} = 1/b^*_{\rm ph}$, corresponding to when the photon orbit is not confined to the equatorial plane. The asterisks indicate nonequatorial confinement. In this case, the radius of the photon orbit [Eq. (2.23)] is substituted into the ratio of Eqs. (A20) and (A21), and thus, the value of $\Lambda^*_{\rm ph}$ is determined in a manner analogous to that used for $\Lambda_{\rm ph}$ of the equatorial photon orbit [Eq. (2.24)]. Note, the radius of the photon orbit for nonequatorial confinement [Eq. (2.23)] is the same as for equatorial confinement [23]. This value of $\Lambda^*_{\rm ph}$ is then used in the escape conditions of Eqs. (2.18) and (2.19) for the scattered photons. However, there now arises another independent condition for the nonexistence of a turning point outside the event horizon that must also be satisfied by the photon, in addition to Eq. (2.18). This additional escape condition is sufficient to account for those photons escaping above and below the equatorial plane.

This second condition depends on the Q value of the scattered photon, $Q'_{\rm ph}$, which is directly proportional to the square of the polar coordinate angular momentum component $(P'_{\rm ph})_\Theta$ for a particle moving through the equatorial plane of the KBH [see Eq. (2.6)]. Define

$$\eta'_{\rm ph} \equiv \frac{Q'_{\rm ph}}{E'^2_{\rm ph}} = \frac{(P'_{\rm ph})^2_\Theta}{E'^2_{\rm ph}} \tag{2.25}$$

[using Eq. (2.6)], again with $Q'_{\rm ph}$ and $E'_{\rm ph}$ being the parameters of the scattered photon; then, the additional

condition is that

$$0 < \eta'_{\rm ph} < \eta^*_{\rm ph} \tag{2.26a}$$

[24], where

$$\eta^*_{\rm ph} \equiv \frac{Q'_{\rm ph}}{E^{*2}_{\rm ph}} = \frac{(P^*_{\rm ph})^2_\Theta}{E^{*2}_{\rm ph}} \ . \tag{2.26b}$$

The inequalities in Eq. (2.26a) indicate that the scattered photon must have $Q'_{\rm ph} > 0$, and that $Q^*_{\rm ph}$ must also be greater than zero (requiring the existence of nonequatorial photon orbits about the KBH), in order to apply this escape condition; the right-hand-side inequality implies that a scattered photon with $\eta'_{\rm ph}$ greater than $\eta^*_{\rm ph}$ has a turning point in the $\hat{\mathbf{e}}_\Theta$ direction, at which $(P'_{\rm ph})_\Theta = 0$. From Eqs. (2.6) and (2.26b), we see that, $Q^*_{\rm ph} = (P^*_{\rm ph})^2_\Theta$ is the Q value for a photon orbiting at the radius of the photon orbit $r_{\rm ph}$, passing through the equatorial plane, in which its path traces out a helix that repeatedly crosses the equatorial plane, as mentioned earlier [23]. The energy $E^*_{\rm ph}$ of Eq. (2.26b) is the conserved total energy of the bound photon in a nonequatorial unstable orbit at $r_{\rm ph}$, as measured by an observer at infinity.

Displayed in Fig. 1(a) is $(P^*_{\rm ph})_\Theta \equiv \sqrt{Q^*_{\rm ph}}$ versus the conserved energy of the nonequatorially orbiting photon, $E^*_{\rm ph}$, at the photon orbit. Note that this energy E^* [see Eq. (A20)] for nonequatorial confined circular orbits at constant radii is the counterpart of Eq. (2.16), which is for the equatorial confined circular orbits. It can be shown from the algebraic equations of Appendix A that, in general, E^* has the form

$$E^* = [f_1(a,r,M)\mu_0^2 + f_2(a,r,M)Q^*]^{1/2} \ , \tag{2.27}$$

with of course $\mu_0 = 0$ for photons, where in principle the functions f_1 and f_2 can be found from the algebraic relations of (A14) to (A24). Note that when Q^* of Eq. (2.27) is set equal to zero, $E^* = E$ of Eq. (2.16); see Fig. 1. An equation similar to Eq. (2.27) exists for L^*, the conserved angular momentum, which reduces to L of Eq. (2.17) when $Q^* = 0$.

Now, to find $\eta^*_{\rm ph}$ of (2.26a), the radius of the photon orbit $r_{\rm ph}$ is substituted into the general expressions for the conserved orbital energy and angular momentum, (A20) and (A21); from these, the ratio of Eq. (2.26b) can be evaluated. Like $\Lambda_{\rm ph} = \Lambda_{\rm ph}(a)$ in the equatorial plane for null geodesic orbits, it is found that $\Lambda^*_{\rm ph} = \Lambda^*_{\rm ph}(a)$ and $\eta^*_{\rm ph} = \eta^*_{\rm ph}(a,M)$ for nonequatorial null geodesic orbits. Moreover, for a given mass M, $\eta^*_{\rm ph}$ behaves in the following manner: (1) $\eta^*_{\rm ph}$ is constant for all photons orbiting at $r_{\rm ph}$, independent of the nonequatorial orbiting photon energy as well as its Q value $Q^*_{\rm ph}$, for KBH's of mass $M \gtrsim 10^7 M_\odot$; (2) $\eta^*_{\rm ph}$ varies slowly with $E^*_{\rm ph}$ and $Q^*_{\rm ph}$ for mass $M \lesssim 10^6 M_\odot$. Note that when $\eta^*_{\rm ph}$ is not constant, the Q value of the scattered particle determines which $\eta^*_{\rm ph}$ to use.

The additional condition of Eq. (2.26a) should be included with Eqs. (2.18) and (2.19) for null geodesics when $Q'_{\rm ph} > 0$. Also, like $\Lambda_{\rm ph}$ of the equatorial plane, $\Lambda^*_{\rm ph}$ and $\eta^*_{\rm ph}$ are associated with the critical impact parameters which separate capture from scattering orbits [24]. These impact parameters describe the trajectory of the photon as seen by an observer at a large distance from the KBH. The parameter $\Lambda_{\rm ph}$ or $\Lambda^*_{\rm ph}$ relates to a possible turning point due to the conserved azimuthal component of the angular momentum $L'_{\rm ph}$, i.e., where $(P'_{\rm ph})_r \to 0$; $\eta^*_{\rm ph}$ relates to a possible turning point due to the polar component of the angular momentum $(P'_{\rm ph})_\Theta$, i.e., where $(P'_{\rm ph})_\Theta \to 0$. A photon scattered with $(P'_{\rm ph})_r > 0$ and $(P'_{\rm ph})_\Theta \neq 0$ must satisfy both the conditions of Eqs. (2.18) and (2.26a), for the nonexistence of a turning point outside the horizon, in order for it to escape to infinity. On the other hand, in addition to the escape conditions of Eq. (2.19), a photon with $(P'_{\rm ph})_r \leq 0$ and

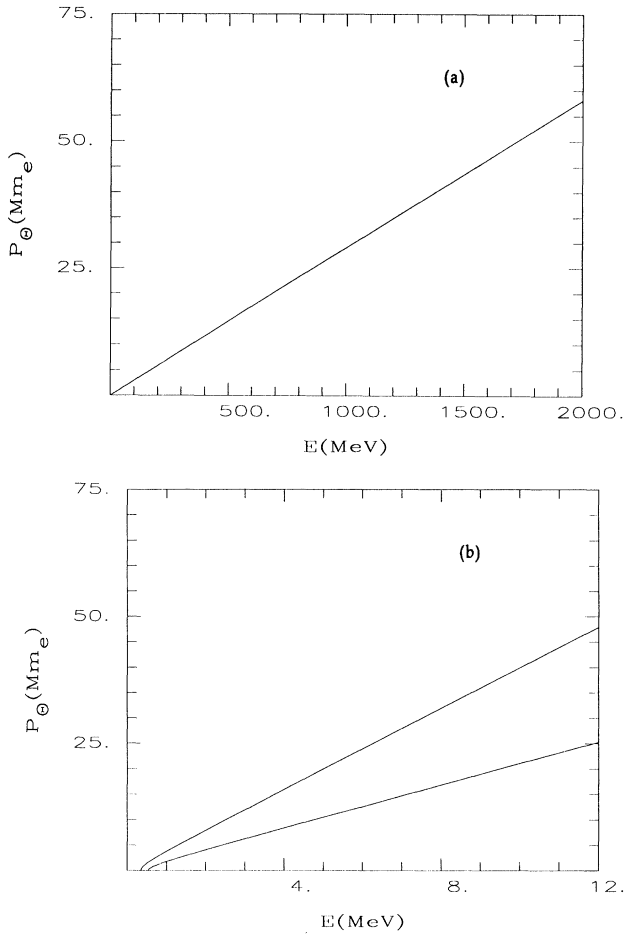

FIG. 1. Orbital parameters of massless and material particles. Magnitude of polar coordinate angular momentum as the bound orbit crosses the equatorial plane ($\equiv \sqrt{Q^*}$) vs the conserved nonequatorial orbital energy: (a) $(P^*_{\rm ph})_\Theta$ vs $E^*_{\rm ph}$ at the photon orbit, $r_{\rm ph} \simeq 1.074M$. (b) $(P^*_e)_\Theta$ vs E^*_e of an orbiting electron at $r_{\rm MB} \simeq 1.089M$ (lower curve), and at $r_{\rm MS} \simeq 1.2M$ (upper curve). Notice that as these momenta go to zero, each of the orbital energies goes to its equatorial confinement value—i.e., as $\sqrt{Q^*_{\rm ph}} \to 0$, $E^*_{\rm ph} \to 0$; as $\sqrt{Q^*_e} \to 0$, $E^*_e \to 0.539$ MeV at $r_{\rm MB}$, and $E^*_e \to 0.349$ MeV at $r_{\rm MS}$.

$(P'_{\rm ph})_\Theta \neq 0$ at $r > r_{\rm orb}$ will escape also if Eq. (2.26a) is not satisfied—implying the existence of a turning point. Moreover, the expressions found for the above parameters (evaluated by methods as described above) are the following: $b_{\rm ph} = 1/\Lambda_{\rm ph} = 1/\Lambda^*_{\rm ph} = 2.1109M$; $\eta^*_{\rm ph} \simeq 0.6518$ s^2 for $M = 10^7 M_\odot$ and $\eta^*_{\rm ph} = 53.402$ s^2 for $M = 10^8 M_\odot$, where $b_{\rm ph}(= b^*_{\rm ph})$ is the impact parameter of Eqs. (2.20), (2.21), and (2.24). Although $\Lambda_{\rm ph}$ and $\Lambda^*_{\rm ph}$ turned out to be equal, they were, however, evaluated independently, from the ratios Eq. (2.16) to (2.17) and (A20) to (A21), respectively.

In summary, the escape conditions depend only on $\Lambda_{\rm ph} = \Lambda^*_{\rm ph}$ for equatorially confined photons ($Q'_{\rm ph} = 0$), and on both $\Lambda^*_{\rm ph}$ and $\eta^*_{\rm ph}$ for nonequatorially confined photons ($Q'_{\rm ph} > 0$). So in general, the values found for $\Lambda^*_{\rm ph}$ and $\eta^*_{\rm ph}$ (by methods described above) are used in Eqs. (2.18), (2.19), and (2.26a), for application of the escape conditions to the scattered photons.

2. The electron (or any material particle)

The escape conditions for the electrons (negatrons and positrons) are determined from Eqs. (A20) and (A21); these equations reduce to Eqs. (2.16) and (2.17), respectively, when the Q value of the orbiting electron, Q^*_e, is set equal to zero. This reduction for the conserved energy E^*_e of an orbiting electron (see Appendix A) to its equatorial value can be seen in Fig. 1(b). Figure 1(b) displays $(P^*_e)_\Theta \equiv \sqrt{Q^*_e}$ versus the energy E^*_e for nonequatorially orbiting electrons at the radii of $r_{\rm MB} \simeq 1.089M$ (marginally bound orbit) and $r_{\rm MS} \simeq 1.2M$ (marginally stable orbit).

The value of $\Lambda = \Lambda^*_e$ of Eq. (2.15) for an orbiting electron, in the case of material particles, does depend on the scattered particle energy, with Λ^*_e being determined in the following manner. When the energy E'_e of the scattered electron and Q'_e are substituted into Eq. (A20), the radius r^*_e of the isoenergy orbit can be solved for numerically. Once this radius r^*_e is known, substitution into Eq. (A21) gives L^*_e. At this point, the ratio of Eq. (2.15) can be evaluated, obtaining Λ^*_e for a particular scattered electron.

This determined value of Λ^*_e for a specific scattered electron is then used in the escape conditions of Eqs. (2.18) and (2.19), along with the condition for unbound orbits ($E'_e > \mu_e$), to determine whether or not the electron escapes to infinity.

C. The efficiency of the Penrose mechanism

Three types of efficiencies are established: Williams's efficiencies (W efficiencies), Piran-Shaham (PS) efficiency [4], and absolute efficiency. We next define and derive expressions of these efficiencies for general Penrose scattering processes.

First, let the subscripts 1, 2, and 3 indicate the infalling particle, the orbiting target particle, and the scattered escaping particle, respectively, and define the following fractions. In the BLF,

$$F_{\rm in} \equiv \frac{E^T_1}{E^T_2 + E^T_1} \ , \tag{2.28a}$$

$$F_{\rm out} \equiv \frac{E^T_3}{E^T_2 + E^T_1} \equiv \epsilon^{\rm abs} \ , \tag{2.28b}$$

where $F_{\rm in}$ and $F_{\rm out}$ are the fractional parts of the total input energy made up by the incoming particles and the outgoing escaping particles, respectively, as measured by a BLF observer; the absolute efficiency $\epsilon^{\rm abs}$ is defined as shown in Eq. (2.28b). The superscript T indicates the total energy of a distribution of particles. Each of the individual energy terms in Eq. (2.28) is the combined energies of those particular particles indicated by subscripts. Similarly, in the laboratory frame (LF),

$$f_{\rm in} \equiv \frac{\varepsilon^T_1}{\varepsilon^T_2 + \varepsilon^T_1} \ , \tag{2.29a}$$

$$f_{\rm out} \equiv \frac{\varepsilon^T_3}{\varepsilon^T_2 + \varepsilon^T_1} \ , \tag{2.29b}$$

where $f_{\rm in}$ and $f_{\rm out}$ are the fractional parts of the total input energy made up by the incoming particles and the outgoing particles, respectively, as measured by a LNRF observer (indicated by the energy notation ε).

Now, using the above fractions, the W efficiencies are defined as

$$\epsilon^W_{\rm LF} \equiv \frac{f_{\rm out}}{f_{\rm in}} = \frac{\varepsilon^T_3}{\varepsilon^T_1} \ , \tag{2.30a}$$

$$\epsilon^W_{\rm BLF} \equiv \frac{F_{\rm out}}{F_{\rm in}} = \frac{E^T_3}{E^T_1} \ , \tag{2.30b}$$

$$\epsilon^W \equiv \frac{\epsilon^W_{\rm BLF}}{\epsilon^W_{\rm LF}} \ , \tag{2.30c}$$

and the PS efficiency is defined by

$$\epsilon^{\rm PS} \equiv \frac{E_3 - (E_1 + E_2)}{E_1 + E_2} \ , \tag{2.31}$$

as measured in the BLF. The efficiencies $\epsilon^W_{\rm LF}$ and $\epsilon^W_{\rm BLF}$ express the total energy of the final escaping particle distribution relative to the initial infalling particle distribution, as measured by a LF observer and a BLF observer, respectively; i.e., $\epsilon^W_{\rm LF}$ and $\epsilon^W_{\rm BLF}$ give us the factor by which the total initial energy of the infalling particle distribution is increased or decreased, by the Penrose scattering process, in the respective frame. The efficiency ϵ^W indirectly measures the blueshift effect due to the frame dragging on the ratios of (2.30a) and (2.30b), by relating the ratio in the LF to its corresponding value in the BLF. On the other hand, $\epsilon^{\rm PS}$ tells whether or not rotational energy was extracted from the KBH by the classical Penrose process (as discussed in Sec. I). For example, for $\epsilon^{\rm PS} > 0$, rotational energy was extracted in the scattering event by the classical Penrose process, and for $\epsilon^{\rm PS} < 0$, there was no energy extracted by this classical process; however, for $\epsilon^{\rm PS} < 0$, and with E_3 (the energy of the escaping particle) greater than E_1 (the initial energy

of infalling particle), and if E_3 is greater than the value it would had acquired had the scattering occurred outside the ergosphere or in flat spacetime, then rotational energy was indirectly extracted from the KBH, although the PS efficiency does not reflect this. This latter process of extracting KBH rotational energy, I have classified as a *quasi*-Penrose process (Sec. IV). Note that $\epsilon^{\rm PS}$ must be evaluated separately for each scattering event (it cannot be used as I have defined the absolute and W efficiencies above for a distribution of scattering events). Details of the efficiencies in (2.30) and (2.31), as they are applied in these scattering processes, will be discussed in Sec. IV.

III. MODEL CALCULATIONS IN THE ERGOSPHERE

A. Inverse Compton scattering

1. Initial conditions in the BLF

The initial conditions for the photons are the following: a photon of energy $E_{\rm ph}$ as measured by an observer at infinity (i.e., in the BLF) is assumed to be emitted inside the ergosphere, from the inner region of the disk (or it may come from outside as in the case of the low energy UV photons), and follows a null geodesic trajectory before colliding with an orbiting electron at a specific radius. Here, only incoming photons moving in the equatorial plane are considered. The motions of the incoming photons discussed in these scattering processes are those moving radially inward. For simplicity, the conditions that the infalling photon encounters in its free fall through the ergosphere before arriving at the designated scattering radius are ignored in these calculations. Otherwise, conditions such as the particle density in the ergosphere and radiative transfer effects would have to be incorporated into the calculations along the null geodesic of the photon. It is assumed that these conditions cause little qualitative change in the results. The photon arrives at the radius in which the scattering takes place with an initial covariant four-momentum $(P_{\rm ph})\mu = [(P_{\rm ph})_r, (P_{\rm ph})_\Theta, L_{\rm ph}, -E_{\rm ph}]$, as measured by an observer at infinity. For a photon falling radially inward along the equatorial plane, $(P_{\rm ph})_\Theta = L_{\rm ph} = 0$. The initial energy of the photon, $E_{\rm ph}$, used in these calculations is either monochromatic or chosen from a blackbody distribution of temperature $T_{\rm ph}$. To select a photon from a blackbody distribution, a Monte Carlo sampling method is employed [25].

The spatial distribution of the electrons is specified as circular orbiting rings, equatorial or nonequatorial. The equatorial orbiting rings can have superposed thermal random velocities on each individual electron, governed by the electron temperature T_e. These rings represent, say, regions of high density in the ergosphere, analogous to those found to form in the inner region of a time-dependent accretion disk around a nonrotating black hole [11].

Two radii are considered for the model electron rings: $r_{\rm MS}(\simeq 1.2M)$, the radius of the marginally stable circular orbit (where $E/\mu_0 < 1$) and $r_{\rm MB}(\simeq 1.089M)$, the radius of the marginally bound circular orbit (where $E/\mu_0 \simeq 1$), for a canonical KBH ($a/M = 0.998$). Recall that an unbound circular orbit is one with $E/\mu_0 > 1$: given an infinitesimal outward perturbation, a particle in such an orbit will escape to infinity on an asymptotically hyperbolic trajectory [21]. The unbound circular orbits are circular in geometry but hyperbolic in energetics, and they are all unstable. Similarly, the orbits at $r_{\rm MB}$ are circular in geometry, but parabolic in energetics. Note that the outer ergosphere boundary, the photon orbit, and the event horizon of a canonical KBH are located at $r_0 = 2M$, $r_{\rm ph} \simeq 1.074M$, and $r_+ \simeq 1.063M$, respectively, in the equatorial plane. The region between the radii $r_{\rm MS}$ and $r_{\rm MB}$ represents the innermost possible periastrons (radial turning points) for bound unstable orbiting particles ($E/\mu_0 \lesssim 1$). A particle in this region, if given a sufficiently large inward perturbation, will eventually fall through the event horizon. Moreover, $r_{\rm MB}$ is the minimum periastron of all circular orbits. Any parabolic trajectory which penetrates to $r < r_{\rm MB}$ must plunge directly into the black hole [21].

The electrons that constitute the equatorial circular orbiting rings about the KBH are assumed in some cases to be cold ($T_e = 0$ K), and in others hot ($T_e \neq 0$ K). In the case of hot electrons, a random motion is superposed on the orbital velocity of the target electron, chosen by applying the Monte Carlo sampling method, simulating a Maxwellian velocity distribution for the electrons at a finite kinetic temperature T_e [25]. The initial conserved orbital energy and angular momentum of an electron belonging to a particular ring (with $T_e = 0$ K) are given by

$$\frac{E_e}{\mu_e} = \text{right-hand side of Eq. (2.16)} \tag{3.1}$$

and

$$\frac{L_e}{\mu_e} = \text{right-hand side of Eq. (2.17)} , \tag{3.2}$$

respectively, as measured by an observer at infinity [see Appendix A for the general expressions of the above-conserved quantities which include orbits that are nonequatorially confined, attributed to $Q \neq 0$ of Eq. (2.6)].

2. Conditions in the LNRF (PCS)

a. Special parameters of the four-momenta. We first define the general geometry used in the Kerr metric [25]. A space vector $\mathbf{p}$ in the LNRF relative to the BLF, at an instant of time in the equatorial plane of the KBH ($\Theta = \pi/2$), is given by

$$\mathbf{p} = p\sin\theta_1\cos\phi_1\hat{\mathbf{e}}_r + p\sin\theta_1\sin\phi_1\hat{\mathbf{e}}_\Theta + p\cos\theta_1\hat{\mathbf{e}}_\Phi , \tag{3.3}$$

where $\hat{\mathbf{e}}_r$, $\hat{\mathbf{e}}_\Theta$, and $\hat{\mathbf{e}}_\Phi$ are the space components of a unit four-vector tangent to the coordinate lines at the

event (r,Θ,Φ,t). This unit four-vector is an orthonormal tetrad, i.e., $\hat{\mathbf{e}}_t \cdot \hat{\mathbf{e}}_t = -1$, $\hat{\mathbf{e}}_r \cdot \hat{\mathbf{e}}_r = 1$, $\hat{\mathbf{e}}_r \cdot \hat{\mathbf{e}}_t = 0$, and so on. In other words, this unit four-vector defines the basis vectors of a local Minkowski metric, where the directions of the space components $\hat{\mathbf{e}}_x$, $\hat{\mathbf{e}}_y$, and $\hat{\mathbf{e}}_z$ of the unit four-vector in the LNRF are in the same directions as $\hat{\mathbf{e}}_r$, $\hat{\mathbf{e}}_\Theta$, and $\hat{\mathbf{e}}_\Phi$ of the BLF, respectively, using a right-hand rule coordinate system. Note that the upper case Greek letters (Θ,Φ) refer to angles centered on the KBH and the lower case letters (θ,ϕ) refer to angles centered on the LNRF.

Next we define the geometry intrinsic to the scattering process. This particular geometry defines a coordinate system in the LNRF with the $\hat{\mathbf{e}}_z$ axis (which defines the direction that the incident photon is traveling) in the same direction as $-\hat{\mathbf{e}}_r$ of the BLF. In this geometry, the directions of the space unit vectors $\hat{\mathbf{e}}_x$, $\hat{\mathbf{e}}_y$, and $\hat{\mathbf{e}}_z$ of the LNRF are in the same directions as $\hat{\mathbf{e}}_\Phi$, $\hat{\mathbf{e}}_\Theta$, and $-\hat{\mathbf{e}}_r$ of the BLF, respectively. The vector $\mathbf{p}$, as defined above, can be expressed in this geometry by

$$\mathbf{p} = -p\cos\theta_2\hat{\mathbf{e}}_r + p\sin\theta_2\sin\phi_2\hat{\mathbf{e}}_\Theta + p\sin\theta_2\cos\phi_2\hat{\mathbf{e}}_\Phi \ . \tag{3.4}$$

Note that the magnitudes of the vector $\mathbf{p}$ given in Eqs. (3.3) and (3.4) are equal. The reason for using these two geometries of the coordinate system in the LNRF relative to the BLF will become apparent later.

In the LNRF, we first define two frames of reference: the LF (the lab frame of a general observer in the LNRF) and the electron rest frame (ERF). The parameters in the ERF are indicated by superscript R and those in the LF have no superscript. The ERF is introduced because in this frame, the determination of the four-momenta of the scattered particles becomes simpler.

From Eq. (3.3), for general initial photon directions in the LF, the initial and final photon space momenta are defined to be

$$\mathbf{p}_{\rm ph} = p_{\rm ph}\sin\theta_{\rm ph}\cos\phi_{\rm ph}\hat{\mathbf{e}}_r + p_{\rm ph}\sin\theta_{\rm ph}\sin\phi_{\rm ph}\hat{\mathbf{e}}_\Theta + p_{\rm ph}\cos\theta_{\rm ph}\hat{\mathbf{e}}_\Phi \tag{3.5}$$

and

$$\mathbf{p}'_{\rm ph} = p'_{\rm ph}\sin\theta'_{\rm ph}\cos\phi'_{\rm ph}\hat{\mathbf{e}}_r + p'_{\rm ph}\sin\theta'_{\rm ph}\sin\phi'_{\rm ph}\hat{\mathbf{e}}_\Theta + p'_{\rm ph}\cos\theta'_{\rm ph}\hat{\mathbf{e}}_\Phi \ , \tag{3.6}$$

where $\theta_{\rm ph}$ and $\theta'_{\rm ph}$ are the polar angles (the polar axis is in the direction of $\hat{\mathbf{e}}_\Phi$) of the incident and scattered photons, respectively; $\phi_{\rm ph}$ and $\phi'_{\rm ph}$ are the corresponding azimuthal angles.

In addition, from Eq. (3.3) we can write, for the target electron,

$$\mathbf{p}_e^T = p_e^T\sin\theta_e\cos\phi_e\hat{\mathbf{e}}_r + p_e^T\sin\theta_e\sin\phi_e\hat{\mathbf{e}}_\Theta + p_e^T\cos\theta_e\hat{\mathbf{e}}_\Phi \ , \tag{3.7}$$

where $\mathbf{p}_e^T$ is the total space momentum vector of a circular orbiting electron, allowing for superposed random motion; the magnitude of $\mathbf{p}_e^T$ will be determined in the following section. As usual, in the LF, the angles of (3.7) are given by

$$\tan\theta_e = \frac{[(p_e^T)_r^2 + (p_e^T)_\Theta^2]^{1/2}}{(p_e^T)_\Phi} \tag{3.8a}$$

[26], and

$$\tan\phi_e = \frac{(p_e^T)_\Theta}{(p_e^T)_r} \ . \tag{3.8b}$$

From Eq. (3.4), we can again define local space momentum vectors of the target electron and the final photon in the LF [as in Eqs. (3.7) and (3.6), respectively]. However, now, these space momenta are defined relative to the direction that the initial photon is traveling—i.e., the polar direction of the coordinate system is in the direction of the momentum vector of the primary photon. Thus, for a radially infalling primary photon, the initial space momentum vector of the electron is expressed in this geometry by

$$\mathbf{p}_e^T = -p_e^T\cos\theta\hat{\mathbf{e}}_r + p_e^T\sin\theta\sin\alpha_1\hat{\mathbf{e}}_\Theta + p_e^T\sin\theta\cos\alpha_1\hat{\mathbf{e}}_\Phi \tag{3.9}$$

[cf. Eq. (3.7)], where θ is the initial polar angle of the electron with the pole in the direction of the initial photon (the $\mathbf{p}_{\rm ph}$ direction) in the LF; α_1 is the initial azimuthal angle of the electron between the $(\hat{\mathbf{e}}_\Phi\mathbf{p}_{\rm ph})$ plane and the $(\mathbf{p}_e^T\mathbf{p}_{\rm ph})$ plane. Similarly, the local vector of the final photon is

$$\mathbf{p}'_{\rm ph} = -p'_{\rm ph}\cos\delta\hat{\mathbf{e}}_r + p'_{\rm ph}\sin\delta\sin\alpha_2\hat{\mathbf{e}}_\Theta + p'_{\rm ph}\sin\delta\cos\alpha_2\hat{\mathbf{e}}_\Phi \tag{3.10}$$

[cf. Eq. (3.6)], where δ is the final polar angle of the photon with the pole in the $\mathbf{p}_{\rm ph}$ direction; α_2 is the final azimuthal angle of the photon between the $(\hat{\mathbf{e}}_\Phi\mathbf{p}_{\rm ph})$ plane and the $(\mathbf{p}'_{\rm ph}\mathbf{p}_{\rm ph})$ plane.

The specific angles defined in the Compton process are δ, the scattering polar angle between the initial photon vector $\mathbf{p}_{\rm ph}$ and the final photon vector $\mathbf{p}'_{\rm ph}$, and α, the scattering azimuthal angle between the $(\mathbf{p}_e^T\mathbf{p}_{\rm ph})$ plane and the $(\mathbf{p}'_{\rm ph}\mathbf{p}_{\rm ph})$ plane, where

$$\alpha = |\alpha_2 - \alpha_1| \tag{3.11}$$

[see Eqs. (3.9) and (3.10)].

From the transformation equation (2.8d), the photon will arrive at the scattering radius with initial energy

$$\varepsilon_{\rm ph} = e^{-\nu}(E_{\rm ph} - \omega L_{\rm ph}) \ , \tag{3.12}$$

as measured by an observer in the LF, where $L_{\rm ph} = 0$ for radial infall.

First, we consider the orbiting electrons to be cold ($T_e = 0$ K). The electrons in the LF will have flat spacetime energy-momentum four-vectors (*principle of relativity*). However, since the electrons are initially moving in circular orbits, before local thermal motions are included, the only nonzero components are $(p_e)_t$ (the time compo-

nent) and $(p_e)_\Phi$ (the azimuthal component). Thus the initial energy and momentum in the $\hat{\mathbf{e}}_\Phi$ direction for an electron as measured by an observer in the LF are

$$\varepsilon_e = \gamma_\Phi m_e \tag{3.13}$$

and

$$(p_e)_\Phi = \gamma_\Phi m_e (v_e)_\Phi \ , \tag{3.14}$$

respectively, where γ_Φ is the electron Lorentz factor due to circular orbital motion only, and $(v_e)_\Phi$ is the azimuthal velocity of the electron relative to the LF. By substitution of Eqs. (3.13) and (3.14) into the transformations, Eqs. (2.7c) and (2.8d), the expressions for $(v_e)_\Phi$ and γ_Φ can be derived in terms of the conserved energy E_e [Eq. (3.1)], and the angular momentum L_e [Eq. (3.2)], as measured by an observer at infinity [27]. It is found that

$$(v_e)_\Phi = \frac{L_e e^{\nu-\psi}}{E_e - \omega L_e} \ , \tag{3.15a}$$

$$\gamma_\Phi = \frac{(E_e - \omega L_e)e^{-\nu}}{m_e} \equiv \gamma_e \ , \tag{3.15b}$$

where the definition arises because γ_e is the general Lorentz factor and does not have to be in the $\hat{\mathbf{e}}_\Phi$ direction only. Equation (3.15) is in agreement with the results of Ref. [21].

Second, still we consider the target electrons to be cold ($T_e = 0$ K); however, now they are allowed to have nonequatorial orbits. In this case, the angular velocity of the target electron in the $\hat{\mathbf{e}}_\Theta$ direction must be included in the calculations. This velocity is given by the following. From Eqs. (2.6) and (2.7b) as the electron passes through the equatorial plane, it is found that

$$(v_e)_\Theta = \frac{e^{-\mu_2}}{\gamma_e m_e}\sqrt{Q_e} \ . \tag{3.16}$$

The Lorentz factor γ_e, for the nonequatorial orbiting electrons, may be obtained from Eqs. (3.15a) and (3.16), or Eq. (3.15b), when E_e and L_e are used from Appendix A [Eqs. (A20) and (A21)]. We next consider what happens when the target electrons have a finite temperature.

b. The comoving frame. The scatterings between the electrons and the photons are evaluated in the ERF. The ERF and the LF are inertial frames related by a Lorentz transformation for frame motion in the direction that the electron moves in the LF. Whenever the electron local kinetic temperature T_e is not zero, the comoving frame (co-LNRF) must be included in the scattering process [25]. The co-LNRF is the proper frame of the matter, say of a group of neighboring electrons; and any inertial observer comoving with the matter is at rest with respect to this frame, i.e., in this frame, $d\tau = dt$, where τ is the proper time and, of course, t is the time measured by an arbitrary inertial observer. Quantities measured in the co-LNRF are denoted with superscript "co." For example, the random velocity of a particle in this frame is indicated by $\mathbf{v}^{\rm co}_{\rm ran}$.

If an electron has a random motion relative to the orbital velocity $\mathbf{v}_e = [0, 0, (v_e)_\Phi]$ in the LF, the ERF will move with velocity $\mathbf{v}^{\rm co}_{\rm ran}$ relative to the co-LNRF. If, however, the electron has no random motion as measured by a co-LNRF observer (with $\mathbf{v}^{\rm co}_{\rm ran} = 0$), then, the ERF will move with the same velocity as the co-LNRF (i.e., the orbital velocity $\mathbf{v}_e$). It follows that, for an electron moving with orbital velocity $(v_e)_\Phi$ and a superposed random velocity $\mathbf{v}_{\rm ran}$ as measured by a LF observer, its total velocity $\mathbf{u}_e$ in the LF is

$$\mathbf{u}_e = (v_e)_\Phi \hat{\mathbf{e}}_\Phi + \mathbf{v}_{\rm ran} \ ; \tag{3.17}$$

these must be added relativistically. The random velocities $\mathbf{v}_{\rm ran}$ of the electrons, due to thermal motions, will be given by a Maxwellian velocity distribution.

Now, the electron temperature T_e of the Maxwellian distribution, as measured by a LF observer, is a thermodynamic quantity that must be initially defined in the co-LNRF. In the proper frame comoving with the matter, the thermodynamic state is governed by the laws of thermodynamics in their usual form [28]. The co-LNRF is related to the LF by a Lorentz transformation. It follows that, the electron temperature in the co-LNRF, $T^{\rm co}_e$, transforms to the electron temperature in the LF, T_e, according to

$$T_e = \gamma_\Phi T^{\rm co}_e \tag{3.18}$$

[28,29], where

$$\gamma_\Phi = [1 - (v_e)_\Phi]^{-1/2} \ ; \tag{3.19}$$

this is the same γ_Φ given by Eq. (3.15).

Once the random motion vector $\mathbf{v}_{\rm ran}$ is chosen from a Maxwellian velocity distribution (using a Monte Carlo sampling method), the Lorentz factor of the thermal orbiting electron is then given by

$$\gamma_e = (1 - \mathbf{u}_e^2)^{-1/2} \ , \tag{3.20}$$

where the velocity $\mathbf{u}_e$ is the total initial velocity vector of a thermal orbiting electron [see Eq. (3.17)] relative to the LF.

Now that we have examined ways to obtain the Lorentz factors of the target electrons: equatorial orbits, nonequatorial orbits, and orbits with thermal motions ($T_e \neq 0$ K), [Eqs. (3.15), (3.16), and (3.20)], the general Lorentz transformations (Appendix B) for the initial photon four-momentum components from the LF to ERF are given by

$$\varepsilon^R_{\rm ph} = \gamma_e[\varepsilon_{\rm ph} - \beta_r(p_{\rm ph})_r - \beta_\Theta(p_{\rm ph})_\Theta - \beta_\Phi(p_{\rm ph})_\Phi] \ , \tag{3.21a}$$

$$(p^R_{\rm ph})_r = \frac{\gamma_e^2}{\gamma_e + 1}\beta_r[\beta_\Phi(p_{\rm ph})_\Phi + \beta_\Theta(p_{\rm ph})_\Theta] + \left(1 + \beta_r^2\frac{\gamma_e^2}{\gamma_e + 1}\right)(p_{\rm ph})_r - \gamma_e\beta_r\varepsilon_{\rm ph} \ , \tag{3.21b}$$

$$(p^R_{\rm ph})_\Theta = \frac{\gamma_e^2}{\gamma_e + 1}\beta_\Theta[\beta_\Phi(p_{\rm ph})_\Phi + \beta_r(p_{\rm ph})_r] + \left(1 + \beta_\Theta^2\frac{\gamma_e^2}{\gamma_e + 1}\right)(p_{\rm ph})_\Theta - \gamma_e\beta_\Theta\varepsilon_{\rm ph} \ , \tag{3.21c}$$

$$(p^R_{\rm ph})_\Phi = \frac{\gamma_e^2}{\gamma_e+1}\beta_\Phi[\beta_\Theta(p_{\rm ph})_\Theta + \beta_r(p_{\rm ph})_r] + \left(1+\beta_\Phi^2\frac{\gamma_e^2}{\gamma_e+1}\right)(p_{\rm ph})_\Phi - \gamma_e\beta_\Phi\varepsilon_{\rm ph} \ , \tag{3.21d}$$

where

$$\gamma_e = (1-\beta_e^2)^{-1/2} \ , \tag{3.21e}$$

and

$$\begin{aligned}\beta_e &= (\beta_r, \beta_\Theta, \beta_\Phi) \\ &\equiv [0, 0, (v_e)_\Phi] \text{ for equatorial targets} \ , \\ &\equiv [0, (v_e)_\Theta, (v_e)_\Phi] \text{ for nonequatorial targets} \ , \\ &\equiv [(u_e)_r, (u_e)_\Theta, (u_e)_\Phi] \text{ for thermal targets} \ ;\end{aligned} \tag{3.21f}$$

the four-momentum components for the initial photon in the LF are given by the transformations of Eqs. (2.8a) to (2.8d).

3. *Scattering process in the LNRF (PCS)*

In this section, the four-momentum of the Penrose Compton scattered (PCS) photon in the ERF, $(p^{R'}_{\rm ph})_\mu = (\mathbf{p}^{R'}_{\rm ph}, i\varepsilon^{R'}_{\rm ph}/c)$, will be determined, and subsequently used in the Lorentz transformations of Appendix B to find the corresponding four-momentum as measured by an observer in the LF. (Note that, in the LNRF, I will sometimes not make the distinction between covariant and contravariant four-momentum, but will instead write the time component to be imaginary, as was done in the above four-vector.)

The final energy of the photon after a scattering event is given by conservation of the four-momentum equation, for this particular scattering process:

$$(p_{\rm ph})_\mu + (p_e)_\mu = (p'_{\rm ph})_\mu + (p'_e)_\mu \ , \tag{3.22}$$

where the primes indicate final conditions. The Compton scattering process in this *pseudo* flat spacetime (i.e., the LNRF) is evaluated in the same way as for a Compton scattering process in flat spacetime. Thus, it is found that the final energy of the photon as measured by an observer in the ERF is

$$\varepsilon^{R'}_{\rm ph} = \frac{\varepsilon^R_{\rm ph}}{1+(\varepsilon^R_{\rm ph}/\mu_e)(1-\cos\delta^R)} \ , \tag{3.23}$$

where δ^R is the scattering (polar) angle between the initial and final space momentum vectors of the photon in the ERF. In general, these vectors are given by Eqs. (3.5) and (3.6), of course, however, with the superscript R appearing in these vectors, indicating parameters measured in the ERF.

We need now to find the scattered photon space momentum vector in the ERF:

$$\mathbf{p}^{R'}_{\rm ph} = p^{R'}_{\rm ph}\sin\theta^{R'}_{\rm ph}\cos\phi^{R'}_{\rm ph}\hat{\mathbf{e}}_r + p^{R'}_{\rm ph}\sin\theta^{R'}_{\rm ph}\sin\phi^{R'}_{\rm ph}\hat{\mathbf{e}}_\Theta + p^{R'}_{\rm ph}\cos\theta^{R'}_{\rm ph}\hat{\mathbf{e}}_\Phi \ , \tag{3.24}$$

where

$$p^{R'}_{\rm ph} = \varepsilon^{R'}_{\rm ph} \ ; \tag{3.25}$$

the angles $\theta^{R'}_{\rm ph}$ and $\phi^{R'}_{\rm ph}$ are the final polar and azimuthal angles of the photon as measured by a ERF observer [cf. Eq. (3.6)]. In the magnitude of Eq. (3.25), $\varepsilon^{R'}_{\rm ph}$ is given by Eq. (3.23).

We must determine how the above angles of Eq. (3.24) are related to the scattering polar and azimuthal angles, δ^R of Eq. (3.23) and α^R, respectively, which are the polar and azimuthal angles defined by the *Klein-Nishina* cross section for Compton scattering processes [Eq. (3.41)]. To determine how these angles are related, we take the scalar vector products of the following: from Eqs. (3.5) and (3.6), $\mathbf{p}_{\rm ph}\cdot\mathbf{p}'_{\rm ph}$ gives

$$\cos\delta = \cos\theta_{\rm ph}\cos\theta'_{\rm ph} + \sin\theta_{\rm ph}\sin\theta'_{\rm ph}\cos(\phi_{\rm ph}-\phi'_{\rm ph}) \ , \tag{3.26}$$

similarly, from Eqs. (3.6) and (3.7), $\mathbf{p}'_{\rm ph}\cdot\mathbf{p}^T_e$ gives

$$\cos\theta' = \cos\theta_e\cos\theta'_{\rm ph} + \sin\theta_e\sin\theta'_{\rm ph}\cos(\phi_e-\phi'_{\rm ph}) \ ; \tag{3.27}$$

from Eqs. (3.5) and (3.7), $\mathbf{p}_{\rm ph}\cdot\mathbf{p}^T_e$ gives

$$\cos\theta = \cos\theta_e\cos_{\rm ph} + \sin\theta_e\sin\theta_{\rm ph}\cos(\phi_e-\phi_{\rm ph}) \ ; \tag{3.28}$$

and from Eqs. (3.9) and (3.10), $\mathbf{p}'_{\rm ph}\cdot\mathbf{p}^T_e$ gives

$$\cos\theta' = \cos\theta\cos\delta + \sin\delta\sin\theta\cos\alpha \ , \tag{3.29}$$

where Eq. (3.11) has been used; again δ is the scattering angle between the initial and final photons; θ and θ' are the angles between the target electron and the initial and final photons, respectively. Equations (3.26) through (3.29) are invariant under a Lorentz transformation, i.e., they retain their same forms. The use of the two geometries, giving rise to the vectors of Eq. (3.3) and (3.4), should be apparent by now: it allows us to relate angles of the inertial frame to the scattering angles by way of Lorentz invariant equations that can, in practice, be solved analytically. Moreover, in the ERF, Eqs. (3.26) to (3.29) reduce to

$$\cos\delta^R = \cos\theta^R_{\rm ph}\cos\theta^{R'}_{\rm ph} + \sin\theta^R_{\rm ph}\sin\theta^{R'}_{\rm ph}\cos(\phi^R_{\rm ph}-\phi^{R'}_{\rm ph}) \ , \tag{3.30}$$

$$\cos\theta^{R'} = \cos\theta^{R'}_{\rm ph} \ , \tag{3.31}$$

$$\cos\theta^{R'} = \cos\theta^R\cos\delta^R + \sin\delta^R\sin\theta^R\cos\alpha^R \ , \tag{3.32}$$

$$\cos\theta^R = \cos\theta^R_{\rm ph} \ , \tag{3.33}$$

since the angles $\theta^R_e = \phi^R_e = 0$, as can be seen in the invariant equation (3.8), with $\mathbf{p}^{T^R}_e = 0$.

In the above equations, the unknown angles are

$$\theta_{\rm ph}^{R'},\ \phi_{\rm ph}^{R'},\ \theta^{R},\ \theta^{R'}\ , \tag{3.34}$$

where $\theta_{\rm ph}^{R'}$ and $\phi_{\rm ph}^{R'}$ are defined in Eq. (3.24); θ^R and $\theta^{R'}$ are angles of the initial and final photons, respectively, as defined in Eq. (3.29), now however, in the ERF. We now solve for these four unknown angles in terms of the known angles

$$\delta^R,\ \alpha^R,\ \theta_{\rm ph}^R,\ \text{and}\ \phi_{\rm ph}^R\ . \tag{3.35}$$

The known angles are defined as the initial angles of the incoming photon $(\theta_{\rm ph}^R, \phi_{\rm ph}^R)$ and the scattering angles of the final photon (δ^R, α^R), as given by the cross section [Eq. (3.41)] for a particular scattering event.

Solving Eqs. (3.30) through (3.33) for the unknown angles of Eq. (3.34), we obtain the following. From Eq. (3.33), it is found that

$$\theta^R = \theta_{\rm ph}^R\ , \tag{3.36}$$

and Eq. (3.32) gives

$$\theta^{R'} = \arccos(\cos\theta^R\cos\delta^R + \sin\delta^R\sin\theta^R\cos\alpha^R)\ . \tag{3.37}$$

From (3.31), we see that

$$\theta_{\rm ph}^{R'} = \theta^{R'}\ . \tag{3.38}$$

Then finally, we solve Eq. (3.30) for $\phi_{\rm ph}^{R'}$ yielding that

$$\phi_{\rm ph}^{R'} = \phi_{\rm ph}^R - \arccos\left(\frac{\cos\delta^R - \cos\theta_{\rm ph}^R\cos\theta_{\rm ph}^{R'}}{\sin\theta_{\rm ph}^R\sin\theta_{\rm ph}^{R'}}\right)\ . \tag{3.39}$$

Equations (3.36) through (3.39) give the unknown angles of Eq. (3.34). In particular, Eqs. (3.38) and (3.39) define the desired azimuthal and polar angles of Eq. (3.24).

We now proceed to specify the known angles of (3.35). First, the angles $\theta_{\rm ph}^R$ and $\phi_{\rm ph}^R$ of the initial photon in the ERF are given by Eq. (3.8), with the replacements

$$\theta_e \to \theta_{\rm ph}^R,\ \phi_e \to \phi_{\rm ph}^R,\ (p_e^T)_r \to (p_{\rm ph}^R)_r,\ \text{etc.} \tag{3.40}$$

[cf. Eq. (3.8)], where the space momentum vector components of the initial photon $[(p_{\rm ph}^R)_{r,\Theta,\Phi}]$ in the ERF are given by the Lorentz transformations of Eqs. (3.21b) through (3.21d). Next, the scattering angles δ^R and α^R are obtained by applying the Monte Carlo method to the Klein-Nishina cross section, used for Compton scattering; this is done in the following section.

a. The Klein-Nishina cross section. The scattering angles δ and α (dropping the R superscripts briefly for simplicity of the notations) in the ERF are obtained by applying the Monte Carlo method to the Klein-Nishina cross section for scattering interactions between free electrons and photons. An expression for the probability that a photon will be emitted at particular angles of α and δ follows from the differential form of the Klein-Nishina cross section [30]:

$$\frac{d\sigma(\delta,\alpha)}{d\Omega} = \frac{1}{2}r_e^2\left(\frac{\varepsilon_{\rm ph}^{R'}}{\varepsilon_{\rm ph}^R}\right)^2\left(\frac{\varepsilon_{\rm ph}^{R'}}{\varepsilon_{\rm ph}^R} + \frac{\varepsilon_{\rm ph}^R}{\varepsilon_{\rm ph}^{R'}} - \sin^2\delta\right)\ , \tag{3.41}$$

where $d\Omega = \sin\delta d\delta d\alpha$; $r_e = 2.818\times10^{-13}$ cm is the classical electron radius; $\varepsilon_{\rm ph}^R$ and $\varepsilon_{\rm ph}^{R'}$ are given by Eqs. (3.21a) and (3.23), respectively. Substitution of Eq. (3.23) into the above differential cross section and integration over angles δ and α yield that

$$\begin{aligned}\sigma(\delta,\alpha) &\equiv \int_0^\delta\int_0^\alpha \frac{d\sigma}{d\Omega}\sin\delta d\delta d\alpha \\ &= \frac{1}{2}r_e^2\alpha\left[\frac{1}{2}\gamma_1\left\{1 - \frac{1}{[1+\gamma_1(1-\cos\delta)^2]}\right\} + \frac{1}{\gamma_1}\left\{\ln[1+\gamma_1(1-\cos\delta)] + \frac{1}{1+\gamma_1(1-\cos\delta)} - 1\right\}\right. \\ &\quad \left. + \frac{1}{\gamma_1^3}\left\{\gamma_1(1-\cos\delta) - 2(1+\gamma_1)\ln[1+\gamma_1(1-\cos\delta)] - \frac{(1+\gamma_1)^2}{1+\gamma_1(1-\cos\delta)} + (1+\gamma_1)^2\right\}\right]\ ,\end{aligned} \tag{3.42}$$

where

$$\gamma_1 = \frac{\varepsilon_{\rm ph}^R}{\mu_e}\ .$$

The above $\sigma(\delta,\alpha)$ is the integral form of the cross section, or the effective area, of an electron producing a scattering event in which a photon is emitted at particular angles of δ and α. When $\delta = \pi$ and $\alpha = 2\pi$ are substituted into Eq. (3.42), we obtain the total cross section of the target electron for scattering of a photon in any direction of δ (between 0 and π) and α (between 0 and 2π):

$$\sigma_{\rm tot} = \sigma_T\frac{3}{4}\left\{\frac{1}{2\gamma_1}\ln(1+2\gamma_1) + \frac{1+\gamma_1}{\gamma_1^3}\left[\frac{2\gamma_1(1+\gamma_1)}{1+2\gamma_1} - \ln(1+2\gamma_1)\right] - \frac{1+3\gamma_1}{(1+2\gamma_1)^2}\right\}\ , \tag{3.43}$$

where $\sigma_T = 8\pi r_e^2/3$ is the cross section for Thompson scattering. The probability that a photon will be emitted at

particular angles of δ and α is

$$\frac{\sigma(\delta,\alpha)}{\sigma_{\rm tot}}=\frac{\sigma(\delta,\alpha)}{\sigma(\pi,2\pi)}=\frac{\sigma(\delta)_1}{\sigma(\delta=\pi)_1}\frac{\sigma(\alpha)_2}{\sigma(\alpha=2\pi)_2}=(\text{prob})_1\,(\text{prob})_2\ ,$$

where the last equality arises because the occurrences of the angles δ and α are independent. That is, Eq. (3.42) is separable, in the sense of

$$\sigma(\delta,\alpha)=\sigma(\delta)_1\sigma(\alpha)_2\ ,$$

with

$$\sigma(\delta)_1\equiv\frac{\sigma(\delta,\alpha)}{\alpha}\ ,$$
$$\sigma(\alpha)_2\equiv\alpha\ .$$

It follows that the probabilities that a photon will be emitted at angles δ and α are

$$(\text{prob})_1=\frac{\sigma(\delta)_1}{\sigma(\delta=\pi)_1}=\frac{\sigma(\delta,\alpha)/\alpha}{\sigma_{\rm tot}/2\pi}=G_1 \tag{3.44}$$

and

$$(\text{prob})_2=\frac{\sigma(\alpha)_2}{\sigma(\alpha=2\pi)_2}=\frac{\alpha}{2\pi}=G_2\ , \tag{3.45}$$

respectively, where the G's are random numbers. The values of δ and α are found from random choices of G_1 and G_2.

After values of δ and α are obtained, the final components of the photon four-momentum can be evaluated from Eqs. (3.23), (3.24), and (3.36) through (3.39). The final four-momentum of the photon in the ERF is transformed to the LF by the inverse of the Lorentz transforms given in Eq. (3.21a) through (3.21d), see Appendix B:

$$\varepsilon'_{\rm ph}=\gamma_e[\varepsilon^{R'}_{\rm ph}+\beta_r(p^{R'}_{\rm ph})_r+\beta_\Theta(p^{R'}_{\rm ph})_\Theta+\beta_\Phi(p^{R'}_{\rm ph})_\Phi]\ , \tag{3.46a}$$

$$(p'_{\rm ph})_r=\frac{\gamma_e^2}{\gamma_e+1}\beta_r[\beta_\Phi(p^{R'}_{\rm ph})_\Phi+\beta_\Theta(p^{R'}_{\rm ph})_\Theta]+\left(1+\beta_r^2\frac{\gamma_e^2}{\gamma_e+1}\right)(p^{R'}_{\rm ph})_r+\gamma_e\beta_r\varepsilon^{R'}_{\rm ph}\ , \tag{3.46b}$$

$$(p'_{\rm ph})_\Theta=\frac{\gamma_e^2}{\gamma_e+1}\beta_\Theta[\beta_\Phi(p^{R'}_{\rm ph})_\Phi+\beta_r(p^{R'}_{\rm ph})_r]+\left(1+\beta_\Theta^2\frac{\gamma_e^2}{\gamma_e+1}\right)(p^{R'}_{\rm ph})_\Theta+\gamma_e\beta_\Theta\varepsilon^{R'}_{\rm ph}\ , \tag{3.46c}$$

$$(p'_{\rm ph})_\Phi=\frac{\gamma_e^2}{\gamma_e+1}\beta_\Phi[\beta_\Theta(p^{R'}_{\rm ph})_\Theta+\beta_r(p^{R'}_{\rm ph})_r]+\left(1+\beta_\Phi^2\frac{\gamma_e^2}{\gamma_e+1}\right)(p^{R'}_{\rm ph})_\Phi+\gamma_e\beta_\Phi\varepsilon^{R'}_{\rm ph}\ , \tag{3.46d}$$

again β_e is given by Eq. (3.21f).

4. Final conditions in the BLF (PCS)

Recalling that the final conditions an observer at infinity measures are the same as those measured by a BLF observer, the transformations of Eq. (2.7) allow us to obtain final measurements in the BLF, in terms of the final conditions of the photon in the LF as given by Eq. (3.46). For the scattered photon, the following energy and space momentum components are measured by a BLF observer:

$$E'_{\rm ph}=e^\nu\varepsilon'_{\rm ph}+\omega e^\psi(p'_{\rm ph})_\Phi\ , \tag{3.47a}$$
$$(P'_{\rm ph})_r=e^{\mu_1}(p'_{\rm ph})_r\ , \tag{3.47b}$$
$$(P'_{\rm ph})_\Theta=e^{\mu_2}(p'_{\rm ph})_\Theta\ , \tag{3.47c}$$
$$(P'_{\rm ph})_\Phi=L'_{\rm ph}=e^\psi(p'_{\rm ph})_\Phi\ . \tag{3.47d}$$

After these local scattering events, some of the photons will escape to infinity, while others will not. Whether or not a particular photon escapes to infinity is governed by the escape conditions given earlier in Sec. II B 1. It follows that the four-momentum components of Eq. (3.47) are used in the escape conditions Eqs. (2.18), (2.19), and (2.26) to determine whether or not a photon escapes to infinity after a scattering event.

B. γ-ray–proton pair production

1. Initial conditions in the BLF

The initial conditions of the γ rays are similar to those for the initial photons of the Compton scattering process. However, the photons are now assumed to have high enough energy-momentum parameters that they can be classified as γ rays, with energies $\sim$ 50 MeV. The incident γ-ray covariant four-momentum is $(P_\gamma)_\mu=[(P_\gamma)_r,0,0,-E_\gamma]$, as measured by an observer at infinity for radial infall. The energy distribution of the infalling γ rays is assumed to be monochromatic in the scatterings.

The spatial distribution of the protons are rings with the same orbital characteristics as the electrons in the Compton scattering process, and the protons are assumed to be cold ($T_p=0$ K). The conserved energy and angular momentum of the orbiting protons, as measured by a BLF observer, are given by equations of the form of (2.16) and (2.17) for equatorial confinement orbits, and by Eqs. (A20) and (A21) for nonequatorial orbits. The scattering between the γ ray and proton takes place at $r_{\rm MB}$ (radius of marginally bound orbit).

2. Conditions in the LNRF ($\gamma p\rightarrow e^-e^+p$)

a. Special parameters of the four-momenta. In the LNRF, we define, the LF and the proton rest frame

(PRF). The scattering process is done in the PRF, since the kinematics are simplest in this frame, as in the ERF for Compton scattering.

Using the geometry that led to the vector of Eq. (3.3), the space momentum vectors are expressed by the following. The general initial LF vector for the proton is

$$\mathbf{p}_p = p_p \sin\theta_p \cos\phi_p \hat{\mathbf{e}}_r + p_p \sin\theta_p \sin\phi_p \hat{\mathbf{e}}_\Theta + p_p \cos\theta_p \hat{\mathbf{e}}_\Phi \ , \tag{3.48}$$

where θ_p and ϕ_p are the initial polar (the pole is in the $\hat{\mathbf{e}}_\Phi$ direction) and azimuthal angles, respectively, of the orbiting proton. Similarly, the general LF γ-ray vector is

$$\mathbf{p}_\gamma = p_\gamma \sin\theta_\gamma \cos\phi_\gamma \hat{\mathbf{e}}_r + p_\gamma \sin\theta_\gamma \sin\phi_\gamma \hat{\mathbf{e}}_\Theta + p_\gamma \cos\theta_\gamma \hat{\mathbf{e}}_\Phi \ , \tag{3.49}$$

where θ_γ and ϕ_γ are the polar and azimuthal angles, respectively, of the incident γ ray. The general LF vector of the scattered positron is

$$\mathbf{p}_+ = p_+ \sin\theta_{e^+} \cos\phi_{e^+} \hat{\mathbf{e}}_r + p_+ \sin\theta_{e^+} \sin\phi_{e^+} \hat{\mathbf{e}}_\Theta + p_+ \cos\theta_{e^+} \hat{\mathbf{e}}_\Phi \ , \tag{3.50}$$

where θ_{e^+} and ϕ_{e^+} are the polar and azimuthal angles, respectively. Similarly, the general LF vector of the scattered negatron is

$$\mathbf{p}_- = p_- \sin\theta_{e^-} \cos\phi_{e^-} \hat{\mathbf{e}}_r + p_- \sin\theta_{e^-} \sin\phi_{e^-} \hat{\mathbf{e}}_\Theta + p_- \cos\theta_{e^-} \hat{\mathbf{e}}_\Phi \ , \tag{3.51}$$

where θ_{e^-} and ϕ_{e^-} are the polar and azimuthal angles, respectively.

Using the geometry that led to the space momentum vector of Eq. (3.4) [i.e., the geometry with the pole of the coordinate system in the direction of the incident γ ray $(-\hat{\mathbf{e}}_r)$], the space momentum vectors for the positron, the negatron, and the primary proton can be defined. Thus, for the positron

$$\mathbf{p}_+ = -p_+ \cos\theta_+ \hat{\mathbf{e}}_r + p_+ \sin\theta_+ \sin\phi_1 \hat{\mathbf{e}}_\Theta + p_+ \sin\theta_+ \cos\phi_1 \hat{\mathbf{e}}_\Phi \ , \tag{3.52}$$

for the negatron,

$$\mathbf{p}_- = -p_- \cos\theta_- \hat{\mathbf{e}}_r + p_- \sin\theta_- \sin\phi_2 \hat{\mathbf{e}}_\Theta + p_- \sin\theta_- \cos\phi_2 \hat{\mathbf{e}}_\Phi \ , \tag{3.53}$$

and similarly, for the primary proton,

$$\mathbf{p}_p = -p_p \cos\theta_{\gamma p} \hat{\mathbf{e}}_r + p_p \sin\theta_{\gamma p} \sin\phi_{\gamma p} \hat{\mathbf{e}}_\Theta + p_p \sin\theta_{\gamma p} \cos\phi_{\gamma p} \hat{\mathbf{e}}_\Phi \ . \tag{3.54}$$

The polar and azimuthal angles of Eqs. (3.52) through (3.54) are defined below.

Specific angles defined in the $\gamma p \rightarrow e^-e^+p$ process are

$$\begin{aligned} \theta_+, \phi_1 &\equiv \text{scattering polar, azimuthal angles between } \mathbf{p}_+ \text{ and } \mathbf{p}_\gamma \ , \\ \theta_-, \phi_2 &\equiv \text{scattering polar, azimuthal angles between } \mathbf{p}_- \text{ and } \mathbf{p}_\gamma \ , \\ \theta_{\gamma p}, \phi_{\gamma p} &\equiv \text{polar, azimuthal angles between } \mathbf{p}_p \text{ and } \mathbf{p}_\gamma \ , \end{aligned} \tag{3.55a}$$

as in the momentum vectors of Eqs. (3.52) through (3.54), and additional specific angles are

$$\begin{aligned} \theta_{p_+} &\equiv \text{spherical polar angle between } \mathbf{p}_p \text{ and } \mathbf{p}_+ \ , \\ \theta_{p_-} &\equiv \text{spherical polar angle between } \mathbf{p}_p \text{ and } \mathbf{p}_- \ , \\ \theta_* &\equiv \text{spherical polar angle between } \mathbf{p}_+ \text{ and } \mathbf{p}_- \ . \end{aligned} \tag{3.55b}$$

We must determine how the above angles relate to the angles of Eqs. (3.50) and (3.51) in order to arrive at the four-momenta of the e^-e^+ pairs (this is done in the following section).

The γ ray arrives at the scattering radius with initial energy

$$\varepsilon_\gamma = e^{-\nu}(E_\gamma - \omega L_\gamma) \tag{3.56}$$

[from Eq. (2.8d); cf. Eq. (3.12)], as measured by an observer in the LF. The circular orbital velocity $(v_p)_\Phi$ and Lorentz factor $\gamma_p (\equiv \gamma_\phi)$ of the cold protons ($T_p = 0$ K) relative to the LF are the same as for the cold electrons [see Eq. (3.15)], at a particular radius.

The orbital velocity of the proton relative to the LF, $\mathbf{v}_p$, and the corresponding Lorentz factor γ_p are used in the Lorentz transformations to find momentum parameters in the PRF. The Lorentz transformations for the four-momentum components of the incident γ ray, from the LF to the PRF, are given by Eqs. (3.21a) through (3.21f), upon changing the subscripts as follows (defined in Appendix B):

$$\begin{aligned} &\varepsilon_{\rm ph} \rightarrow \varepsilon_\gamma, \ (p_{\rm ph})_r \rightarrow (p_\gamma)_r, \ \text{etc.} \ , \\ &\varepsilon^R_{\rm ph} \rightarrow \varepsilon^R_\gamma, \ (p^R_{\rm ph})_r \rightarrow (p^R_\gamma)_r, \ \text{etc.} \ , \\ &\gamma_e \rightarrow \gamma_p \ , \end{aligned} \tag{3.57a}$$

with

$$\beta_p \equiv (\beta_r, \beta_\Theta, \beta_\Phi) = [0, 0, (v_p)_\Phi] \ , \tag{3.57b}$$

where the γ-ray momentum components $(p_\gamma)_\mu$, in the LF, are given by the transformations of Eqs. (2.8a) to (2.8c).

3. *Scattering process in the LNRF ($\gamma p \rightarrow e^-e^+p$)*

As discussed earlier, an observer in the LNRF will see an e^-e^+ pair produced in the Coulomb field of a proton. In this section, the four-momenta of the e^-e^+ pairs are obtained. The energies of the pairs, ε^R_- and ε^R_+, in the PRF (as indicated by the superscript R) will be obtained explicitly from the application of the Monte Carlo method to the differential cross section for this PPP ($\gamma p \rightarrow e^-e^+p$) process, and then, approximate values

of the scattering polar angles θ_+^R and θ_-^R [see Eq. (3.55a)] can be found. Next, these energies and scattering angles are used to determine the relative spherical angle between a pair, θ_*^R, from which the scattering azimuthal angles ϕ_1^R and ϕ_2^R of the pairs are obtained. These scattering angles and energies, along with the spacetime geometry in which the scattering takes place, enable the acquisition of the four-momenta of the pairs.

a. The differential cross section. The angular distributions and energies of the scattered e^-e^+ pairs will be governed by the differential cross section (defined in PRF). This cross section gives the probability of the emission of a positron of energy ε_+ and a negatron of energy ε_-, in the directions θ_+ and θ_-, respectively, relative to the direction of the primary γ ray, into the element $d\varepsilon_+ d\theta_+ d\theta_- d\phi_+$, with ϕ_+ being the relative azimuthal angle of the e^+e^- pair (the superscript R has been dropped briefly for simplicity of the notations):

$$d\sigma = -\frac{Z^2}{137}\frac{e^4}{2\pi}\frac{p_-p_+}{\varepsilon_\gamma^3}\frac{d\varepsilon_+}{q^4}\sin\theta_+\sin\theta_-d\theta_+d\theta_-d\phi_+$$
$$\times\left\{\frac{p_+^2\sin^2\theta_+}{(\varepsilon_+ - p_+\cos\theta_+)^2}(4\varepsilon_-^2 - q^2) + \frac{p_-^2\sin^2\theta_-}{(\varepsilon_- - p_-\cos\theta_-)^2}(4\varepsilon_+^2 - q^2)\right.$$
$$+\frac{2p_+p_-\sin\theta_+\sin\theta_-\cos\phi_+}{(\varepsilon_- - p_-\cos\theta_-)(\varepsilon_+ - p_+\cos\theta_+)}(4\varepsilon_+\varepsilon_- + q^2 - 2\varepsilon_\gamma^2)$$
$$\left.-2\varepsilon_\gamma^2\left[\frac{p_+^2\sin^2\theta_+ + p_-^2\sin^2\theta_-}{(\varepsilon_- - p_-\cos\theta_-)(\varepsilon_+ - p_+\cos\theta_+)}\right]\right\} \tag{3.58}$$

[31]. The expression q in Eq. (3.58) is the magnitude of the recoil momentum or the momentum transferred to the proton, defined by

$$\mathbf{q}^2 = (\mathbf{p}_\gamma - \mathbf{p}_+ - \mathbf{p}_-)^2 \ . \tag{3.59}$$

Equation (3.58) is symmetrical in ε_+ and ε_-. An asymmetry would arise only in higher Born approximations and is small for higher energies. In the extreme relativistic regime where all the energies are large compared to μ_e, Eq. (3.58) can be integrated over all angles [31] to obtain the cross section for the creation of a positron and a negatron with energies ε_+ and ε_-, respectively:

$$d\sigma(\varepsilon_+) = \frac{4Z^2}{137}\frac{r_e^2}{\varepsilon_\gamma^3}\left(\varepsilon_-^2 + \varepsilon_+^2 + \frac{2}{3}\varepsilon_-\varepsilon_+\right)$$
$$\times\left(\ln\frac{2\varepsilon_-\varepsilon_+}{\mu_e\varepsilon_\gamma} - \frac{1}{2}\right)d\varepsilon_+ \ , \tag{3.60}$$

for no screening, in which

$$\frac{2\varepsilon_+\varepsilon_-}{\varepsilon_\gamma} \ll \frac{\mu_e^2}{(1/137)Z^{1/3}} \ .$$

The Monte Carlo method will be applied to the cross section of Eq. (3.60) to calculate energy spectra of the pairs in the PRF. The energy of ε_+ will vary from μ_e to $(\varepsilon_\gamma - \mu_e)$. We integrate Eq. (3.60) between the limits $[\mu_e, \varepsilon_+]$ to obtain the integral form of the cross section:

$$\sigma(\varepsilon_+) \equiv \int_{\mu_e}^{\varepsilon_+} d\sigma(\varepsilon_+) \ . \tag{3.61}$$

But first, set $Z = 1$, assuming a pure hydrogen disk, and assume that the recoil energy given to the proton is small, therefore negligible, so that the conservation of energy gives

$$\varepsilon_\gamma = \varepsilon_+ + \varepsilon_- \ , \tag{3.62a}$$

or

$$\varepsilon_- = \varepsilon_\gamma - \varepsilon_+ \ . \tag{3.62b}$$

Substituting Eq. (3.62b) into (3.60) and performing the integration of Eq. (3.61) yield that

$$\sigma(\varepsilon_+) = \frac{4}{137}\frac{r_e^2}{\varepsilon_\gamma^3}\sum_{i=1}^{9} I_i \ , \tag{3.63a}$$

where

$$I_1 \equiv \varepsilon_\gamma^2\left\{\varepsilon_+\left[\ln\left(\frac{2\varepsilon_+}{\mu_e}\right) - 1\right] + \mu_e(1 - \ln 2)\right\} \ , \tag{3.63b}$$

$$I_2 \equiv \frac{4}{9}\left\{\varepsilon_+^3\left[\ln\left(\frac{2\varepsilon_+}{\mu_e}\right) - \frac{1}{3}\right] - \mu_e^3\left(\ln 2 - \frac{1}{3}\right)\right\} \ , \tag{3.63c}$$

$$I_3 \equiv -\frac{2}{3}\varepsilon_\gamma\left\{\varepsilon_+^2\left[\ln\left(\frac{2\varepsilon_+}{\mu_e}\right)-\frac{1}{2}\right]-\mu_e^2\left(\ln 2-\frac{1}{2}\right)\right\}, \tag{3.63d}$$

$$I_4 \equiv \varepsilon_\gamma^2\left\{(\varepsilon_+-\varepsilon_\gamma)\ln\left(1-\frac{\varepsilon_+}{\varepsilon_\gamma}\right)-\varepsilon_+-(\mu_e-\varepsilon_\gamma)\ln\left(1-\frac{\mu_e}{\varepsilon_\gamma}\right)+\mu_e\right\}, \tag{3.63e}$$

$$I_5 \equiv \frac{4}{3}\left\{\frac{1}{3}(\varepsilon_+^3-\varepsilon_\gamma^3)\ln\left(1-\frac{\varepsilon_+}{\varepsilon_\gamma}\right)-\frac{1}{3}\varepsilon_\gamma^3\left[\frac{\varepsilon_+}{\varepsilon_\gamma}+\frac{1}{2}\left(\frac{\varepsilon_+}{\varepsilon_\gamma}\right)^2+\frac{1}{3}\left(\frac{\varepsilon_+}{\varepsilon_\gamma}\right)^3\right]\right.$$
$$\left.\times-\frac{1}{3}(\mu_e^3-\varepsilon_\gamma^3)\ln\left(1-\frac{\mu_e}{\varepsilon_\gamma}\right)+\frac{1}{3}\varepsilon_\gamma^3\left[\frac{\mu_e}{\varepsilon_\gamma}+\frac{1}{2}\left(\frac{\mu_e}{\varepsilon_\gamma}\right)^2+\frac{1}{3}\left(\frac{\mu_e}{\varepsilon_\gamma}\right)^3\right]\right\}, \tag{3.63f}$$

$$I_6 \equiv -\frac{4}{3}\varepsilon_\gamma\left\{\frac{1}{2}(\varepsilon_+^2-\varepsilon_\gamma^2)\ln\left(1-\frac{\varepsilon_+}{\varepsilon_\gamma}\right)-\frac{1}{2}\varepsilon_\gamma^2\left[\frac{\varepsilon_+}{\varepsilon_\gamma}+\frac{1}{2}\left(\frac{\varepsilon_+}{\varepsilon_\gamma}\right)^2\right]\right.$$
$$\left.\times-\frac{1}{2}(\mu_e^2-\varepsilon_\gamma^2)\ln\left(1-\frac{\mu_e}{\varepsilon_\gamma}\right)+\frac{1}{2}\varepsilon_\gamma^2\left[\frac{\mu_e}{\varepsilon_\gamma}+\frac{1}{2}\left(\frac{\mu_e}{\varepsilon_\gamma}\right)^2\right]\right\}, \tag{3.63g}$$

$$I_7 \equiv -\frac{1}{2}\varepsilon_\gamma^2(\varepsilon_+-\mu_e), \tag{3.63h}$$

$$I_8 \equiv -\frac{2}{9}(\varepsilon_+^3-\mu_e^3), \tag{3.63i}$$

$$I_9 \equiv \frac{1}{3}\varepsilon_\gamma(\varepsilon_+^2-\mu_e^2). \tag{3.63j}$$

If we substitute $\varepsilon_+ = \varepsilon_\gamma - \mu_e$ (defining the upper limit of the integration) into Eq. (3.63), we get the total cross section for the creation of an e^-e^+ pair, which depends only on the γ-ray energy:

$$\sigma(\varepsilon_\gamma) = \frac{4}{137}r_e^2\left[\frac{7}{9}\ln\left(\frac{2\varepsilon_\gamma}{\mu_e}\right)-\frac{109}{54}\right] \tag{3.64}$$

[31]. The probability that a positron is emitted with a particular value of energy ε_+^R (resuming to use the superscript R to indicate the PRF) is

$$\frac{\sigma(\varepsilon_+^R)}{\sigma(\varepsilon_\gamma^R)} = G_3, \tag{3.65}$$

where the numerator and denominator are given by Eqs. (3.63) and (3.64), respectively, and G_3 is a random number varying between 0 and 1. The values of ε_+^R, and hence ε_-^R from Eq. (3.62), are found from the random choice, or Monte Carlo selection, of G_3 for each scattering event.

b. Approximate values of the scattering angles. The angular distribution of θ_+^R and θ_-^R is generally obtained by integrating the differential cross section of Eq. (3.58); however, the integration is complex. Yet, through suitable approximations, a usable formula for the mean square angle $\langle\theta_-^{R^2}\rangle$ (or $\langle\theta_+^{R^2}\rangle$) is found in the relativistic regime ($\varepsilon_\gamma^R, \varepsilon_+^R, \varepsilon_-^R \gg \mu_e$). At such high energies, the maximum emission of electrons in the angular distribution, in the forward direction (traveling direction of the γ ray), becomes more pronounced, which makes use of the root-mean-square angle valid. For smaller energies, the concentration in the forward direction is less marked [16]. The mean square angle between the electron and the γ ray is given below (it applies as well to the positron):

$$\langle\theta_-^{R^2}\rangle = \frac{4\mu_e^2}{\varepsilon_-^{R^2}}\left\{\frac{F\ln(\theta_{-\max}^R/\beta)+G\ln[\tilde{\alpha}^2+(1+\tilde{\alpha})\theta_{-\max}^{R^2}/\tilde{\alpha}^2+(1+\tilde{\alpha})\beta^2]}{(1+\tilde{\alpha}^2)f_1(\gamma_2)+\frac{2}{3}\tilde{\alpha}f_2(\gamma_2)}\right\} \tag{3.66a}$$

[32], where screening by atomic electrons has been neglected, with

$$\tilde{\alpha} \equiv \frac{\varepsilon_+^R}{\varepsilon_-^R}, \tag{3.66b}$$

$$F \equiv 2(1+\tilde{\alpha}^2)\ln(2\varepsilon_+^R\varepsilon_-^R/\mu_e\varepsilon_\gamma^R)+\tilde{\alpha}(2-\tilde{\alpha})-1, \tag{3.66c}$$

$$G \equiv [(2+\tilde{\alpha})(4+4\tilde{\alpha}-\tilde{\alpha}^2)/16(1+\tilde{\alpha})], \tag{3.66d}$$

$$\beta \equiv 2\left(\frac{\mu_e\varepsilon_+^R}{\varepsilon_-^R\varepsilon_\gamma^R}\right)^2. \tag{3.66e}$$

Once the energies of the produced pairs are obtained by the Monte Carlo method described in the previous section [Eqs. (3.58) through (3.65)], the root-mean-square angle of Eq. (3.66) $\langle\theta_-^{R^2}\rangle^{1/2}$ (or $\langle\theta_+^{R^2}\rangle^{1/2}$) can be found, since Eq. (3.66) is symmetrical in θ_-^R and θ_+^R. Note that the restrictions on Eq. (3.66) are

$$\varepsilon_\gamma^R, \varepsilon_+^R, \varepsilon_-^R \gg \mu_e,$$
$$\frac{\mu_e}{4\varepsilon_-^R} \ll \frac{\varepsilon_+^R}{\varepsilon_\gamma} \le 1,$$
$$\beta < \theta_{-\max}^R \le 60^\circ. \tag{3.67}$$

The two functions $f_1(\gamma_2)$ and $f_2(\gamma_2)$ in Eq. (3.66a) are

functions of

$$\gamma_2 = \frac{100\mu_e\varepsilon_\gamma^R}{\varepsilon_+^R\varepsilon_-^R Z^{1/3}} \tag{3.68}$$

[31], the quantity which determines the effects of screening. For $\gamma_2 < 1$ screening is important, where as for $\gamma_2 \gg 1$ screening can be practically neglected. The functions f_1 and f_2 are given in several papers [31–33]. After the suitable high energy approximations are made in the cross section of Eq. (3.58) [34], $\theta^R_{-\,\max}$ is defined as the upper limit of the integration, leading to the derivation of the root-mean-square angle given in Eq. (3.66). The choice of $\theta^R_{-\,\max}$ of Eqs. (3.66) and (3.67) is, unfortunately, ambiguous. However, the higher the energy of the γ ray, the smaller the value of $\theta^R_{-\,\max}$ is allowed to be, and thus, the more accurate is the determined scattering angle θ^R_- (the same applies for θ^R_+).

c. Conservation of the four-momentum equation. The four-momentum equation is solved for this PPP process to obtain an expression for the angle θ^R_*, which is the spherical angle between an emitted e^-e^+ pair [see Eq. (3.55b)], as measured by a PRF observer. The four-momenta in the LF for the γ ray, the proton, the positron, and the negatron will be denoted by $p_{\gamma\lambda}$, $p_{p\lambda}$, $p_{+\lambda}$, and $p_{-\lambda}$, respectively, where λ is a summation index. From the conservation of four-momentum

$$p_{\gamma\lambda} + p_{p\lambda} = p_{+\lambda} + p_{-\lambda} + p'_{p\lambda} \ , \tag{3.69}$$

where the prime indicates the scattered proton. Equation (3.69) leads to

$$\sum_\lambda (p_{\gamma\lambda} + p_{p\lambda} - p_{-\lambda} - p_{+\lambda})^2 = \sum_\lambda p'^2_{p\lambda} \ . \tag{3.70}$$

The individual four-momenta in the above equations can be expressed as the following. For the

$$\text{incident photon} : p_{\gamma\lambda} = (\mathbf{p}_\gamma, i\varepsilon_\gamma) \ , \tag{3.71a}$$

$$\text{scattered positron} : p_{+\lambda} = (\mathbf{p}_+, i\varepsilon_+) \ , \tag{3.71b}$$

$$\text{scattered negatron} : p_{-\lambda} = (\mathbf{p}_-, i\varepsilon_-) \ , \tag{3.71c}$$

$$\text{incident and scattered proton} : p_{p\lambda} = (\mathbf{p}_p, i\varepsilon_p) \text{ and } p'_{p\lambda} = (\mathbf{p}'_p, i\varepsilon'_p) \ . \tag{3.71d}$$

Squaring Eq. (3.70), and using the Lorentz invariance of the scalar product of the four-momentum with itself (i.e., $p_\lambda^2 = -m_0^2$), we obtain the Lorentz invariant form of the conservation of four-momentum equation:

$$\sum_\lambda p_{+\lambda}p_{-\lambda} = \sum_\lambda (p_{\gamma\lambda}p_{+\lambda} + p_{\gamma\lambda}p_{-\lambda} + p_{p\lambda}p_{-\lambda} - p_{\gamma\lambda}p_{p\lambda}) + m_e^2 \ . \tag{3.72}$$

We then use Eq. (3.71) to evaluate the individual terms in Eq. (3.72), where, for example,

$$\sum_\lambda p_{+\lambda}p_{-\lambda} = \mathbf{p}_+ \cdot \mathbf{p}_- - \varepsilon_+\varepsilon_- \ , \tag{3.73a}$$

$$\sum_\lambda p_{\gamma\lambda}p_{+\lambda} = \mathbf{p}_\gamma \cdot \mathbf{p}_+ - \varepsilon_\gamma\varepsilon_+ \ , \text{etc.} \ , \tag{3.73b}$$

i.e., with similar relations existing for the other four-momentum products in Eq. (3.72). Substitution of the evaluated four-momentum products of Eq. (3.73) into (3.72), with the space momentum vector of the proton $\mathbf{p}_p^R = 0$ in the PRF, and using the definition of the angles in Eq. (3.55), the conservation of the four-momentum equation expressed in the PRF is given by

$$\begin{aligned} p_+^R p_-^R \cos\theta_*^R - \varepsilon_+^R\varepsilon_-^R = {} & p\gamma^R p_+^R \cos\theta_+^R - \varepsilon_\gamma^R\varepsilon_+^R \\ & + p\gamma^R p_-^R \cos\theta_-^R - \varepsilon_\gamma^R\varepsilon_-^R \\ & - \mu_p\varepsilon_-^R - \mu_p\varepsilon_+^R - \mu_p\varepsilon_\gamma^R + m_e^2 \ , \end{aligned} \tag{3.74}$$

where μ_p is the rest-mass-energy of the proton. In the extreme relativistic regime, where $\varepsilon_+^R, \varepsilon_-^R \gg \mu_e$, the magnitudes of the momenta of the positron and negatron in the PRF are given by

$$p_+^R \simeq \varepsilon_+^R \text{ and } p_-^R \simeq \varepsilon_-^R \ , \tag{3.75}$$

respectively. And as usual, the magnitude of the γ-ray momentum is

$$p_\gamma^R = \varepsilon_\gamma^R \ . \tag{3.76}$$

Substitutions of Eqs. (3.75) and (3.76) into Eq. (3.74) yield the desired angle

$$\begin{aligned} \cos\theta_*^R = {} & 1 + \varepsilon_\gamma^R \left[\frac{1}{\varepsilon_-^R}(\cos\theta_+^R - 1) + \frac{1}{\varepsilon_+^R}(\cos\theta_-^R - 1) \right] \\ & - \frac{1}{\varepsilon_+^R\varepsilon_-^R}[\mu_p(\varepsilon_-^R + \varepsilon_+^R - \varepsilon_\gamma^R) - \mu_e^2] \ , \end{aligned} \tag{3.77a}$$

or, using the assumption of Eq. (3.62),

$$\begin{aligned} \cos\theta_*^R = {} & 1 + \varepsilon_\gamma^R \left[\frac{1}{\varepsilon_-^R}(\cos\theta_+^R - 1) + \frac{1}{\varepsilon_+^R}(\cos\theta_-^R - 1) \right] \\ & + \frac{\mu_e^2}{\varepsilon_+^R\varepsilon_-^R} \ . \end{aligned} \tag{3.77b}$$

d. The four-momenta of the pairs. We now want to find the relationships between the scattering angles of Eq. (3.55) and the angles $(\theta^R_{e^+}, \phi^R_{e^+})$ and $(\theta^R_{e^-}, \phi^R_{e^-})$ in order to calculate the four-momenta of the e^-e^+ pairs, Eqs. (3.50) and (3.51). The scalar vector products give us the following: from Eqs. (3.49) and (3.50), $\mathbf{p}_\gamma \cdot \mathbf{p}_+$ gives

$$\cos\theta_+ = \cos\theta_\gamma\cos\theta_{e^+} + \sin\theta_\gamma\sin\theta_{e^+}\cos(\phi_\gamma - \phi_{e^+}) \ ; \tag{3.78a}$$

from Eqs. (3.49) and (3.51), $\mathbf{p}_\gamma \cdot \mathbf{p}_-$ gives

$$\cos\theta_- = \cos\theta_\gamma\cos\theta_{e^-} + \sin\theta_\gamma\sin\theta_{e^-}\cos(\phi_\gamma - \phi_{e^-}) \ ; \tag{3.78b}$$

from Eqs. (3.48) and (3.50), $\mathbf{p}_p \cdot \mathbf{p}_+$ gives

$$\cos\theta_{p_+} = \cos\theta_p\cos\theta_{e^+} + \sin\theta_p\sin\theta_{e^+}\cos(\phi_p - \phi_{e^+}) \ ; \tag{3.78c}$$

from Eqs. (3.48) and (3.51), $\mathbf{p}_p \cdot \mathbf{p}_-$ gives

$$\cos\theta_{p_-} = \cos\theta_p \cos\theta_{e^-} + \sin\theta_p \sin\theta_{e^-} \cos(\phi_p - \phi_{e^-}) \ ; \tag{3.78d}$$

from Eqs. (3.48) and (3.49), $\mathbf{p}_p \cdot \mathbf{p}_\gamma$ gives

$$\cos\theta_{\gamma p} = \cos\theta_p \cos\theta_\gamma + \sin\theta_p \sin\theta_\gamma \cos(\phi_p - \phi_\gamma) \ ; \tag{3.78e}$$

from Eqs. (3.52) and (3.53), $\mathbf{p}_+ \cdot \mathbf{p}_-$ gives

$$\cos\theta_* = \cos\theta_+ \cos\theta_- + \sin\theta_+ \sin\theta_- \cos(\phi_1 - \phi_2) \ ; \tag{3.78f}$$

from Eqs. (3.52) and (3.54), $\mathbf{p}_p \cdot \mathbf{p}_+$ gives

$$\cos\theta_{p_+} = \cos\theta_{\gamma p} \cos\theta_+ + \sin\theta_{\gamma p} \sin\theta_+ \cos(\phi_{\gamma p} - \phi_1) \ ; \tag{3.78g}$$

from Eqs. (3.53) and (3.54), $\mathbf{p}_p \cdot \mathbf{p}_-$ gives

$$\cos\theta_{p_-} = \cos\theta_{\gamma p} \cos\theta_- + \sin\theta_{\gamma p} \sin\theta_- \cos(\phi_{\gamma p} - \phi_2) \ , \tag{3.78h}$$

[cf. Eq. (3.55)]. The angular relations of Eq. (3.78) are Lorentz invariant. Since in the PRF, equations similar to (3.8) give for the proton, that, $\theta_p^R = \phi_p^R = 0$, and since by way of deduction, $\phi_{\gamma p}^R = 0$, i.e., the azimuthal angle (defined by a plane) between the proton at rest and the γ ray is zero the angular relations of Eq. (3.78) become, in the PRF,

$$\cos\theta_+^R = \cos\theta_\gamma^R \cos\theta_{e^+}^R + \sin\theta_\gamma^R \sin\theta_{e^+}^R \cos(\phi_\gamma^R - \phi_{e^+}^R) \ , \tag{3.79a}$$

$$\cos\theta_-^R = \cos\theta_\gamma^R \cos\theta_{e^-}^R + \sin\theta_\gamma^R \sin\theta_{e^-}^R \cos(\phi_\gamma^R - \phi_{e^-}^R) \ , \tag{3.79b}$$

$$\cos\theta_{p_+}^R = \cos\theta_{e^+} \ , \tag{3.79c}$$

$$\cos\theta_{p_-}^R = \cos\theta_{e^-} \ , \tag{3.79d}$$

$$\cos\theta_{\gamma p}^R = \cos\theta_\gamma^R \ , \tag{3.79e}$$

$$\cos\theta_*^R = \cos\theta_+^R \cos\theta_-^R + \sin\theta_+^R \sin\theta_-^R \cos(\phi_1^R - \phi_2^R) \ , \tag{3.79f}$$

$$\cos\theta_{p_+}^R = \cos\theta_{\gamma p}^R \cos\theta_+^R + \sin\theta_{\gamma p}^R \sin\theta_+^R \cos\phi_1^R \ , \tag{3.79g}$$

$$\cos\theta_{p_-}^R = \cos\theta_{\gamma p}^R \cos\theta_-^R + \sin\theta_{\gamma p}^R \sin\theta_-^R \cos\phi_2^R \ . \tag{3.79h}$$

The equations of (3.79) must be solved simultaneously for the unknown angles:

$$\begin{aligned} &\theta_{e^+}^R, \phi_{e^+}^R, \theta_{e^-}^R, \phi_{e^-}^R \ , \\ &\theta_{\gamma p}^R, \phi_{\gamma p}^R, \theta_{p^+}^R, \phi_{p^-}^R \ , \\ &\phi_1^R, \phi_2^R \ , \end{aligned} \tag{3.80a}$$

in terms of the known angles:

$$\theta_+^R, \theta_-^R, \theta_*^R, \theta_\gamma^R, \phi_\gamma^R \tag{3.80b}$$

[cf. Eqs. (3.49) through (3.51), and Eq. (3.55) for definitions]. However, but first before solving Eq. (3.79) for the unknown angles [Eq. (3.80a)], we complete the determination of the known angles [Eq. (3.80b)]. Recall that once the energies of the pairs, ε_+^R and ε_-^R, are given by Eqs. (3.62b) and (3.65), the angles θ_+^R and θ_-^R are found from Eq. (3.66), since this equation is symmetrical in θ_-^R and θ_+^R. Also recall that θ_*^R is given by Eq. (3.77). The last of the known angles to be determined are the angles θ_γ^R and ϕ_γ^R of the infalling photon [cf. Eq. (3.49)]; they are determined by Eq. (3.8), with the replacements

$$\theta_e \to \theta_\gamma^R, \phi_e \to \phi_\gamma^R, (p_e^T)_r \to (p_\gamma^R)_r, \text{ etc.} \ , \tag{3.81}$$

where $(p_\gamma^R)_\mu$, with $\mu = r, \Theta, \Phi$, are the space momentum components of the γ ray in the PRF, given by the Lorentz transformations of Eq. (3.57).

Now let us proceed to solve the equations of (3.79), with the goal of obtaining the polar and azimuthal angles of the e^-e^+ pairs in the PRF. These angles are found to be (see Appendix C)

$$\theta_{e^+}^R = \arccos(\cos\theta_\gamma^R \cos\theta_+^R + \sin\theta_\gamma^R \sin\theta_+^R \cos\phi_1^R) \ , \tag{3.82a}$$

$$\phi_{e^+}^R = \phi_\gamma^R - \arccos\left(\frac{\cos\theta_+^R - \cos\theta_\gamma^R \cos\theta_{e^+}^R}{\sin\theta_\gamma^R \sin\theta_{e^+}^R}\right) \ , \tag{3.82b}$$

and

$$\theta_{e^-}^R = \arccos(\cos\theta_\gamma^R \cos\theta_-^R + \sin\theta_\gamma^R \sin\theta_-^R \cos\phi_2^R) \ , \tag{3.83a}$$

$$\phi_{e^-}^R = \phi_\gamma^R - \arccos\left(\frac{\cos\theta_-^R - \cos\theta_\gamma^R \cos\theta_{e^-}^R}{\sin\theta_\gamma^R \sin\theta_{e^-}^R}\right) \ , \tag{3.83b}$$

for the positron and negatron, respectively, where

$$\phi_2^R = \phi_1^R - \arccos\left(\frac{\cos\theta_*^R - \cos\theta_+^R \cos\theta_-^R}{\sin\theta_+^R \sin\theta_-^R}\right) \ . \tag{3.84}$$

Except for the scattering angle ϕ_1^R [see Eq. (3.55)], we now know of ways to determine all the angles of Eq. (3.80). In the following paragraph, the determination of the angle ϕ_1^R is presented.

The Monte Carlo method is employed to determine an appropriate value for the angle ϕ_1^R. Recall that the scattering azimuthal angle ϕ_+^R of Eq. (3.58) is the angle between the $(\mathbf{p}_\gamma^R \mathbf{p}_+^R)$ plane and the $(\mathbf{p}_\gamma^R \mathbf{p}_-^R)$ plane. From the scattering geometry used to derive the momenta of Eqs. (3.52) and (3.53), with the pole of the coordinate system in the direction of the γ ray,

$$\phi_+ = |\phi_2 - \phi_1| \tag{3.85}$$

[cf. Eq. (3.55a)]; therefore, by the invariance of the distance between two spatial points in Minkowski spacetime under a Lorentz transformation, it follows that, in the PRF,

$$\phi_+^R = |\phi_2^R - \phi_1^R| \ . \tag{3.86}$$

In principle, we could solve for the angle ϕ_1^R from Eq. (3.86), if the angle ϕ_+^R were known. However, since the cross section of Eq. (3.58) is a function of ϕ_+^R, θ_+^R, and θ_-^R in the sense that the probabilities of these angles cannot be separated as was done in the Klein-Nishina cross section for the Compton scattering processes [see Eqs. (3.41) through (3.45)], we cannot apply the Monte Carlo method to ϕ_+^R directly. For this reason, we must apply the Monte Carlo method directly to ϕ_1^R, to be used in Eq. (3.84); then, if desirable, the relative angle ϕ_+^R can be obtained from Eq. (3.86). Therefore, the probability that the positron will be emitted with azimuthal angle ϕ_1^R existing somewhere between 0 and 2π is given by

$$\frac{\phi_1^R}{2\pi} = G_4 \ , \tag{3.87}$$

where G_4 is a random number ranging between 0 and 1. Choices of G_4 will give values of ϕ_1^R, and thus, ϕ_2^R can be found by Eq. (3.84).

In summary and to conclude this section, the energies of the positron and the negatron in the PRF are given by Eqs. (3.65) and (3.62), respectively. Substitution of the appropriate angles of Eqs. (3.82) and (3.83) into the vectors of Eqs. (3.50) and (3.51) gives the space momenta of the positron, $\mathbf{p}_+^R$, and the negatron, $\mathbf{p}_-^R$, as measured by a PRF observer. We next use the Lorentz transformations (Appendix B) to find the four-momenta of the e^-e^+ pairs as measured by a LF observer:

$$\varepsilon_+ = \gamma_p[\varepsilon_+^R + \beta_r(p_+^R)_r + \beta_\Theta(p_+^R)_\Theta + \beta_\Phi(p_+^R)_\Phi] \ , \tag{3.88a}$$

$$(p_+)_r = \frac{\gamma_p^2}{\gamma_p+1}\beta_r[\beta_\Phi(p_+^R)_\Phi + \beta_\Theta(p_+^R)_\Theta] + \left(1+\beta_r^2\frac{\gamma_p^2}{\gamma_p+1}\right)(p_+^R)_r + \gamma_p\beta_r\varepsilon_+^R \ , \tag{3.88b}$$

$$(p_+)_\Theta = \frac{\gamma_p^2}{\gamma_p+1}\beta_\Theta[\beta_\Phi(p_+^R)_\Phi + \beta_r(p_+^R)_r] + \left(1+\beta_\Theta^2\frac{\gamma_p^2}{\gamma_p+1}\right)(p_+^R)_\Theta + \gamma_p\beta_\Theta\varepsilon_+^R \ , \tag{3.88c}$$

$$(p_+)_\Phi = \frac{\gamma_p^2}{\gamma_p+1}\beta_\Phi[\beta_\Theta(p_+^R)_\Theta + \beta_r(p_+^R)_r] + \left(1+\beta_\Phi^2\frac{\gamma_p^2}{\gamma_p+1}\right)(p_+^R)_\Phi + \gamma_p\beta_\Phi\varepsilon_+^R \ , \tag{3.88d}$$

where β is given by Eq. (3.57b), and γ_p is the corresponding Lorentz factor of the orbiting proton. A Lorentz transformation similar to the above exists for the negatron also.

4. Final conditions in the BLF ($\gamma p \rightarrow e^-e^+p$)

The transformations of Eq. (2.7) give us the final measurements in the BLF, in terms of the final conditions of the e^-e^+ pairs in the LF. From the measurements given in Eq. (3.88), an observer at infinity will obtain for the positron the following energy and space momentum components:

$$E_+ = e^\nu\varepsilon_+ + \omega e^\psi(p_+)_\Phi \ , \tag{3.89a}$$

$$(P_+)_r = e^{\mu_1}(p_+)_r \ , \tag{3.89b}$$

$$(P_+)_\Theta = e^{\mu_2}(p_+)_\Theta \ , \tag{3.89c}$$

$$(P_+)_\Phi = L_+ = e^\psi(p_+)_\Phi \ , \tag{3.89d}$$

where similar equations exist for the negatron.

Whether or not the scattered electrons can escape to infinity is governed by the escape conditions given in Sec. II B 2, for an electron or any material particle. The four-momentum components of Eq. (3.89) are used in the escape conditions of Eqs. (2.18) and (2.19) to determine if the electron escapes from the potential well of the KBH.

C. γ-ray–γ-ray pair production

1. Initial conditions in the BLF

Initially, a photon of energy $E_{\gamma 1}$, assumed to be emitted inside the ergosphere (say from processes intrinsic to an accretion disk or from prior Penrose processes), collides with another photon of energy $E_{\gamma 2}$ orbiting at the photon orbit, $r_{\rm ph} \simeq 1.074M$ [see Eqs. (2.22) and (2.23)]. This collisional process subsequently produces an e^-e^+ pair. The energies $E_{\gamma 1}$ and $E_{\gamma 2}$ are those measured by an observer at infinity. Since the scattering takes place in the equatorial plane of the KBH, an observer at infinity will measure the following initial four-momenta. For the incident radially infalling photon (only the radially emitted incident photons are considered here), the BLF observer measures

$$(P_{\gamma 1})_\mu = [(P_{\gamma 1})_r, 0, 0, -E_{\gamma 1}] \ , \tag{3.90}$$

and for the orbiting photon he measures

$$(P_{\gamma 2})_\mu = [0, (P_{\gamma 2})_\Theta, L_{\gamma 2}, -E_{\gamma 2}] \ , \tag{3.91}$$

for the covariant four-momenta.

The initial energies of the two colliding photons can cover a wide range of values, as long as the threshold conditions of Eq. (1.2) are satisfied. The energies $E_{\gamma 1}$ of the incident photons will have a blackbody distribution, or they will be monochromatic. The energy $E_{\gamma 2}$ of the orbiting photon is given by Eq. (A20) of Appendix A, for a circular nonequatorially confined massless particle orbiting at the photon orbit. This conserved energy $E_{\gamma 2}$ depends on the Q value [cf. Eq. (2.27)] of the photon and increases with increasing $Q_{\gamma 2}(\equiv Q_{\rm ph}^*)$, as can be seen in Fig. 1(a). Note, in general, and for all practical purposes, for the orbiting photon, $Q_{\gamma 2}$ must be > 0, meaning that the orbit cannot be confined to the equatorial plane [cf. Eq. (2.6)].

2. Conditions in the LNRF ($\gamma\gamma \rightarrow e^-e^+$)

a. Special parameters of the four-momenta. Using the geometry defined by Eq. (3.3), i.e., with the pole of the

coordinate system positioned in the $\hat{\mathbf{e}}_\Phi$ direction, the space momentum vectors for this pair production process can be expressed by the following. The general LF vector of the infalling photon is given by

$$\mathbf{p}_{\gamma 1} = p_{\gamma 1}\sin\theta_{\gamma 1}\cos\phi_{\gamma 1}\hat{\mathbf{e}}_r + p_{\gamma 1}\sin\theta_{\gamma 1}\sin\phi_{\gamma 1}\hat{\mathbf{e}}_\Theta + p_{\gamma 1}\cos\theta_{\gamma 1}\hat{\mathbf{e}}_\Phi \ , \tag{3.92}$$

where, $\theta_{\gamma 1}$ and $\phi_{\gamma 1}$ are the polar and azimuthal angles of the infalling photon, respectively. Similarly, the general LF vector of the orbiting photon is expressed by

$$\mathbf{p}_{\gamma 2} = p_{\gamma 2}\sin\theta_{\gamma 2}\cos\phi_{\gamma 2}\hat{\mathbf{e}}_r + p_{\gamma 2}\sin\theta_{\gamma 2}\sin\phi_{\gamma 2}\hat{\mathbf{e}}_\Theta + p_{\gamma 2}\cos\theta_{\gamma 2}\hat{\mathbf{e}}_\Phi \ , \tag{3.93}$$

where, $\theta_{\gamma 2}$ and $\phi_{\gamma 2}$ are the polar and azimuthal angles of the orbiting photon, respectively. The general LF space momentum vectors of the positron and negatron are given by Eqs. (3.50) and (3.51), respectively.

From the geometry leading to Eq. (3.4), now with the pole of the coordinate system positioned in the direction of the incident infalling photon [the $(-\hat{\mathbf{e}}_r)$ direction], space momentum vectors for the positron, the negatron, and the orbiting photon can be defined as follows. For the positron,

$$\mathbf{p}_+ = -p_+\cos\theta_+\hat{\mathbf{e}}_r + p_+\sin\theta_+\sin\phi_+\hat{\mathbf{e}}_\Theta + p_+\sin\theta_+\cos\phi_+\hat{\mathbf{e}}_\Phi \ , \tag{3.94}$$

for the negatron,

$$\mathbf{p}_- = -p_-\cos\theta_-\hat{\mathbf{e}}_r + p_-\sin\theta_-\sin\phi_-\hat{\mathbf{e}}_\Theta + p_-\sin\theta_-\cos\phi_-\hat{\mathbf{e}}_\Phi \ . \tag{3.95}$$

Similarly, for the orbiting photon,

$$\mathbf{p}_{\gamma 2} = -p_{\gamma 2}\cos\theta_{\gamma\gamma}\hat{\mathbf{e}}_r + p_{\gamma 2}\sin\theta_{\gamma\gamma}\sin\phi_{\gamma\gamma}\hat{\mathbf{e}}_\Theta + p_{\gamma 2}\sin\theta_{\gamma\gamma}\cos\phi_{\gamma\gamma}\hat{\mathbf{e}}_\Phi \ . \tag{3.96}$$

The polar and azimuthal angles of Eqs. (3.94) through (3.96) are defined below.

Specific angles defined in the $\gamma\gamma \to e^-e^+$ process are

$$\begin{aligned} \theta_+, \phi_+ &\equiv \text{scattering polar, azimuthal angles between } \mathbf{p}_{\gamma 1} \text{ and } \mathbf{p}_+ \ , \\ \theta_-, \phi_- &\equiv \text{polar, azimuthal angles between } \mathbf{p}_{\gamma 1} \text{ and } \mathbf{p}_- \ , \\ \theta_{\gamma\gamma}, \phi_{\gamma\gamma} &\equiv \text{polar, azimuthal angles between } \mathbf{p}_{\gamma 1} \text{ and } \mathbf{p}_{\gamma 2} \ . \end{aligned} \tag{3.97}$$

The angles of Eq. (3.97) comprise a coordinate system in which $\mathbf{p}_{\gamma 1}$ is the direction of the polar axis and azimuths are measured relative to the azimuths of $\mathbf{p}_{\gamma 2}$. Additional specific scattering angles are

$$\begin{aligned} \theta_{\gamma +} &\equiv \text{spherical polar angle between } \mathbf{p}_{\gamma 2} \text{ and } \mathbf{p}_+ \ , \\ \theta_{\gamma -} &\equiv \text{spherical polar angle between } \mathbf{p}_{\gamma 2} \text{ and } \mathbf{p}_- \ , \\ \theta_* &\equiv \text{spherical polar angle between } \mathbf{p}_+ \text{ and } \mathbf{p}_- \ . \end{aligned} \tag{3.98}$$

From the transformation Eq. (2.8d), the radially infalling (or emitted) photon will arrive at the photon orbit with initial energy given by

$$\varepsilon_{\gamma 1} = e^{-\nu}E_{\gamma 1} \ , \tag{3.99}$$

as measured by a LF observer, where $E_{\gamma 1}$ is the infalling photon energy measured by a BLF observer. Similarly, for the orbiting photon,

$$\varepsilon_{\gamma 2} = e^{-\nu}(E_{\gamma 2} - \omega L_{\gamma 2}) \ , \tag{3.100}$$

as measured by a LF observer, where $E_{\gamma 2}$ and $L_{\gamma 2}$ are the conserved orbital energies and angular momentum, respectively, of the orbiting photon measured by a BLF observer [Eqs. (A20) and (A21) of Appendix A].

3. *Scattering process in the LNRF ($\gamma\gamma \to e^-e^+$)*

As discussed earlier, a radially infalling photon produces an e^-e^+ pair upon colliding with a target photon orbiting along the photon orbit. In this section, the four-momenta of the pairs are obtained. The scattering process is done in the center-of-momentum (c.m.) frame, which is related to the LF by a Lorentz transformation. The sum of the space momentum vectors for a given event is zero in the c.m. frame. In the c.m. frame, the kinematics of the $\gamma\gamma \to e^-e^+$ process become simpler; for this reason, the scattering process is computed in this frame. Note that parameters measured in the c.m. frame will be indicated by the superscript c.

a. The center-of-momentum frame. Energy and momentum properties of the $\gamma\gamma \to e^-e^+$ process in the c.m. frame are the following [30]. In the c.m. frame,

$$\mathbf{P}^c = \mathbf{p}^c_+ + \mathbf{p}^c_- = \mathbf{p}^c_{\gamma 1} + \mathbf{p}^c_{\gamma 2} = 0 \ , \tag{3.101}$$

where $\mathbf{P}^c$ is the composite space momentum in this frame. That is, for a given scattering the total space momentum vanishes in the c.m. frame, where $\mathbf{p}^c_+, \mathbf{p}^c_-, \mathbf{p}^c_{\gamma 1}$, and $\mathbf{p}^c_{\gamma 2}$ are the space momentum vectors of the positron, the negatron, the infalling photon, and the orbiting photon, respectively. Other properties characterizing the c.m. frame are

$$E^c = \varepsilon^c_+ + \varepsilon^c_- = \varepsilon^c_{\gamma 1} + \varepsilon^c_{\gamma 2} \ , \tag{3.102a}$$

$$\varepsilon^c_{\gamma 1} = = \varepsilon^c_{\gamma 2} = \varepsilon^c_+ = \varepsilon^c_- \ , \tag{3.102b}$$

$$\beta^c_+ = \frac{p^c_+}{\varepsilon^c_+} = \beta^c_- = \frac{p^c_-}{\varepsilon^c_-} \ , \tag{3.102c}$$

where E^c is the composite energy in the c.m. frame; $\varepsilon^c_{\gamma 1}$, $\varepsilon^c_{\gamma 2}$, ε^c_+, or ε^c_- equals the c.m. frame energy; and $\beta^c_+ = \beta^c_-$ defines the velocity of the positron or negatron relative to the c.m. frame.

It follows that, from the relativistic energy-momentum

equation for a particle of rest-mass-energy μ_0 in any inertial frame,

$$\varepsilon^2 = p^2 + \mu_0^2 \ , \tag{3.103}$$

we have, for the positron in the c.m. frame,

$$p_+^c = \left(\varepsilon_+^{c^2} - \mu_e^2\right)^{1/2} \ . \tag{3.104}$$

Equation (3.104) allows us to determine the magnitude of the space momentum, $p_+^c = p_-^c$, of the e^+e^- pairs, once the c.m. frame energy, say ε_+^c of Eq. (3.102b), is known.

The angles between the space momentum vectors become, in the c.m. frame,

$$\theta_*^c = \theta_{\gamma\gamma}^c = \pi \ , \tag{3.105a}$$
$$\theta_-^c + \theta_+^c = \pi \ , \tag{3.105b}$$
$$\phi_+^c \pm \pi = \phi_-^c \ , \tag{3.105c}$$
$$\theta_{e^-}^c + \theta_{e^+}^c = \pi \ , \tag{3.105d}$$
$$\phi_{e^+}^c \pm \pi = \phi_{e^-}^c \ , \tag{3.105e}$$

[use Eqs. (3.97), (3.98), (3.50), and (3.51), for identification of these angles, however, in the c.m. frame].

The connections between the c.m. frame and the LF are obtainable by Lorentz transformations. The relative frame velocity or the velocity that the c.m. frame moves with respect to a LF observer is given by

$$\mathbf{v}_{\text{c.m.}} = \frac{\mathbf{p}_{\gamma 1} + \mathbf{p}_{\gamma 2}}{\varepsilon_{\gamma 1} + \varepsilon_{\gamma 2}} \tag{3.106a}$$

[35], or

$$\beta_{\text{c.m.}} = \frac{\mathbf{p}_{\gamma 1} + \mathbf{p}_{\gamma 2}}{\varepsilon_{\gamma 1} + \varepsilon_{\gamma 2}} \tag{3.106b}$$

with

$$\gamma_{\text{c.m.}} = (1 - \beta_{\text{c.m.}}^2)^{-1/2} \ , \tag{3.106c}$$

where $\varepsilon_{\gamma 1}$ and $\mathbf{p}_{\gamma 1}$ are the energy and space momentum vector of the radially infalling photon as measured by a LF observer; similarly, $\varepsilon_{\gamma 2}$ and $\mathbf{p}_{\gamma 2}$ are these measured quantities for the orbiting photon: These four-momentum components of the incident photons in the LF are given by the transformations of Eq. (2.8).

We now determine the c.m. frame energy of Eq. (3.102b), to be used in Eq. (3.104). From the definitions of the composite space momentum and the composite energy of Eqs. (3.101) and (3.102a), respectively, in the c.m. frame, conservation of four-momentum allows us to write the composite four-momenta in the LF and the c.m. frame as

$$P_\lambda^i = P_\lambda^f \ ,$$
$$[(\mathbf{p}_{\gamma 1} + \mathbf{p}_{\gamma 2}), i(\varepsilon_{\gamma 1} + \varepsilon_{\gamma 2})] = [(\mathbf{p}_+ + \mathbf{p}_-), i(\varepsilon_+ + \varepsilon_-)] \ , \tag{3.107}$$

and

$$P_\lambda^{c^i} = P_\lambda^{c^f} \ ,$$
$$[(\mathbf{p}_{\gamma 1}^c + \mathbf{p}_{\gamma 2}^c), i(\varepsilon_{\gamma 1}^c + \varepsilon_{\gamma 2}^c)] = [(\mathbf{p}_+^c + \mathbf{p}_-^c), i(\varepsilon_+^c + \varepsilon_-^c)] \ , \tag{3.108}$$
$$[0, i(\varepsilon_{\gamma 1}^c + \varepsilon_{\gamma 2}^c)] = [0, i(\varepsilon_+^c + \varepsilon_-^c)] \ ,$$

respectively. To find the c.m. frame energy, say ε_+^c [see Eq. (3.102b)], in terms of the LF energies $\varepsilon_{\gamma 1}$ and $\varepsilon_{\gamma 2}$ [see Eqs. (3.99) and (3.100)], use the invariance of the scalar product of a four-vector with itself,

$$\sum_\lambda P_\lambda^2 = \sum_\lambda (P_\lambda^c)^2 \ , \tag{3.109}$$

and solve for ε_+^c. Now, substitution of Eqs. (3.107) and (3.108) into Eq. (3.109) yields

$$[(\mathbf{p}_{\gamma 1} + \mathbf{p}_{\gamma 2}), i(\varepsilon_{\gamma 1} + \varepsilon_{\gamma 2})^2] = [(\mathbf{p}_+^c + \mathbf{p}_-^c), i(\varepsilon_+^c + \varepsilon_-^c)]^2 \ ,$$
$$(\mathbf{p}_{\gamma 1} + \mathbf{p}_{\gamma 2})^2 - (\varepsilon_{\gamma 1} + \varepsilon_{\gamma 2})^2 = 0 - (\varepsilon_+^c + \varepsilon_-^c)^2 \ ;$$

it follows that

$$\mathbf{p}_{\gamma 1} \cdot \mathbf{p}_{\gamma 2} - \varepsilon_{\gamma 1}\varepsilon_{\gamma 2} = -2(\varepsilon_+^c)^2 \ ,$$

where Eqs. (3.102b) and (3.103) have been used. Since the angle between $\mathbf{p}_{\gamma 1}$ and $\mathbf{p}_{\gamma 2}$ is $\theta_{\gamma\gamma}$ [see Eq. (3.97)], we obtain for the c.m. frame energy that

$$\varepsilon_+^c = \sqrt{\frac{1}{2}\varepsilon_{\gamma 1}\varepsilon_{\gamma 2}(1 - \cos\theta_{\gamma\gamma})} \ , \tag{3.110}$$

where according to Eq. (3.102b), $\varepsilon_+^c = \varepsilon_-^c = \varepsilon_{\gamma 1}^c = \varepsilon_{\gamma 2}^c$.

Next we substitute Eq. (3.110) into (3.104) to determine the magnitude of the space momentum vectors of the e^-e^+ pairs ($p_+^c = p_-^c$), where in the c.m. frame these vectors are given by

$$\mathbf{p}_+^c = p_+^c \sin\theta_{e^+}^c \cos\phi_{e^+}^c \hat{\mathbf{e}}_r + p_+^c \sin\theta_{e^+}^c \sin\phi_{e^+}^c \hat{\mathbf{e}}_\Theta + p_+^c \cos\theta_{e^+}^c \hat{\mathbf{e}}_\Phi \ , \tag{3.111a}$$

$$\mathbf{p}_-^c = p_-^c \sin\theta_{e^-}^c \cos\phi_{e^-}^c \hat{\mathbf{e}}_r + p_-^c \sin\theta_{e^-}^c \sin\phi_{e^-}^c \hat{\mathbf{e}}_\Theta + p_-^c \cos\theta_{e^-}^c \hat{\mathbf{e}}_\Phi \ , \tag{3.111b}$$

Application of the Lorentz transformations to Eq. (3.111), once these vectors are known in the c.m. frame, gives the space momentum vectors in the LF. However, we will come to this later, but first, we must determine the angles of Eq. (3.111). These angles $(\theta_{e^+}^c, \phi_{e^+}^c, \theta_{e^-}^c, \phi_{e^-}^c)$ must be defined in terms of the scattering angles $(\theta_+^c, \phi_+^c, \theta_-^c, \phi_-^c)$ in the c.m. frame [cf. Eq. (3.97)]. The scattering angles are determined from the cross section for the $\gamma\gamma \to e^-e^+$ process; and once the scattering angles are known, relations can be found between them and the angles of Eq. (3.111), using the scalar products of the space momentum vectors, as done in the previous scattering processes (Secs. III A 3 and III B 3 d): These derivations are completed in the following subsections.

b. The differential cross section. The scattering angle θ_+^c in the c.m. frame is obtained by applying the Monte Carlo method to the differential cross section for this pair production process:

$$d\sigma(\theta_+^c) = \frac{\pi}{2} r_e^2 \beta_+ \left(\frac{\mu_e}{\varepsilon_+^c}\right)^2 \left[\frac{1-\beta_+^4\cos^4\theta_+^c + 2(\mu_e/\varepsilon_+^3)\beta_+^2\sin^2\theta_+^c}{(1-\beta_+^2\cos^2\theta_+^c)^2}\right] \sin\theta_+^c\, d\theta_+^c \tag{3.112}$$

[30], where $\beta_+ \equiv \beta_+^c$ of Eq. (3.102c). Although the cross section of Eq. (3.112) is written in terms of the positron it can, however, refer to either the positron or the negatron. Also, this pair production cross section by unpolarized photons is symmetrical with respect to $\theta_+^c = \frac{\pi}{2}$. Moreover, at very high energies the e^-e^+ pairs are produced at very small angles with respect to the line of incidence.

The differential cross section Eq. (3.112) is integrated over the angle θ_+^c, to get the integral form of the cross section:

$$\sigma(\theta_+^c) = \int_0^{\theta_+^c} d\sigma(\theta_+^c) \ . \tag{3.113}$$

Upon performing the algebraic integration of Eq. (3.113), it is simple to show that

$$\sigma(\theta_+^c) = \frac{\pi}{2} r_e^2 (1-\beta_+^2)\left\{\frac{1}{2}(3-\beta_+^4)\ln\left[\frac{(1+\beta_+)(1-\chi)}{(1-\beta_+)(1+\chi)}\right] \beta_+(\beta_+^2-2) + \chi\left[1 + \frac{(1-\beta_+^2)^2}{1-\chi^2}\right]\right\} , \tag{3.114a}$$

where

$$\chi \equiv \beta_+ \cos\theta_+^c \tag{3.114b}$$

[36]. The relation that

$$\frac{\mu_e^2}{(\varepsilon_+^c)^2} = (1-\beta_+^2) \tag{3.115}$$

has been used; Eq. (3.115) can be derived from Eqs. (3.102c) and (3.104). The total cross section σ_T is obtained when the integrated cross section Eq. (3.114) is evaluated at $\theta_+^c = \pi$; thus,

$$\sigma_T = \frac{\pi}{2} r_e^2 (1-\beta_+^2)\left[(3-\beta_+^4)\ln\left(\frac{1+\beta_+}{1-\beta_+}\right) - 2\beta_+(2-\beta_+^2)\right] . \tag{3.116}$$

Equation (3.116) is in agreement with the result of Ref. [30]. Finally, the probability that the positron be emitted at a particular angle θ_+^c is

$$(prob)_{\theta_+^c} = \frac{\sigma(\theta_+^c)}{\sigma_T} = G_5 \ , \tag{3.117}$$

where G_5 is a random number between 0 and 1. The random choices of G_5 give values of θ_+^c as desired, and using Eq. (3.105b) gives θ_-^c.

c. The four-momenta of the pairs. Now that we have ways to determine θ_+^c and θ_-^c, we then proceed to find the angles in Eq. (3.111). By taking the scalar vector product of the space momentum vectors, the following is obtained: from Eqs. (3.94) and (3.96), $\mathbf{p}_+ \cdot \mathbf{p}_{\gamma 2}$ gives

$$\cos\theta_{\gamma+} = \cos\theta_{\gamma\gamma}\cos\theta_+ + \sin\theta_{\gamma\gamma}\sin\theta_+\cos(\phi_{\gamma\gamma} - \phi_+) \ ; \tag{3.118a}$$

from Eqs. (3.95) and (3.96), $\mathbf{p}_- \cdot \mathbf{p}_{\gamma 2}$ gives

$$\cos\theta_{\gamma-} = \cos\theta_{\gamma\gamma}\cos\theta_- + \sin\theta_{\gamma\gamma}\sin\theta_-\cos(\phi_{\gamma\gamma} - \phi_-) \ ; \tag{3.118b}$$

from Eqs. (3.94) and (3.95), $\mathbf{p}_+ \cdot \mathbf{p}_-$ gives

$$\cos\theta_* = \cos\theta_+\cos\theta_- + \sin\theta_+\sin\theta_-\cos(\phi_+ - \phi_-) \ ; \tag{3.118c}$$

from Eqs. (3.50) and (3.94), $\mathbf{p}_+ \cdot \mathbf{p}_+$ gives

$$1 = -\sin\theta_{e^+}\cos\phi_{e^+}\cos\theta_+ + \sin\theta_{e^+}\sin\phi_{e^+}\sin\theta_+\sin\phi_+ + \cos\theta_{e^+}\sin\theta_+\cos\phi_+ \ ; \tag{3.118d}$$

from Eqs. (3.51) and (3.95), $\mathbf{p}_- \cdot \mathbf{p}_-$ gives

$$1 = -\sin\theta_{e^-}\cos\phi_{e^+}\cos\theta_- + \sin\theta_{e^-}\sin\phi_{e^-}\sin\theta_-\sin\phi_- + \cos\theta_{e^-}\sin\theta_-\cos\phi_- \ ; \tag{3.118e}$$

from Eqs. (3.96) and (3.50), $\mathbf{p}_{\gamma 2} \cdot \mathbf{p}_+$ gives

$$\cos\theta_{\gamma+} = -\sin\theta_{e^+}\cos\phi_{e^+}\cos\theta_{\gamma\gamma} + \sin\theta_{\gamma\gamma}\sin\phi_{\gamma\gamma}\sin\theta_{e^+}\sin\phi_{e^+} + \cos\theta_{e^+}\sin\theta_{\gamma\gamma}\cos\phi_{\gamma\gamma} \ ; \tag{3.118f}$$

from Eqs. (3.96) and (3.51), $\mathbf{p}_{\gamma 2} \cdot \mathbf{p}_-$ gives

$$\cos\theta_{\gamma-} = -\sin\theta_{e^-}\cos\phi_{e^-}\cos\theta_{\gamma\gamma} + \sin\theta_{\gamma\gamma}\sin\phi_{\gamma\gamma}\sin\theta_{e^-}\sin\phi_{e^-} + \cos\theta_{e^-}\sin\theta_{\gamma\gamma}\cos\phi_{\gamma\gamma} \ . \tag{3.118g}$$

The angular relations of Eq. (3.118) are Lorentz invariant. Therefore, by Eq. (3.105), they become, in the c.m. frame,

$$\cos\theta_{\gamma+}^c = -\cos\theta_+^c \ , \tag{3.119a}$$

$$\cos\theta_{\gamma-}^c = -\cos\theta_-^c \ , \tag{3.119b}$$

$$-1 = \cos\theta_+^c\cos\theta_-^c + \sin\theta_+^c\sin\theta_-^c\cos(\phi_+^c - \phi_-^c) \ , \tag{3.119c}$$

$$1 = -\sin\theta_{e^+}^c\cos\phi_{e^+}^c\cos\theta_+^c + \sin\theta_{e^+}^c\sin\phi_{e^+}^c\sin\theta_+^c\sin\phi_+^c + \cos\theta_{e^+}^c\sin\theta_+^c\cos\phi_+^c \ , \tag{3.119d}$$

$$1 = -\sin\theta_{e^-}^c\cos\phi_{e^-}^c\cos\theta_-^c + \sin\theta_{e^-}^c\sin\phi_{e^-}^c\sin\theta_-^c\sin\phi_-^c + \cos\theta_{e^-}^c\sin\theta_-^c\cos\phi_-^c \ , \tag{3.119e}$$

$$\cos\theta^c_{\gamma+} = \sin\theta^c_{e^+}\cos\theta^c_{e^+} \ , \tag{3.119f}$$

$$\cos\theta^c_{\gamma-} = \sin\theta^c_{e^-}\cos\theta^c_{e^-} \ . \tag{3.119g}$$

The equations of (3.119) must be solved simultaneously for the unknown angles $\theta^c_{e^+}$, $\phi^c_{e^+}$, $\theta^c_{e^-}$, $\phi^c_{e^-}$, $\theta^c_{\gamma+}$, and $\theta^c_{\gamma-}$ in terms of the scattering angles θ^c_+, θ^c_-, and ϕ^c_-. Recall that the angles θ^c_+ and θ^c_- are found from Eqs. (3.117) and (3.105b), respectively. The angle ϕ^c_+ is the scattering azimuthal angle of the cross section Eq. (3.112), and it too is obtained by application of the Monte Carlo method [Eq. (3.122)]. But first, the equations of Eq. (3.119) are solved (see Appendix D) yielding the polar and azimuthal angles in the space momentum vectors [Eq. (3.111)] of the e^-e^+ pairs. For the positron

$$\theta^c_{e^+} = -\arcsin\left(\frac{\cos\theta^c_+}{\cos\phi^c_{e^+}}\right) \ , \tag{3.120}$$

$$\phi^c_{e^+} = \arctan\left[\frac{-D_2 + (D_2^2 - 4D_1D_3)^{1/2}}{2D_1}\right] \ , \tag{3.121a}$$

where

$$D_1 \equiv \cos^2\theta^c_+ \sin^2\theta^c_+ \ , \tag{3.121b}$$

$$D_2 \equiv 2\cos\theta^c_+ \sin\theta^c_+ \sin\phi^c_+(1-\cos^2\theta^c_+) \ , \tag{3.121c}$$

$$D_3 \equiv 1 + \cos^2\theta^c_+(\cos^2\theta^c_+ - 2) + \sin^2\theta^c_+\cos^2\phi^c_+(\cos^2\theta^c_+ - 1) \ . \tag{3.121d}$$

Since by Eqs. (3.105d) and (3.105e),

$$\theta^c_{e^-} = \pi - \theta^c_{e^+} \ , \tag{3.105d$'$}$$

$$\phi^c_{e^-} = \phi^c_{e^+} \pm \pi \ , \tag{3.105e$'$}$$

the above angles for the positron, Eqs. (3.120) and (3.121), are sufficient to give the polar and azimuthal angles of the negatron.

The scattering azimuthal angle ϕ^c_+ [cf. Eq. (3.97)] of Eqs. (3.121c) and (3.121d) is now found below. Note that this azimuthal angle has been integrated over from 0 to 2π in the cross section of Eq. (3.112). Thus, the probability that the positron be emitted at the angle ϕ^c_+ in the c.m. frame is given by

$$\frac{\phi^c_+}{2\pi} = G_6 \ , \tag{3.122}$$

where G_6 is a random number between 0 and 1 [cf. Eq. (3.45)].

In summary, the energy of the positron in the c.m. frame $\varepsilon^c_+ (= \varepsilon^c_- = \varepsilon^c_{\gamma 1} = \varepsilon^c_{\gamma 2})$ is given by Eq. (3.110), and the magnitudes and space momentum vectors of the e^-e^+ pair in the c.m. frame are given by Eqs. (3.104) and (3.111), respectively. The angles of the momenta in Eq. (3.111) are given by Eqs. (3.120), (3.121), (3.105d$'$), and (3.105e$'$). To conclude this section, perform a Lorentz transformation on the above four-momentum components of the e^-e^+ pairs in the c.m. frame, to get these parameters as measured by a LF observer; this is achieved by making the following replacements in the transformations of Eq. (3.88):

$$\varepsilon^R_+ \to \varepsilon^c_+, (p^R_+)_r \to (p^c_+)_r, \text{ etc.} \ , \quad \gamma_p \to \gamma_{\text{c.m.}} \ , \tag{3.123}$$

where $\gamma_{\text{c.m.}}$ and $\beta_{\text{c.m.}} \equiv (\beta_r, \beta_\Theta, \beta_\Phi)$ are of Eq. (3.106); similar equations can be written for the four-momentum components of the negatron.

The final conditions in the BLF of the e^-e^+ pairs are computed in the same way as the final conditions in the BLF for the previous PPP ($\gamma p \to e^-e^+p$): I then refer the reader to Sec. III B 4, from which the four-momenta in the BLF, and the distribution of the escaping pairs, can be obtained, using the LF measurements of Eq. (3.123).

IV. RESULTS

As results accumulated during this investigation of the Penrose mechanism, to see if it is capable of producing the observed radiation spectra of celestial objects we believe to be powered by black holes, in particular AGN, certain trends became evident. The Compton processes, consisting of scattering low energy UV ($\sim$ 5 eV) incoming photons, ranging to γ-ray ($\sim$ 1 MeV) photons, by target orbiting electrons, reveal the following. First, we find that the factor by which the total incoming photon energy gets boosted (i.e., the relative energy gained by the outgoing photons) is largest for the low energy UV incoming photons; however, the efficiencies defined in Eqs. (2.28b), (2.30), and (2.31), as we shall see below, suggest that this is not a favorable Penrose Compton scattering (PCS). Nevertheless, these UV photons are consistent with the characteristic "blue bump" seen in the optical and UV spectra of AGN observations. This blue bump is believed to be a feature intrinsic to the photon emission from the accretion disk. In my model, these UV photons that fall into the ergosphere, undergo Compton scattering events, and escape with x-ray energies as high as $\sim$ 218 keV. These UV photons probably originate in the "outer" and "middle" regions of the classical thin accretion disk, as defined in Ref. [37]. Second, for the distribution of moderate energy incoming photons $\sim$ 30 keV (soft x rays) to $\sim$ 150 keV (hard x rays), after the scattering events, from about 75% up to 99% escape with energies as high as $\sim$ 12 MeV, always with a relative energy gain. These moderate energy photons, energies consistent with the theoretical temperatures of thin disk/ion corona accretion models (see Sec. I B), seem to be favorable in extracting energy by way of PCS. Third, for a distribution of high energy incoming photons $\sim$ 1 MeV (soft γ rays) and equatorially orbiting target electrons, about 70% of the scattered photons can escape with energies as high as $\sim$ 4 MeV; however, the total distribution of these incoming γ-ray photons gives up energy to the KBH (i.e., no relative energy is gained); PCS does not favor such initial conditions. On the other hand, for

the same distribution of incoming photons of energy ~ 1 MeV and nonequatorially orbiting target electrons, up to $\sim 98\%$ of the scattered photons can escape with energies as high as ~ 22 MeV, where relative energy is gained by the outgoing photons, making this a favorable PCS. Now, in the $\gamma\gamma \to e^-e^+$ processes, the incoming photons are allowed to have energies ranging from 3.5 keV to 10 MeV, and they undergo scatterings with orbiting photons that are allowed to have energies ranging from 3.4 MeV to 2.146 GeV. In these cases, up to $\sim 50\%$ of the scattered pairs escape with energies as high as ~ 2 GeV. Note that such high energy orbiting photons are consistent with those produced by processes in the accretion disk [12], and then are blueshifted, as they follow null geodesics through the ergosphere, by a factor $\simeq 52$ at the photon orbit. Finally, in the $\gamma p \to e^-e^+p$ processes the results were not very promising, as will be discussed below: none of the pairs were allowed to escape. Nevertheless, in the PCS and PPP ($\gamma\gamma \to e^-e^+$), the results were very promising, and they are sufficient to explain the mysterious energy source of quasars and other AGN.

Before presenting these results in details, it must be mentioned here that, in the past, energy extracted due to a Penrose process has been defined as the rotational energy extracted from a KBH when the initially orbiting target particle is put on a negative energy "captured" plunge trajectory [3,21]. In these present scattering processes, by comparing the sum of the energies of the incident particles in the BLF, for a given event, with the energy of the escaping particle, it is clear that the measured energy of the escaping particle above this sum is classical Penrose rotational extracted energy. However, what should one call the process when the target particle recoils to give up some of its orbital energy to the escaping particle, with the target particle (although not being put on a negative energy captured plunge trajectory) being put on a positive energy captured plunge trajectory [21]: as I have found in some of these Compton scattering events? Or by what name should the process be called in which the total energy of the target orbiting particle and incident particle is given to the newly created, possibly, escaping particles: as I have found in the $\gamma\gamma \to e^-e^+$ processes? The answers to these questions are given in the following. Due to the motion of a particle against the flow of spacetime, which creates frictional-like forces (that arise because inside the ergosphere the angular momentum of the KBH and the curvature of spacetime, force particles to rotate in the direction that the hole rotates), the recoil of a target particle still however extracts rotational energy, even though the target particle may not be put on a negative energy orbit. In these cases, for example in the Compton scattering events, the escaping photon energy will be less than the sum of the energies of the target electron and infalling photon, appearing as if no Penrose rotational energy was extracted—remember that any energy above this sum is defined to be classical Penrose extracted energy. But, in fact, due to the so-called friction set up by the frame dragging and the recoil of the target initially orbiting electron, rotational energy was indeed extracted by (or transferred to) the escaping photon. Thus, because an observer at infinity observes in principle a low energy particle (say, infalling from an accretion disk) participating in a scattering event with a bound orbiting particle inside the ergosphere, and then the scattered particle being allowed to escape to infinity with considerably more mass-energy than the original infalling low energy particle, as in the PCS, I will classify such scattering events as "quasi-Penrose" processes. Also the PPP ($\gamma\gamma \to e^-e^+$), I classify such events as quasi-Penrose processes: my reason for this will be discussed fully in Sec. IV C 2. In support of the above classification, it is important to note that, the extracted (or excess) energy, the scattered particle escapes with, may have been forever trapped by the KBH, had the scattering event not occurred [21]. Moreover, in the case of PCS, at $r_{\rm MB}$, this excess energy is ~ 70 times more than the scattered photon energy, had the scattering occurred outside the ergosphere or at infinity (flat spacetime). So in summary, the two classifications, resulting in particles escaping to infinity with extracted energy from the KBH, are the following: scattering events in which the target particle is put on a negative energy captured plunge are classified as classical Penrose processes, and all others as quasi-Penrose processes. Thus, with the above preliminaries in mind, I now proceed to present the results.

A. Inverse Compton scattering

1. *Energy and momentum spectra*

The results presented here are for the scattering of 2000 radially infalling photons by orbiting electrons in the ergosphere. The mass of the KBH generally used in the calculations is $10^8 M_\odot$. Note that the Penrose mechanism can operate for any size KBH irrespective of the mass of the black hole. The target electrons are located at $r_{\rm MS}$ or $r_{\rm MB}$, having orbital energies of 0.349 MeV or 0.539 MeV, respectively, for $Q_e = 0$, where Q_e is the Q value of the orbiting electron [Eq. (2.6)]; notice in Fig. 1(b) that, as $Q_e (\equiv Q_e^*)$ goes to zero the energies go to the above given values, as would be expected for equatorial orbits at constant radii. For nonequatorial orbits, as can be seen in Fig. 1(b), the orbital energy of the particle increases with increasing Q_e. For example, when $\sqrt{Q_e} = 12.43 M m_e$ (with $G = c = 1$), the target electrons located at $r_{\rm MS}$ and $r_{\rm MB}$ have the increased orbital energies of 3.132 MeV and 5.927 MeV, respectively (cf. with the above equatorial values). Now, the initial infalling photon distributions are allowed to have monochromatic energies ranging from 5 eV to 1 MeV. Moreover, when not set equal to zero, the temperature of the blackbody distribution of initial photons, $T_{\rm ph}$, and the finite temperature of the orbiting target electrons, T_e, are given the values 3.5×10^8 K or 5.8×10^8 K. These above initial energies and temperatures are compatible with the thin disk/ion corona models (see Sec. I B).

The final energies of escaping scattered photons as measured by an observer at infinity Eq. (3.47a) are put into energy bins, and the spectra [the number of photons $N(E)$ per average energy interval versus the average en-

ergy] are plotted as illustrated in Fig. 2. The vertical error bars of such plots are the standard statistical $\sqrt{N}$ errors, involved in a Monte Carlo calculation [4], and the horizontal bars give the energy widths of the bins.

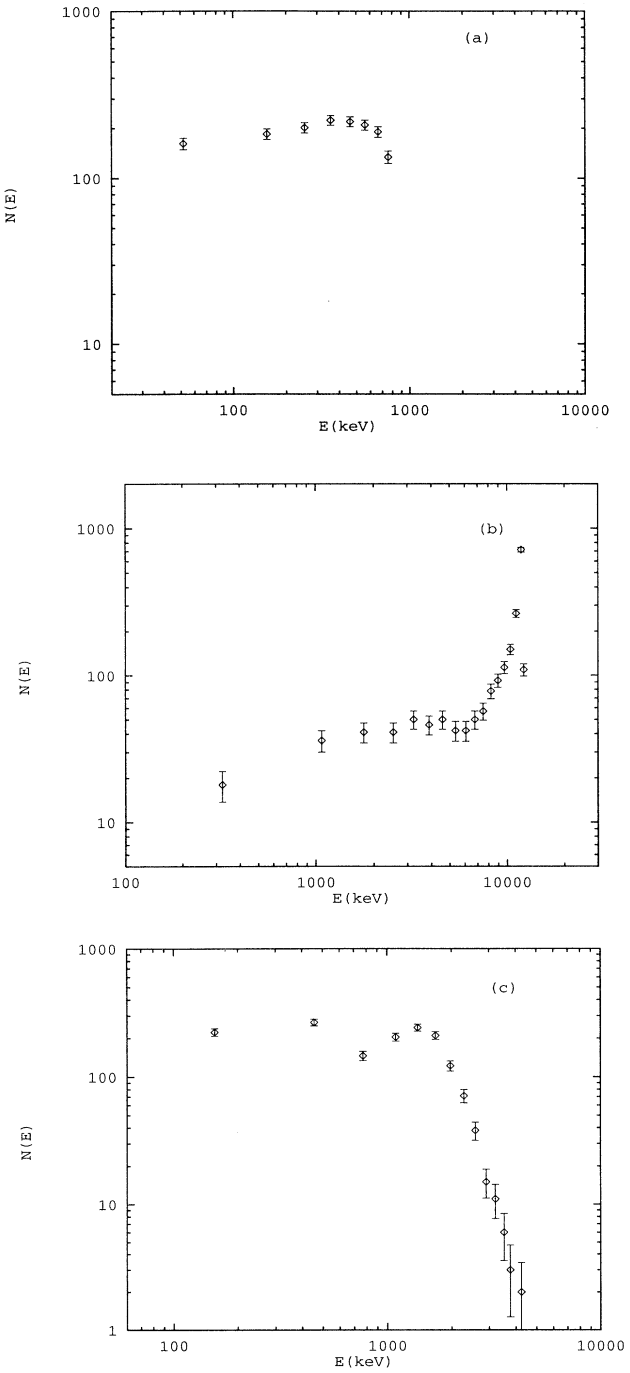

FIG. 2. Compton scattering at r_{MB}. (a) $E_{\mathrm{ph}} = 0.03$ MeV and $E_e = 0.539$ MeV; No. 3 of Tables I and II. (b) Using nonequatorial target electrons: $E_{\mathrm{ph}} = 0.03$ MeV and $E_e = 11.79$ MeV; No. 10. (c) Using blackbody incoming photons, thermal target electrons: $T_{\mathrm{ph}} = T_e = 5.8 \times 10^8$ K; No. 19.

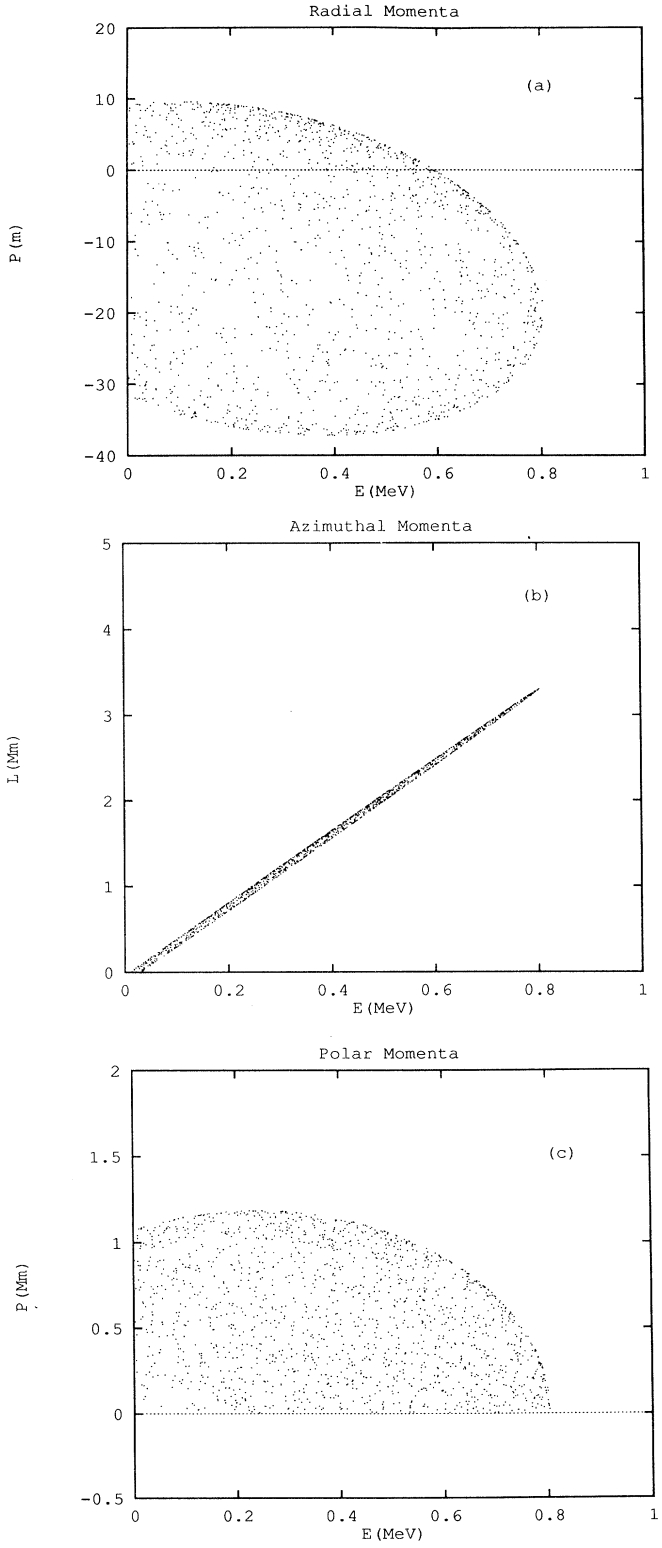

FIG. 3. Compton scattering: scatter plots showing space momenta of scattered escaping photons (each point represents a scattering event). (a) Radial momentum components: $(P'_{\mathrm{ph}})_r$ vs E'_{ph}. (b) Azimuthal angular momentum components: L'_{ph} vs E'_{ph}. (c) Polar angular momentum components $(\equiv \sqrt{Q'_{\mathrm{ph}}})$: $(P'_{\mathrm{ph}})_\Theta$ vs E'_{ph}. Same as Fig. 2(a) and No. 3 of Tables I and II.

Specific cases (or computer runs) are given in Table I. Table I gives a summary of the scattering events and the resulting spectral distributions (I have indicated these by numbers): Nos. 1–6 give the spectral distributions of the photons, scattered by equatorial orbiting target electrons at $r_{\rm MB}$; Nos. 7–12 give the distributions of escaping photons that have been scattered by nonequatorial orbiting target electrons at $r_{\rm MB}$; Nos. 13–15 give the distributions of escaping photons when the scattering occurs at $r_{\rm MS}$; Nos. 16 and 17 give the photon distribution after scattering by orbiting electrons of a finite kinetic temperature T_e ($\neq 0$ K); Nos. 18 and 19 give the escaping distributions resulting from scattering initial blackbody photons of temperature $T_{\rm ph}$, by orbiting cold ($T_e = 0$ K) electrons in one case, and by hot electrons of a finite temperature in the others, respectively; $E_{\rm peak}$ is the energy value where most of the escaping photons are emitted, and $E_{\rm max}$ is the maximum energy carried by the escaping photons. The final space momentum components of the escaping photons in the BLF, from scattering monochromatic photons of initial energy $E_{\rm ph} = 30$ keV, off cold target electrons orbiting at $r_{\rm MB}$, are presented in Fig. 3; Fig. 4 gives these space momenta after the same monochromatic photons are scattered off nonequatorial target electrons. Both Figs. 3 and 4 are scatter plots resulting from the application of the Monte Carlo method, which yields individual four-momentum components for the scattered particles.

Several types of efficiencies are established in Sec. II C: the absolute efficiency of Eq. (2.28b), the W efficiencies of Eq. (2.30), and the PS efficiency of Eq. (2.31). As we shall see below, each of these efficiencies reveals an important aspect of the scattering process. These efficiencies for specific cases are presented in Table II, where the case numbers correspond to those on Table I. Note that, $\epsilon^{\rm PS}_{\rm peak}$ is evaluated at where most of the energy is emitted, and $\epsilon^{\rm PS}_{\rm max}$ is evaluated at the maximum energy of the escaping particles.

The results presented in Figs. 2–4, along with Tables I and II, reveal the following:

a. r_{MS} scattering compared to r_{MB} scattering. The maximum energy attainable by the photons, the W efficiencies, and the absolute efficiency increase as one scatters closer to the horizon (cf. Nos. 3 [Fig. 2(a)], 9, and 10 to 13–15, respectively, on Tables I and II). Moreover, comparing the PS efficiencies for the cases mentioned above, one can see that classical Penrose energy extraction is important at $r_{\rm MB}$, yet not at $r_{\rm MS}$: here, only quasi-Penrose energy extraction occurs, in which the target electrons, more than likely, recoil to captured plunge orbits of, lesser, positive energies [21]. (The radii $r_{\rm MB}$ and $r_{\rm MS}$ are defined in Sec. III A 1.)

b. Change in energy of the initial photon. Higher energies of the infalling photons produce higher maximum energies for the escaping photons. However, the relation

TABLE I. The Compton scattering processes: resultant spectra.

	$N = 2000$[a]		$a/M = 0.998$	$r/M = 1.089$		
Case no.	$E_{\rm ph}$(MeV)	E_e(MeV)	$P_{e\Theta}(Mm_e)$[b]	$N_{\rm es}$[c]	$E_{\rm peak}$(MeV)	$E_{\rm max}$(MeV)
1	5.11×10^{-4}	0.539	0	1707	0.025	0.053
2	0.0035	0.539	0	1635	0.128	0.261
3	0.03	0.539	0	1521	0.665	0.759
4	0.05	0.539	0	1496	0.459	0.960
5	0.15	0.539	0	1442	0.459	1.563
6	1.0	0.539	0	1390	0.510	3.956
7	0.0035	5.927	12.43	1997	5.070	5.250
8	0.0035	11.79	24.79	2000	10.77	11.07
9	0.03	5.927	12.43	1988	5.948	6.253
10	0.03	11.79	24.79	1995	11.86	12.21
11	5 eV	5.927	12.43	1971	0.016	0.016
12	5 eV	11.79	24.79	1995	0.022	0.218
13[d]	0.03	0.349	0	1527	0.155	0.325
14[d]	0.03	3.132	12.43	1980	2.968	3.114
15[d]	0.03	6.218	24.79	1991	5.950	6.195
16	0.03	0.539	3.5×10^8 K[e]	1614	0.559	1.272
17	0.05	0.539	5.8×10^8 K[e]	1589	0.307	2.494
18	5.8×10^8 K[f]	0.539	0	1454	0.766	1.888
19	5.8×10^8 K[f]	0.539	5.8×10^8 K[e]	1559	1.387	4.242

[a]Number of infalling photons used in the scatterings.
[b]Nonzero values indicate nonequatorial orbiting target electrons: $P_{e\Theta} \equiv \sqrt{Q_e}$.
[c]Number of scattered photons escaping.
[d]Scattering at $r_{\rm MS}$: $r/M = 1.2$.
[e]Maxwellian temperature of thermal target electrons.
[f]Photon temperature of blackbody distribution.

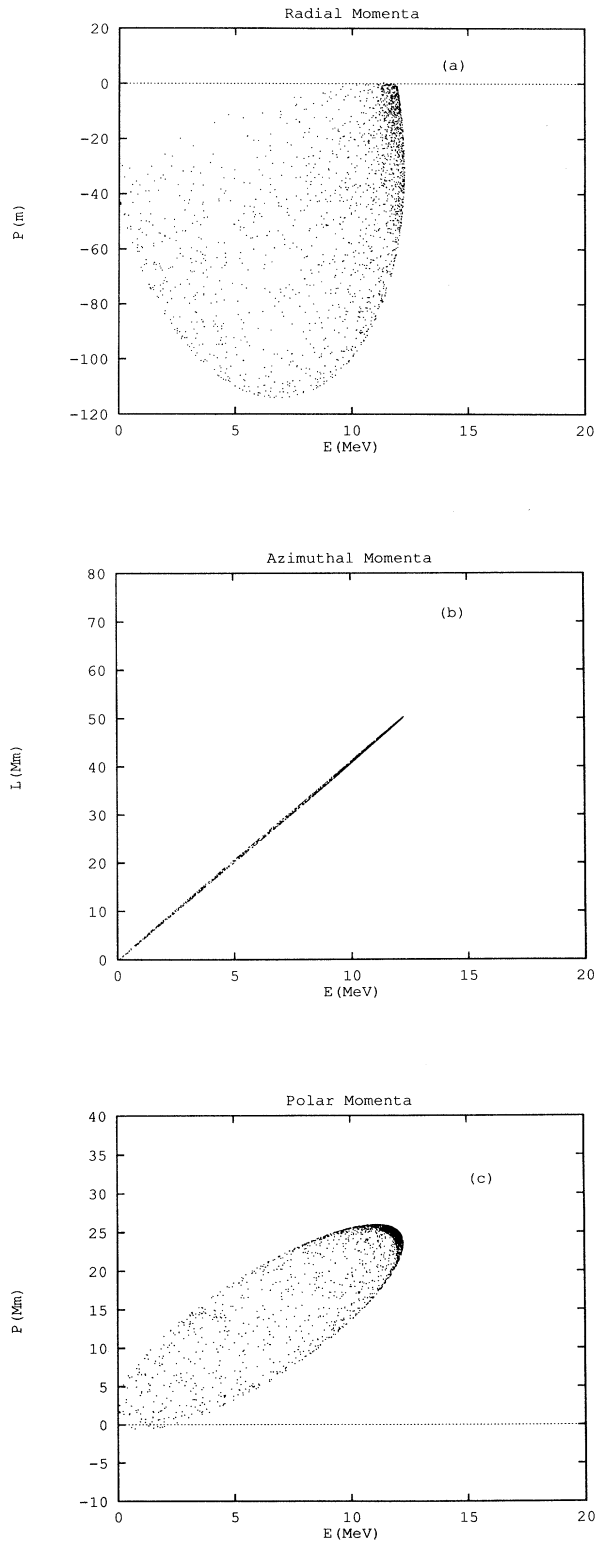

FIG. 4. Compton scattering: scatter plots showing space momenta of escaping photons scattered by nonequatorial orbiting target electrons (each point represents a scattering event). Refer to Fig. 3, for further explanations of momentum components: (a) radial, (b) azimuthal, and (c) polar. Same as Fig. 2(b) and No. 10 of Tables I and II.

between the initial energy and the final maximum energy is not linear (cf. the second and last columns of Table I). Notice that the corresponding W efficiencies of Table II decrease with increasing initial photon energy, suggesting that the Penrose mechanism has a favorable energy range. Also it is found that, to a BLF observer, as the initial photon energy is increased, more scattered photons of negative energies arise (of course, these negative energy photons do not escape from the ergosphere). In Nos. 4–6 on Table I, there is a noticeable peak that occurs around 0.5 MeV at $r_{\rm MB}$ for the initial photon energies in the range of 50 keV$\leq E_{\rm ph} \leq$ 1 MeV. This peak is also evident in the scattering at $r_{\rm MS}$, occurring around 0.3 MeV for incoming photons with initial energies in the range of 50 keV$\leq E_{\rm ph} \leq$ 1 MeV. The energy values of these peaks are nearly equal to the orbital energies of the target electrons at the scattering radii: at $r_{\rm MB}$, $E_e = 0.539$ MeV and at $r_{\rm MS}$, $E_e = 0.349$ MeV; just how near a peak is to the energy value of the target orbiting electrons depends on the initial energies of the incident photon distribution. Again, as mentioned earlier in this section, the excess energy of the scattered photon, above the sum of the energy of the target electron and the initial photon, is the classical Penrose extracted rotational energy.

c. Orbiting electrons and incoming photons with finite temperatures. A finite temperature given to the electrons that scatter monochromatic photons (1) increases the W

TABLE II. The Compton scattering processes: efficiencies.

Case no.	$\epsilon^{W}_{\rm BLF}$ [a]	ϵ^{W} [b]	$\epsilon^{\rm PS}_{\rm peak}$ [c]	$\epsilon^{\rm PS}_{\rm max}$ [c]	$\epsilon^{\rm abs}$ [d]
1	45.7	23.8	−0.95	−0.90	0.04
2	30.7	22.1	−0.76	−0.52	0.20
3	10.2	17.0	0.17	0.33	0.54
4	7.34	15.3	−0.22	0.63	0.62
5	3.46	11.4	−0.33	1.27	0.75
6	0.98	5.51	−0.67	1.57	0.64
7	925	22.0	−0.15	−0.12	0.55
8	207×10^{1}	22.2	−0.09	−0.06	0.61
9	157	21.4	−0.002	0.05	0.79
10	315	21.9	0.003	0.03	0.80
11	310×10^{1}	22.1	−0.997	−0.997	0.003
12	211×10^{2}	22.2	−0.998	−0.99	0.01
13	4.28	5.77	−0.59	−0.14	0.34
14	69.3	5.31	−0.06	−0.02	0.66
15	146	5.38	−0.05	−0.01	0.70
16	14.4	18.3	···	···	0.75
17	14.8	19.1	···	···	1.21
18	3.53	11.3	···	···	0.72
19	6.59	15.3	···	···	1.29

[a] $\left(\frac{\text{total outgoing photon energy}}{\text{total incoming photon energy}}\right)$ as measured by a BLF observer.
[b] $\left(\frac{\text{W efficiency in the BLF}}{\text{W efficiency in the LNRF}}\right)$.
[c] "+" value indicates classical Penrose extraction of rotational energy.
[d] $\left[\frac{\text{total outgoing photon energy}}{\text{total input energy (electrons+photons)}}\right]$.

and absolute efficiencies of Table II, and (2) increases the maximum energies of escaping photons (cf. Nos. 3 and 4 to 16 and 17, respectively on Table I; notice that the PS efficiencies are not given for the thermal scattering cases, Nos. 16–19, because, these efficiencies make sense only for monochromatic initial energy distributions or single scattering events [see Eq. (2.31)]). When the incoming photons, described by a blackbody distribution of particles at a finite temperature, scatter off cold target electrons, the resulting spectrum acquires a thermal-like (as related to a Planck curve) appearance; cf. No. 18 to 4 (here the initial photons have a monochromatic energy equivalent to the blackbody photon temperature $T_{\rm ph} = 5.8 \times 10^8$ K). When both the target electrons and the incoming photons are given finite temperatures, Fig. 2(c), the maximum energy of the escaping photons increases by a factor of ~ 4, from that of the equivalent case with $T_{\rm ph} = T_e = 0$ (cf. No. 19 to 4).

d. Nonequatorial orbiting target electrons. When the nonequatorial orbiting trajectories are used for the target electrons (Appendix A), the scattered photons can escape with higher energies. These escaping energies increase with increasing Q values of the target electron orbits. Again, as in the cases of equatorial target electrons, the escaping photon distribution tends to peak around the target electron orbital energy [see Fig. 2(b) and Nos. 9, 10, 14, and 15 of Table I].

e. The efficiencies compared. The efficiencies of Table II, to be used along with Table I in the comparisons for the different cases mentioned below, are defined as follows. The W efficiencies, $\epsilon^W_{\rm BLF}$, of Eq. (2.30b), tells us the energy gained/loss by the incoming distribution of scattered photons in the BLF; and ϵ^W, of Eq. (2.30c), relates this energy gained/loss, to that which is measured by a LNRF observer [Eq. (2.30a)]. The PS efficiencies, $\epsilon^{\rm PS}_{\rm peak}$ and $\epsilon^{\rm PS}_{\rm max}$, as given in Eq. (2.31), tell us whether or not classical Penrose energy was extracted: a positive value indicates classical Penrose energy extraction; a negative value indicates quasi-Penrose extraction. These are evaluated at the peak and maximum energy values, $E_{\rm peak}$ and $E_{\rm max}$, respectively (of Table I). On the other hand, the absolute efficiency, $\epsilon^{\rm abs}$ as given in Eq. (2.28b), tells how effective the total input energy is converted into energy that can be radiated away.

For scattering at $r_{\rm MB}$, the radius of marginally bound orbits, the W efficiencies convey the following. Notice that for equatorial target electrons, $\epsilon^W_{\rm BLF}$ [Eq. (2.30b)] is largest for the low energy initial photons (cf. Nos. 1–6), and as the total energy of the initial photons is increased, $\epsilon^W_{\rm BLF}$ decreases. This suggests that PCS works more effective for infalling photons with energies $\lesssim 150$ keV; that is, initial photon distributions with energies above this value give up energy in the scattering process, as measured by a BLF observer (cf. No. 6).

On the other hand, still at $r_{\rm MB}$, the absolute efficiency and the PS efficiencies convey the following. For the equatorial target electrons of fixed orbital energies, as the total energy of the initial photons is increased, $\epsilon^{\rm abs}$ starts very low for the low initial energy (No. 1), reaches a maximum for the moderate initial energy (No. 5), then declines at higher initial energies (No. 6), as would be expected, based on the above suggestion that the PCS works best for moderate initial photon energy (Nos. 3–5). Likewise, under the same initial conditions, both PS efficiencies start negative in Nos. 1 and 2 (indicating only quasi-Penrose energy extraction, in which the target electrons are put on plunging trajectories of positive energy orbits); both become positive in No. 3 (indicating classical Penrose energy extraction becomes dominant, in which the target electrons are put on negative energy plunges); then in Nos. 4–6 only $\epsilon^{\rm PS}_{\rm max}$ is positive (indicating that classical Penrose energy extraction may no longer be dominant). For the nonequatorial target electrons we find similar behaviors for the efficiencies (cf. Nos. 7–12).

Now at the scattering radius $r_{\rm MS}$, the PS efficiencies suggest that no energy is extracted by classical Penrose processes; nevertheless, since the energy boosts and the absolute efficiencies can get to be fairly large, as indicated by $\epsilon^W_{\rm BLF}$ and $\epsilon^{\rm abs}$, respectively, such quasi-Penrose processes are expected to contribute, some, to the overall emitted photon spectrum (cf. Nos. 13–15).

Of the cases considered, for equatorial targets, the efficiencies of Table II seem to suggest that the PCS mechanism gives the most favorable results for the cases of (Nos. 3–5): For favorable results we want both $\epsilon^W_{\rm BLF}$ and $\epsilon^{\rm abs}$ as large as possible, and, as far as classical Penrose extraction is concerned, we desire $\epsilon^{\rm PS}_{\rm peak}$ and $\epsilon^{\rm PS}_{\rm max}$ to have large positive values. Now concerning the nonequatorial target electrons, using a similar argument to that given above, the most favorable results (out of the cases presented here) are given for the cases of Nos. 9 and 10. Notice that in these favorable cases the incoming photons have moderate (soft x-ray) energies. In addition, notice that the highest absolute efficiency is given for the case of thermal initial photons and thermal target electrons [see Fig. 2(c) and No. 19]. Unfortunately, in the thermal cases, simple values for the PS efficiencies cannot be found; however, for the thermal cases presented here (Nos. 16–19), I presume that these efficiencies will not be too much different from the cases of Nos. 3 and 4.

2. A typical scattering event (PCS)

In this section, we will follow the scattering process of one Compton scattering event from the initial photon to the final photon. This event is typical of the other scattering events. The initial photon has energy $E_{\rm ph} = 0.03$ MeV, and the target equatorial orbiting electron at $r = r_{\rm MB}$ has energy $E_e = 0.539$ MeV (marginally bounded), in the BLF. In the LF the photon energy increases to $\varepsilon_{\rm ph} = 0.959$ MeV [Eq. (3.12)] and in the ERF it increases to $\varepsilon^R_{\rm ph} = 1.427$ MeV [Eq. (3.21a)]. Application of the Monte Carlo method to the cross section [Eq. (3.41)] gives the scattering angles $\delta^R = 60.19°$ and $\alpha^R = 24.02°$ from Eqs. (3.44) and (3.45), respectively. The final energy of the photon is as follows: In the ERF, $\varepsilon^{R'}_{\rm ph} = 0.594$ MeV [Eq. (3.23)]; this transforms to $\varepsilon'_{\rm ph} = 0.991$ MeV [Eq. (3.46a)] in the LF; and a BLF observer measures

this final energy to be $E'_{\rm ph} = 0.762$ MeV [Eq. (3.47a)]. Upon comparing the final energy $E'_{\rm ph}$ and the initial energy $E_{\rm ph}$ given above, notice the energy gained by the final photon in the BLF ($E'_{\rm ph} = 25.4E_{\rm ph}$)—these energies compared in the LF give that $\varepsilon'_{\rm ph} = 1.033\varepsilon_{\rm ph}$. Momentum components resulting from the distribution of initial monochromatic photons, in which the case just considered is represented by a point on the scatter plots, are presented in Fig. 3; and these momenta belong to members of the spectrum in Fig. 2(a). Notice in Figs. 3(a) and 4(a) that a large number of particles with negative radial momenta escapes (this may be important in astrophysical jet formation). Compare Fig. 3, scattering by equatorial target electrons, with Fig. 4, scattering by nonequatorial target electrons, and notice how the magnitudes of the polar coordinate angular momenta $(P'_{\rm ph})_\Theta$ of the escaping photons increase for the nonequatorial cases, as would be expected; also notice the one-sided distribution in the polar direction (this too may be of astrophysical significance as related to the jets; this will be discussed in Sec. V).

B. γ-ray–proton pair production

1. *Energy and momentum spectra*

In these $\gamma p \rightarrow e^- e^+ p$ processes, for a distribution of 2000 initial radially infalling photons of monochromatic energy $E_\gamma = 40$ MeV in the BLF, none of the scattered pairs are allowed to escape, and thus, there is no need to present energy and momentum spectra here; nevertheless, detailed results are presented below, along with suggestions to make this, if possible, a feasible PPP process. Note that the energy value used for the infalling γ-ray photon is consistent with the theoretical suggested value (Sec. I B). Because of the approximations that ε_γ, ε_+, $\varepsilon_- \gg \mu_e$, used in the integration of the cross section [Eq. (3.58)], it is found that the following condition must be satisfied: $\varepsilon_\gamma, \varepsilon_+, \varepsilon_- > 200$ MeV in the LF ($>\sim 6$ MeV in the BLF). On the other hand, if the energy of the γ ray is too high ($\gtrsim 60$ MeV in the BLF or $\gtrsim 1.918$ GeV in the LF), the assumption that the recoil energy given to the proton is negligible [see Eq. (3.62)] cannot be maintained, since the energy of the photon in the LF will be greater than the rest-mass-energy of the proton ($\simeq 938$ MeV). Thus, it is found that a feasible range of initial energies for the γ ray in the BLF is 10 MeV$\leq E_\gamma \leq 60$ MeV, using the cross section given by Eq. (3.60), and if the scattering is done near the marginally bound radius $r_{\rm MB}$ ($\sim 1.09M$). However, for a radially infalling γ ray, with such high energy in this range, the radial momentum component is too high at the scattering event for the azimuthally directed proton to scatter any of the $e^- e^+$ pairs into the positive radial direction, that which is needed to escape (in particular at $r_{\rm MB}$, since pairs penetrating this radius must plunge directly into the black hole). It remains to be seen what happens when the γ ray is initially infalling with positive or negative azimuthal direction, at the scattering event. It is possible that the electron pair may then be allowed to escape, but with only the energy of the infalling γ ray, i.e., without any energy being extracted from the KBH. This limitation on the escaping energies of the pair can be expected because of the assumption made that the recoil energy given to the proton is negligible [Eq. (3.62)], therefore, making any energy exchange between the γ ray and orbiting proton impossible. If this be the case, then, this assumption must be taken out of the cross section (more on this later in Sec. V B 2).

2. *A typical scattering event ($\gamma p \rightarrow e^- e^+ p$)*

In order to shed some light on the above results, one pair production event is followed and various parameters are presented (as done for Compton scattering in Sec. IV A 2), with this event being typical of the others. The scattering occurs at the radius $r = 1.09M$ ($\sim r_{\rm MB}$). The initial energy of the radially infalling γ ray is $E_\gamma = 40$ MeV, and the energy of the orbiting proton is $E_p = 966.9$ MeV, as measured by a BLF observer. A LF observer measures this initial γ-ray energy as $\varepsilon_\gamma = 1.251$ GeV [Eq. (3.56)], and in the PRF, this energy is measured as $\varepsilon^R_\gamma = 1.837$ GeV [Eq. (3.57a)]. Application of the Monte Carlo method to the cross section [Eq. (3.60)], and then using the root-mean-square angle of Eq. (3.66a) to find the scattering angles that the pairs make with the primary γ ray in the PRF, one finds the following. The scattering angles are $\theta^R_- = 0.045°$ and $\theta^R_+ = 0.158°$ for the negatron and positron, respectively; the corresponding maximum angles of Eq. (3.67) used in Eq. (3.66a) were $\theta^R_{-\,\rm max} = 9.43°$ and $\theta^R_{+\,\rm max} = 12.97°$, respectively. These angles were obtained by setting $\theta^R_{-\,\rm max}$ (or $\theta^R_{+\,\rm max}$) equal to 8.594° plus Eq. (3.66e) for the negatron (or positron): it turns out that the results depend very little on the choice of these maximum angles. The energies of the pairs in the LF are measured to be $\varepsilon_- = 1.05$ GeV and $\varepsilon_+ = 201.0$ MeV. To a BLF observer these energies are measured as $E_- = 33.76$ MeV and $E_+ = 6.828$ MeV; thus, we see that the sum of the pair energies approximately equals E_γ (= 40 MeV), indicating negligible energy gain for the pair by way of the Penrose process. This effect of getting back approximately only the energy of the incident γ rays, for the $e^- e^+$ pair, is found to occur in all the $\gamma p \rightarrow e^- e^+ p$ events. Again, the reason for this is probably the assumption that negligible recoil energy is given to the proton [Eq. (3.62) used in Eqs. (3.63) and (3.77b)]. It may be worthwhile mentioning here that in order to get an effective Penrose process, some recoil into a retrograde and/or negative energy orbit of the proton must be allowed.

C. γ-ray–γ-ray pair production

1. *Energy and momentum spectra*

As in the above scattering processes, 2000 initial radially infalling photons participate in pair production

events. In most cases, monochromatic photons of initial energy in the range of 3.5 keV$\leq E_{\gamma 1} \leq$ 10 MeV, scatter off photons orbiting at the photon orbit with energies in the range 3.4 MeV$\lesssim E_{\gamma 2} \lesssim$ 2.146 GeV, as measured by a BLF observer; in the other cases, the infalling photons are from a blackbody distribution of finite temperature $T_{\rm ph}$. However, the acceptable lower limits of $E_{\gamma 1}$ and $E_{\gamma 2}$ are dependent on the threshold energy requirement of Eq. (1.2). The orbiting photon energy is given by (A20) and is plotted in Fig. 1(a). It is assumed here that these γ rays of the photon orbit have been initially blueshifted by the KBH to energies ($E_{\gamma 2}$) in the range as given above, and that they have the corresponding Q values ($Q_{\gamma 2}$) of the photon orbit [cf. Eq. (2.6)]. Note that the high energy γ rays of $E_{\gamma 2}$ are consistent with existing accretion disk models (see Sec. I C).

The energy spectra of the escaping e^-e^+ pairs are shown in Fig. 5; see also Table III (again, each scattering case is represented by a number). Corresponding efficiencies similar to those of Eqs. (2.28b) and (2.30) are expressed in Table IV. Numbers 1–18 give the distributions of escaping pairs when the infalling photons have monochromatic energies $E_{\gamma 1}$ in the range given above, and the target photons have orbital energies $E_{\gamma 2}$ in the range also given above, with corresponding Q values in the range of $0.099Mm_e \leq \sqrt{Q_{\gamma 2}} \leq 62.28Mm_e$. Case No. 19 gives the distribution resulting from infalling photons of blackbody temperature $T_{\rm ph} = 5.8 \times 10^8$ K and target photons having energy $E_{\gamma 2} = 10.75$ MeV. For completion, the space momentum components for case No. 8 of Tables III and IV, and Fig. 5(b), are presented in the scatter plots of Fig. 6.

The efficiencies presented in Table IV are defined generally in Sec. II C; however, here, briefly we will review their meaning, as they relate to the present scattering process. The W efficiencies $\epsilon^W_{\rm BLF}$ and $\epsilon^W_{\rm LF}$ give the ratios of the total energy of the escaping pairs to the total energy of the incoming photons in the BLF and LF, respectively; and ϵ^W reveals how these ratios are related [see Eq. (2.30c)]. The absolute efficiency $\epsilon^{\rm abs}$ expresses the ratio of the total energy of the escaping pairs to the total input energy: of the incident photons ($E^T_{\gamma 1} + E^T_{\gamma 2}$) used in the 2000 scattering events. The PS efficiencies, which do not appear in Table IV, are all negative, indicating that no classical Penrose energy is extracted in this PPP; however, quasi-Penrose energy is extracted.

The results presented in Nos. 1–19 of Tables III and IV, and Fig. 5 reveal the following:

a. Changing the energy of the infalling photon, $E_{\gamma 1}$. In most of the spectra a characteristic peak appears at an energy approximately equal to $\frac{1}{2}$ the orbital energy of the photon ($E_{\gamma 2}$). With a fixed orbital energy $E_{\gamma 2} (\gg E_{\gamma 1})$, and an increasing $E_{\gamma 1}$, the shapes of the spectra depend very little on $E_{\gamma 1}$ [cf. Fig. 5(c) to 5(d)]. However, when

TABLE III. The $\gamma\gamma \rightarrow e^-e^+$ processes: resultant spectra.

	$r_{\rm ph} = 1.074M$		$N = 2000$[a]		$a/M = 0.998$	
Case no.	$E_{\gamma 1}$(MeV)	$E_{\gamma 2}$(MeV)	$P_{\gamma 2\Theta}(Mm_e)$[b]	$N_{\rm es}$[c]	$E_{\rm peak}$(MeV)	$E_{\rm max}$(MeV)
1	0.0035	3.40	0.099	1326	1.782	2.209
2	0.03	3.40	0.099	1382	1.289	3.163
3	1.0	3.40	0.099	644	1.231	3.181
4	10	3.40	0.099	324	0.767	3.158
5	0.0035	10.75	0.312	1895	5.370	9.840
6	0.03	10.75	0.312	1812	4.653	10.44
7	10	10.75	0.312	845	1.303	10.34
8	0.0035	34.00	0.987	1964	17.35	32.87
9	1.0	34.00	0.987	1684	11.25	32.96
10	0.0035	206.7	6.0	1992	97.48	197.8
11	0.03	206.7	6.0	1984	106.0	199.9
12	0.0035	340.0	9.87	1995	170.8	318.5
13	0.03	340.0	9.87	1989	174.4	328.7
14	0.0035	854.1	24.79	1997	372.2	757.0
15	0.03	854.1	24.79	1992	432.6	818.3
16	1.0	854.1	24.79	1967	407.5	831.8
17	0.0035	2.146 GeV	62.28	2000	906.3	1.713 GeV
18	0.03	2.146 GeV	62.28	1997	1.068 GeV	2.026 GeV
19	3.5×10^8 K[d]	10.75	0.312	1743	4.60	10.44

[a]Number of infalling photons used in the scattering.
[b]$P_{\gamma 2\Theta} \equiv \sqrt{Q_{\gamma 2}}$, of the photon orbit.
[c]Number of escaping electrons (or positrons).
[d]Photon temperature of blackbody distribution.

the energies $E_{\gamma 1}$ and $E_{\gamma 2}$ are comparable, and $E_{\gamma 1}$ is allowed to increase there is a noticeable change in the spectra: The distribution around the characteristic peak (always at $\simeq \frac{1}{2}E_{\gamma 2}$) is flatter for low $E_{\gamma 1}$; and as $E_{\gamma 1}$ increases, the peak becomes more pronounced and occurs at a smaller energy than the characteristic peak (Nos. 1–4). In addition, the maximum energy of the escaping pairs is always $\sim E_{\gamma 2}$, depending little on increasing $E_{\gamma 1}$ (cf. $E_{\gamma 2}$ and $E_{\max}$ on Table III). The number of escaping particles decreases with increasing $E_{\gamma 1}$; this feature is more profound for lower energies of $E_{\gamma 2}$ (cf. Nos. 1–3 to 14–16 of Table III). Also, with increasing $E_{\gamma 1}$, the number of electrons (e^-e^+ pairs) with negative energies as measured by a BLF observer increases. Moreover, both the W efficiencies and the absolute efficiencies presented in Table IV decrease with increasing $E_{\gamma 1}$, for a fixed value of small $E_{\gamma 2}$: this is not true for $\epsilon^{\rm abs}$ when $E_{\gamma 2}$ is large (cf. corresponding case numbers on Tables III and IV).

b. Changing the energy of the orbiting photon, $E_{\gamma 2}$. First, the maximum energies of the escaping pairs, $E_{\max}$, increase with increasing $E_{\gamma 2}$, and is approximately equal to $E_{\gamma 2}$, as can be seen on Table III and in Fig. 5. Second, as $E_{\gamma 2}$ increases to values $\gg \mu_e$, the spectra become invariant and the distribution of the escaping electrons has a more pronounced characteristic peak ($\sim \frac{1}{2}E_{\gamma 2}$), as can be seen in Fig. 5. Finally, we notice in Table IV, the behavior of the efficiencies [Eqs. (2.28a), (2.30b), and (2.30c)] with increasing $E_{\gamma 2}$ are the following: $\epsilon^W_{\rm BLF}$, which give the ratio of the total escaping energy (of the e^-e^+ pairs) to the total infalling photon energy in the BLF, increase without bound; ϵ^W reaches a maximum value of 49.5, nearing the blueshift factor at the photon orbit [$e^{-\nu} \simeq 52$; see Eqs. (2.8d) and (2.10a)], as would be expected, since this efficiency is a measure of the relative difference between the BLF and LF; and $\epsilon^{\rm abs}$, which expresses the ratio of the total escaping energy ($E^T_+ + E^T_-$) to the total input energy ($E^T_{\gamma 1} + E^T_{\gamma 2}$), reaches a maximum of ~ 0.5, as would also be expected, since in these PPP processes, for radially infalling incident photons, one of the pairs usually escapes, while the other becomes trapped by the KBH.

c. Infalling blackbody photons. At high energies for

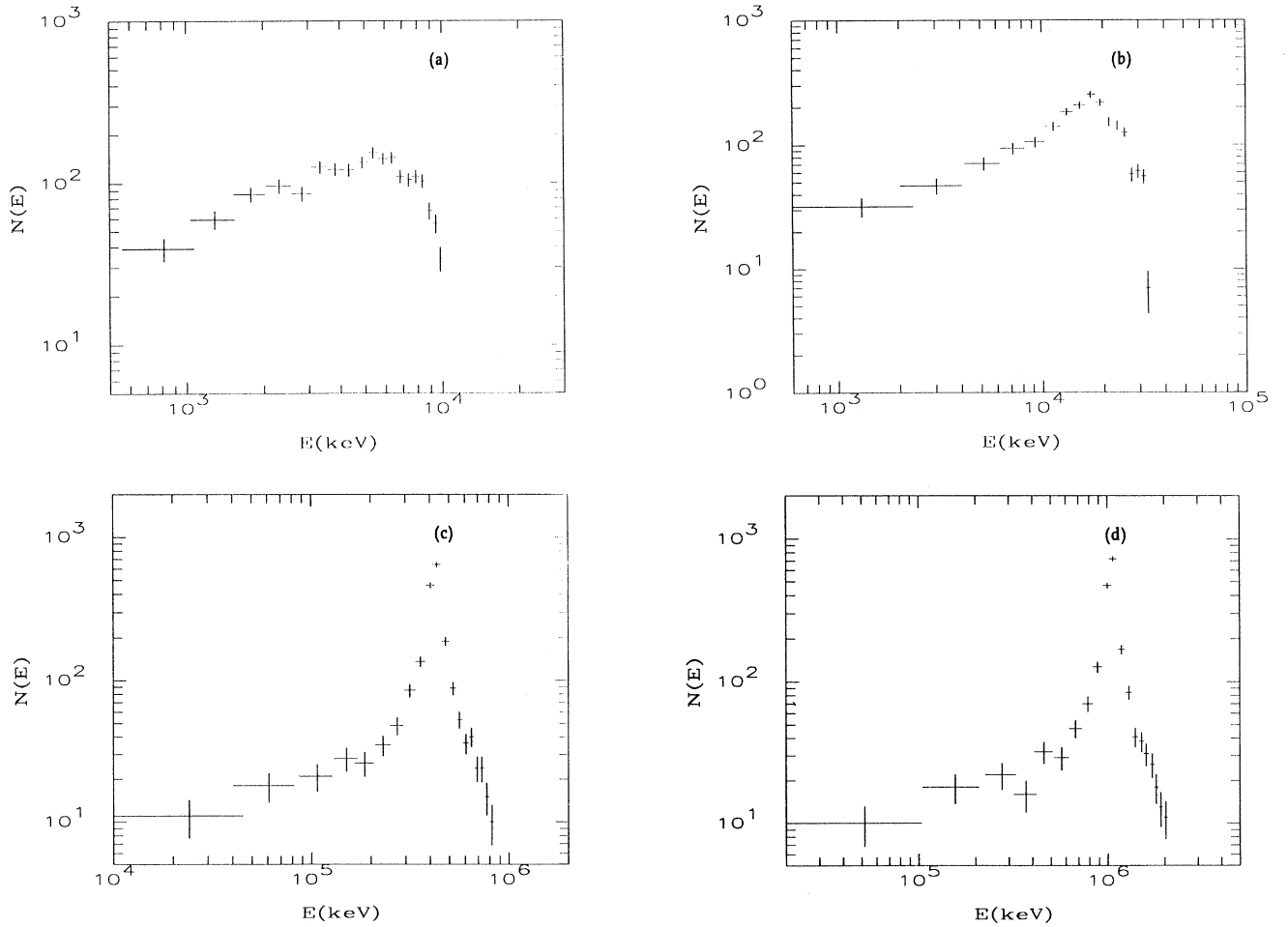

FIG. 5. Penrose pair production ($\gamma\gamma \to e^-e^+$): (a) $E_{\gamma 1} = 0.0035$ MeV (infalling) and $E_{\gamma 2} = 10.75$ MeV (target); No. 5 of Tables III and IV. (b) $E_{\gamma 1} = 0.0035$ MeV and $E_{\gamma 2} = 34.0$ MeV; No. 8. (c) $E_{\gamma 1} = 0.03$ MeV and $E_{\gamma 2} = 854.1$ MeV; No. 15. (d) $E_{\gamma 1} = 0.03$ MeV and $E_{\gamma 2} = 2.146$ GeV; No. 18.

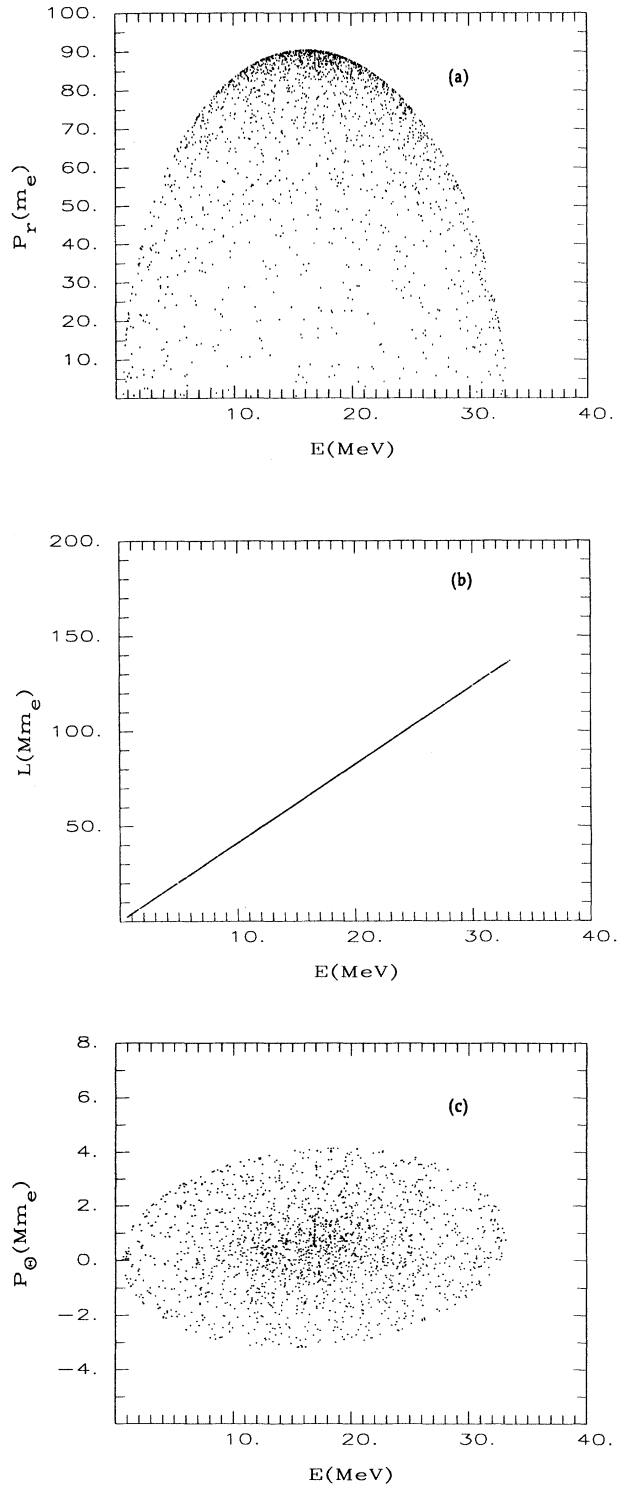

FIG. 6. Penrose pair production ($\gamma\gamma \rightarrow e^-e^+$): scatter plots showing space momenta of scattered escaping pairs (each point or mark represents a scattering event). For the infalling photons, $E_{\gamma 1} = 3.5$ keV, and the target orbiting photon, $\sqrt{Q_{\gamma 2}} = 0.987 M m_e$, with corresponding energy $E_{\gamma 2} = 34.0$ MeV. (a) Radial momentum components. (b) Azimuthal angle momentum components. (c) Polar angle momentum components ($\equiv \sqrt{Q_\mp}$). Same as Fig. 5(b) and No. 8 of Tables III and IV.

TABLE IV. The $\gamma\gamma \rightarrow e^-e^+$ processes: efficiencies.

Case no.	$\epsilon^W_{\rm BLF}$ [a]	ϵ^W [b]	$\epsilon^{\rm abs}$ [c]
1	311	47.2	0.32
2	37	41.0	0.33
3	0.41	29.1	0.09
4	0.02	28.8	0.02
5	145×10^1	48.8	0.47
6	154	45.3	0.43
7	0.11	20.4	0.05
8	478×10^1	49.3	0.49
9	10.2	33.1	0.29
10	290×10^2	49.5	0.49
11	42.2	40.3	0.39
12	472×10^2	49.5	0.49
13	562×10^1	49.3	0.50
14	111×10^3	49.5	0.46
15	140×10^2	49.5	0.49
16	404	47.5	0.47
17	253×10^3	49.5	0.41
18	348×10^2	49.5	0.49
19	50.7	41.8	0.39

[a] $\left[\frac{\text{total outgoing } e^-e^+ \text{ energy}}{\text{total incoming photon energy}(\gamma 1)}\right]$ as measured by a BLF observer.
[b] $\left(\frac{\text{W efficiency in the BLF}}{\text{W efficiency in the LNRF}}\right)$.
[c] $\left[\frac{\text{total outgoing } e^-e^+ \text{ energy}}{\text{total input energy}(\gamma 1+\gamma 2)}\right]$.

$E_{\gamma 2}$ (the orbiting photon), there is no noticeable change in the emitted spectra from that of the monochromatic infalling photons; and at lower energies for $E_{\gamma 2}$, there is very little change in the spectra (cf. No. 6 to 19 of Table III).

2. *A typical scattering event* ($\gamma\gamma \rightarrow e^-e^+$)

As it was done above for the other scattering processes, we will follow one $\gamma\gamma \rightarrow e^-e^+$ scattering event. The infalling photon has energy $E_{\gamma 1} = 3.5$ keV; the target photon of the photon orbit has energy $E_{\gamma 2} = 34.0$ MeV (A20), defined by the Q value of the orbit, $\sqrt{Q_{\gamma 2}} \equiv (P_{\gamma 2})_\Theta = 0.987 M m_e$ [see Fig. 1(a)]. In the LF these energies become $\varepsilon_{\gamma 1} = 182.9$ keV [Eq. (3.99)] and $\varepsilon_{\gamma 2} = 35.87$ MeV [Eq. (3.100)], respectively. The pair production process is done in the center-of-momentum frame (c.m. frame). The Monte Carlo method is applied to the cross section [Eq. (3.112)] and the scattering angles of the pairs are determined [see Eqs. (3.105b), (3.105c), (3.117), and (3.122)]. Upon transforming back to the LF, the energies of the positron and the negatron are measured to be $\varepsilon_+ = 22.73$ MeV and $\varepsilon_- = 13.2$ MeV, respectively. The BLF observer measures these energies as $E_+ = 12.5$ MeV and $E_- = 12.39$ MeV, respectively. Notice that the sum of the pair energies in the LF, equals (approximately) the sum of the primary photon energies in the LF, as would

be expected, due to conservation of energy in this *pseudo* flat spacetime. In Fig. 6, momentum components of the escaping pairs, for the case under discussion, are presented; this particular scattering event is represented by a point on the scatter plots, and is a member of the pairs in the spectrum of Fig. 5(b). The space momentum components in Fig. 6 reveal the following features of this PPP. (1) Only positive radial e^-e^+ pairs escape; this can be expected, since the scattering takes place at the photon orbit, beyond the last orbit ($r_{\rm MB}$) possible for any material particle (Sec. III A 1); therefore, inward scattered pairs would fall directly into the KBH [cf. Fig. 6(a)]. (2) The azimuthal angular momenta and energies are linear, and similar to the PCS [cf. Figs. 6(b), 3(b), and 4(b)]. (3) The polar angular momenta have a nearly symmetrical distribution about the equatorial plane [cf. Fig. 6(c)]; note that this is found not to be the case in the scatterings by the higher energy targets, as will be discussed later.

In the above so-called quasi-Penrose process, one might ask the question, was energy extracted from the KBH, since the pairs can escape with only the energy of the incident photons: the answer is yes, because of the following explanation, which includes my reason for classifying this PPP as a quasi-Penrose process. Photons are blueshifted to higher energies as they become bound in unstable orbits at the photon orbit. This newly acquired energy is given to a photon by way of the gravitational potential well (or the curvature of spacetime), and by way of the frame dragging due to the KBH. Now, before going on, I must deviate briefly to explain how these photon orbits, illustrated in Fig. 1(a), may be populated: I am assuming that the criteria for a photon to become bounded, depends on its polar angular momentum (i.e., its Q value) and its blueshifted initial energy [and that this blueshifted energy corresponds to the energy given when this Q value is substituted into Eq. (A20)]; moreover, since in the equatorial plane at the photon orbit $E_{\gamma 2} = 0$ (or $E_{\gamma 2}/\mu_0 = \infty$), I am led to believe that the only photons that can possibly become bound to the photon orbit are the ones with $Q_{\gamma 2} > 0$, and that no bound orbits exist for $Q_{\gamma 2} = 0$ (orbits that would be confined to the equatorial plane). Instead of depending on "normal" accretion processes, populating the photon orbit will most likely depend on some prior Penrose scattering processes to create the seed photons for these $\gamma\gamma \to e^-e^+$ reactions, especially true for the bound photons that have large orbital energies with corresponding large Q values. Such a task can possibly be accomplished by the PCS photons; these photons can, under the right initial conditions, be made to have the appropriate energies and Q values needed, i.e., to populate the photon orbit. In addition, as has been suggested [18], the γ rays created in the $\pi^\circ \to \gamma\gamma$ decays (Sec. I B) can, also, populate the photon orbit, i.e., if the γ rays are created with the appropriate Q values; this is something worthwhile investigating. (Possible ways to populate the orbits of the target particles will be looked at further in the following section.) Now continuing, assuming prior processes have populated the photon orbit, when the low energy infalling photons and the blueshifted orbiting photons collide, producing e^-e^+ pairs, the electrons that are allowed to escape to infinity, escape with the blueshifted energy imparted to the orbiting photons by the KBH; thus, in part, the energies of the escaping electrons come from the KBH, illustrating that energy is extracted: for this reason, I have classified such PPP events as quasi-Penrose processes.

D. Conclusions of the results

I conclude this section with the following comments. Of all the scattering cases presented, it seems that the incoming photon energies that give the most favorable results are in the ranges of 30 keV to 150 keV for the Compton scattering processes, and 3.5 keV to 30 keV for the $\gamma\gamma \to e^-e^+$ processes, based on what has been said above concerning the efficiencies [Eqs. (2.28b), (2.30), and (2.31)]: Recall that, indeed it is important to have a large factor by which the total input energy is increased ($\epsilon^W_{\rm BLF} \equiv$ "Penrose boost"); however, it is equally important to have a large as possible absolute efficiency $\epsilon^{\rm abs}$, which gives the amount of the total input energy (of the test particles participating in the scattering events) that can be effectively radiated away. To add to the importance of $\epsilon^{\rm abs}$, this efficiency is largest for the PCS cases when classical Penrose energy is extracted (cf. $\epsilon^{\rm PS}_{\rm peak}$ and $\epsilon^{\rm PS}_{\rm max}$ of Table II). The above incoming photon energy ranges are consistent with the thin disk/ion corona accretion models (Sec. I B). Note that the most favorable results are defined as the ones with absolute efficiencies $\epsilon^{\rm abs} > 0.42$, where this lowest limit expresses the value of the gravitational binding energy of a unit mass of gas when it reaches the inner edge of an accretion disk about a maximum rotating ($a = M$) KBH: the gravitational binding energy equals the total energy radiated by a unit mass of gas during its passage inward through the disk (neglecting radiation due to viscous stresses) [37].

Overall, for the scattering cases presented here for a $10^8 M_\odot$ KBH, the PCS photons can escape with energies in the range 15 keV$\lesssim E'_{\rm ph} \lesssim$ 12 MeV; and the PPP pairs ($\gamma\gamma \to e^-e^+$) can escape with energies in the range 2 MeV$\lesssim E_\mp \lesssim$ 2 GeV. Details of how well these cases correlate with existing accretion disk models will be discussed in the next section. Moreover, these Penrose processes can operator for any size mass rotating black hole. However, the emitted spectra will depend on how well the orbits of the target particles are populated by prior Penrose processes and normal accretion disk processes.

V. DISCUSSION

A. Summary

In this paper, I have presented Monte Carlo computer simulations of Compton scattering and e^-e^+ pair production processes ($\gamma p \to e^-e^+p$ and $\gamma\gamma \to e^-e^+$) in the ergosphere of a KBH. Particles, compatible with a thin disk/ion corona accretion surrounding the black hole, fall into the ergosphere and scatter off target particles that

are in bound orbits. These orbits consist of equatorial [$Q = 0$; see Eq. (2.6)] and nonequatorial ($Q > 0$) orbits. In this paper, the equations that govern the orbital trajectory of a particle about a KBH are solved to determine the conserved energy and angular momentum of material and massless particles that have orbits not confined to the equatorial plane (i.e., nonequatorial orbits; see Appendix A). The escape conditions to determine whether or not a particle escapes from the potential well of the KBH are applied to the scattered particles. The Penrose mechanism allows rotational energy of the KBH to be extracted by scattered particles escaping from the ergosphere to large distances from the black hole. The results of these model calculations, as we shall see in this section show that the Penrose mechanism is capable of producing the astronomically observed high energy particles emitted by quasars and other AGN. This mechanism, as applied in the models of this paper, can extract hard x-ray and γ-ray photons, from the inverse Compton scatterings of initially low energy UV and soft x-ray photons by target orbiting electrons inside the ergosphere. These model calculations also allow relativistic e^-e^+ pairs to escape after being produced by infalling low energy photons, interacting with target photons in bound orbits inside the ergosphere, at the photon orbit. This process may be the origin of the copious relativistic electrons inferred from observations to emerge from the cores of AGN.

B. Observations and disk model correlations

1. Inverse Compton scattering

Putting these PCS results into an astrophysical context, this process may play an important role in the upgrading of UV photons $\sim$ 5 eV, say from a classical thin disk, to x-ray photons $\sim$ 15–218 keV; and in upgrading soft x-ray and hard x-ray photons $\sim$ 0.511–150 keV, say from the thin disk/ion corona accretion (Sec. I B), to hard x-ray and γ-ray photons $\sim$ 53 keV–12 MeV: contributing to the high energy observed spectra of AGN. In addition, because most of the escaping γ rays have negative radial momenta and nonzero polar coordinate angular momenta [see Figs. 3(a), 3(c), 4(a), and 4(c)], these γ rays could possibly aid (along with magnetic fields and relativistic electrons) in the formation of the observed astrophysical jets commonly seen in AGN. Depicted in Fig. 7 are polar

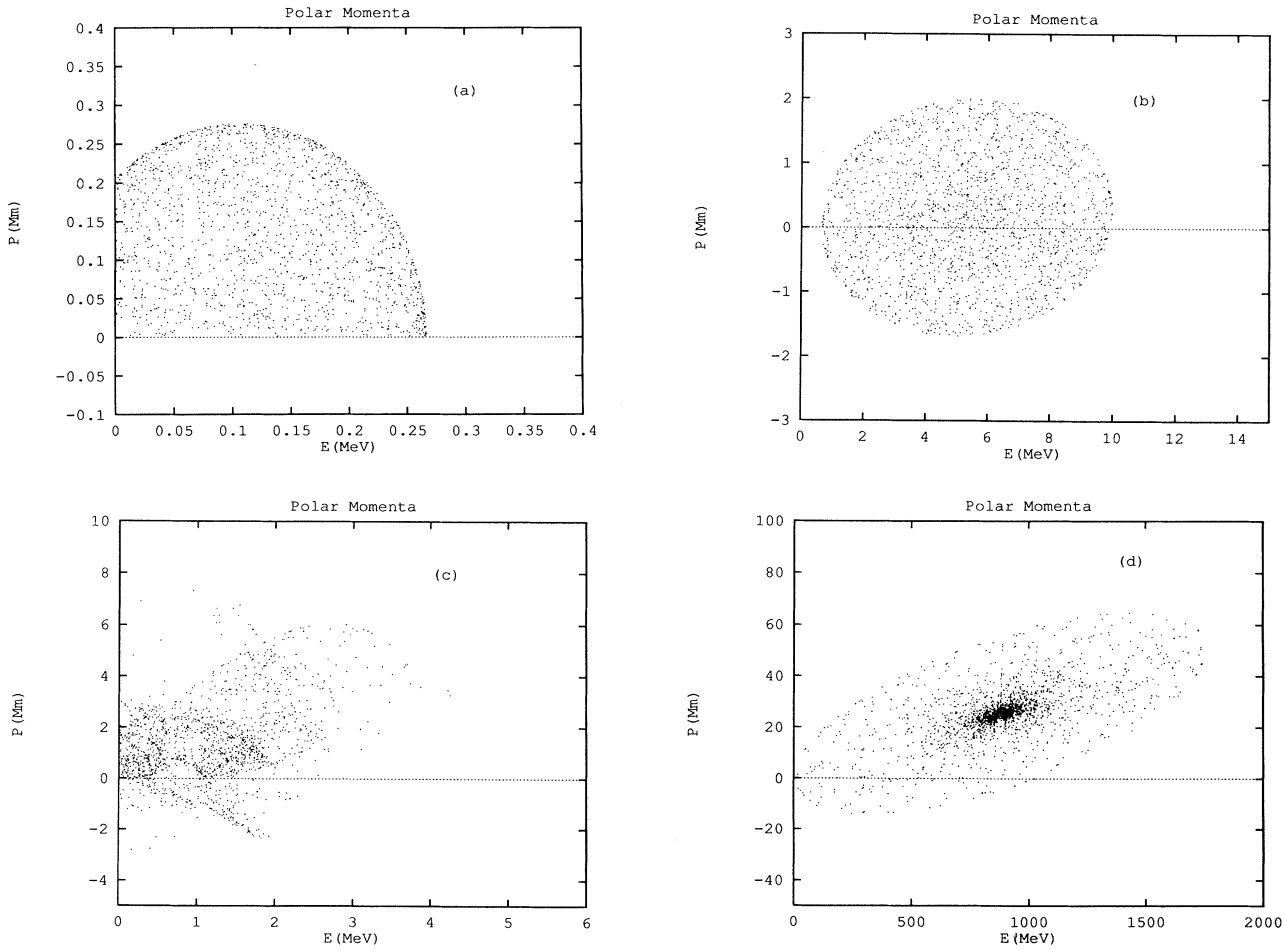

FIG. 7. Polar coordinate momentum $P_\Theta (\equiv \sqrt{Q})$ scatter plots for escaping particles. (a) PCS: No. 2 of Tables I and II; (b) PPP: No. 5 of Tables III and IV; (c) PCS: No. 19 of Tables I and II; (d) PPP: No. 17 of Tables III and IV.

coordinate momentum components for various Penrose scattering cases. Compare Figs. 3(c), 4(c), 7(a), and 7(c), which are for PCS; notice the asymmetry in the polar directions: the one-sided distribution favors the positive $\hat{\mathbf{e}}_\Theta$ direction. This feature could be extremely important in jet formation. Moreover, concerning the observations of these PCS photons, hard x-ray and γ-ray AGN observations have detected energies consistent with the range predicted by this model; details are addressed in another paper [38].

2. γ-ray–proton pair production

Because of the high energy e^-e^+ pairs predicted to be produced in this PPP process, this process could possibly be a somewhat fruitful way of extracting relativistic e^-e^+ pairs from the KBH, if one would, perhaps, relax the assumption that no recoil energy is given to the proton. This assumption is used in the integration of the cross section [Eq. (3.60)]. Relaxing this assumption has yet to be done, but would be one direction in which this research could be extended. In addition, since high energy initial photons are required by this $\gamma p \rightarrow e^-e^+p$ process, they would have to infall from an azimuthal direction [e.g., spiral: $L \neq 0$, in Eqs. (2.8c) and (2.8d)], so as not to have extremely large negative radial momentum components, which prevented, in these scattering cases, the pairs from escaping.

3. γ-ray–γ-ray pair production

In an astrophysical context, the results of this PPP process clearly show that this is an important way, if not the dominant way, to extract the relativistic e^-e^+ pairs—contributing to the observed synchrotron radiation of AGN, and the formation of jets. In essence, a possible picture of what an observer at infinity (the BLF) observes is the following: low energy unbound infalling photons, with energies as low as 3.5 keV (soft x rays), pair producing relativistic electrons at the photon orbit, of which about 50% of these relativistic electrons are allowed to escape from the potential well of the KBH, with energies as high as $\sim$ 2 GeV. These copiously produced relativistic escaping electrons can participate in astrophysical processes inherent to observations of AGN, such as, the production of the synchrotron radiation and the formation of jets. It is important to note here that if this $\gamma\gamma \rightarrow e^-e^+$ process had not occurred, photons in the photon orbit would, most likely, not have had any other way of escaping, and the energy released in this PPP process would have been forever trapped by the KBH. However, I cannot rule out the possibility of pair production between the photons in the photon orbit, nor the possibility that the photons in the unstable photon orbit can be made, if perturbed slightly, to spiral inward or escape outward.

4. Penrose processes and the classical thin disk

First note that, in these PCS and PPP ($\gamma\gamma \rightarrow e^-e^+$) processes, the low energies used for the infalling photons are consistent with the surface temperature ($T_s \simeq 5.3\times10^6$ K-4×10^7 K, at $r \approx 1.43M$, for $M = 10^8 M_\odot$) of the classical thin disk accretion model about a KBH [39]. Now, the scenario for a $10^8 M_\odot$ KBH, surrounded by a classical thin disk (i.e., before the Lightman instability sets in, as discussed in Sec. I B), is the following. About 75% of the initially infalling soft x rays ($\sim$ 3.5 keV), that have undergone PCS by equatorial orbiting target electrons, can escape with boosted energies as high as hard x rays ($\sim$ 0.26 MeV), while the others either fall into the KBH, or become bound at the photon orbit—acquiring blueshifted energies as high as $\sim$ 13 MeV (cf. No. 2 of Table I; recall that the blueshift parameter [of Eq. (2.8d)] is $\sim$ 50 at the photon orbit). The scatter plot of Fig. 7(a) illustrates that indeed such PCS photons can acquire the necessary Q values to populate the photon orbit by the criteria discussed in Sec. IV C 2 [i.e., the energies and Q values must match those of the photon orbit; cf. Fig. 1(a)]. Subsequently, these blueshifted photons, now assuming to have populated the photon orbit, can undergo PPP ($\gamma\gamma \rightarrow e^-e^+$) processes with infalling soft x rays, producing e^-e^+ pairs with energies as high as $\sim$ 12 MeV [cf. Fig. 5(a) and No. 5 of Table III]. About half of the produced pairs escape: these pairs can subsequently radiate synchrotron radiation in the presence of a magnetic field (as discussed in the following section). Thus, I conclude, that, due to PCS and PPP ($\gamma\gamma \rightarrow e^-e^+$) processes, in a classical thin disk, the highest particle energies attainable for the PCS photons are $\sim$ 260 keV; and for the relativistic PPP electrons, the highest energies attainable are $\sim$ 12 MeV. Yet, without these Penrose processes, as can be seen above from the surface temperature T_s, the highest energy radiated by a classical thin disk surrounding a supermassive KBH is $\sim$ 3.5 keV, and, of course, no pair production.

5. Penrose processes and the thin disk/ion corona

Since the disk can exist between two phases (thin disk/ion corona; see Sec. I B), the occurrence of the Lightman instability can act to enhance the Penrose process, being responsible for the observed variabilities, and particle energies up to $\sim$ GeV, as we shall see in the following scenario, for a $10^8 M_\odot$ KBH, surrounded by a thin disk/ion corona. In this scenario, x rays $\sim$ 0.03–0.15 MeV, after undergoing PCS by equatorial orbiting target electrons, can escape with boosted energies ranging from $\sim$ 0.7 MeV up to $\sim$ 4 MeV (see Nos. 3–5 and 19 of Table I). Just as in the classical thin disk, about 75% of the PCS photons escape, while the others either fall into the KBH, or become bound at the photon orbit—acquiring blueshifted energies, however, in these cases, ranging from $\sim$ 35 MeV to as high as $\sim$ 200 MeV. The scatter plots of Figs. 3(c) and 7(c) illustrate that indeed these PCS photons can acquire the necessary Q values to

populate the photon orbit in the above blueshifted energy range [cf. Fig. 1(a)]. Subsequently, the blueshifted photons, now assuming to have populated the photon orbit, can undergo the PPP ($\gamma\gamma \rightarrow e^-e^+$) processes with infalling soft x rays, producing e^-e^+ pairs that can escape with energies as high as $\sim$ 200 MeV (cf. Nos. 8 and 10 of Table III). Moreover, such escaping relativistic e^-e^+ pairs, in the presence a large strength magnetic field, as we shall see below, can produce synchrotron radiation spectra, with energies ranging up to $\sim$ GeV, consistent with the observed spectra of AGN.

Now we assume that the photon orbit can be populated by γ rays from the pion decays ($\pi^0 \rightarrow \gamma\gamma$), occurring in Eilek's [12] thin disk/ion corona model in the Kerr metric (see Secs. IB and IC). To test the validity of this assumption, these pion decays, as well as the resulting pairs produced by these newly created γ rays, should be treated also as Penrose processes, since the inner region of the accretion disk extends well inside the ergosphere (to $\sim r_{\rm MS} = 1.2M$). There is a strong possibility that some of the resultant scattered Penrose particles will acquire the necessary Q values to populate the orbits, since this was found to be the case in the PCS events. Such an investigation is under way by the author; the results will be reported elsewhere. Nevertheless, these γ rays are created with energies narrowly peaked around $E_\gamma \simeq 75$ MeV. Such γ rays, say, of initial energies $E_\gamma \sim 50$ MeV can be blueshifted to energies $\sim$ 2 GeV, as they become bound at the photon orbit. Subsequently, infalling soft x rays from the disk can undergo PPP ($\gamma\gamma \rightarrow e^-e^+$) with these bound γ rays, producing e^-e^+ pairs that can escape with energies up to $\sim$ 2 GeV [cf. Fig. 5(d) and Nos. 17, 18 of Table III]. Again, magnetic fields can harden the observed energy spectra to energies $>$ 2 GeV: we next look at such secondary processes. But first, notice in Figs. 6(c), 7(b), and 7(d) the increase in the asymmetry of the pair distribution, as the orbital energy (or Q value) of the target photon increases: such one-sidedness could be, as in the PCS case, extremely important in jet formation.

Moreover, if we assume that pairs produced in the model of Ref. [12], mentioned above, with energies peaked around $E_\pm \simeq 35$ MeV, can populate the nonequatorial target electron orbits, at least in the range of $\sim$ 12 MeV: provided that these electrons are created with appropriate Q values [cf. Fig. 1(b)], then PCS, of infalling soft x rays and UV photons from the disk, allows most of the scattered photons to escape with boosted energies up to $\sim$ 12 MeV [cf. Nos. 7–12, 14, 15 of Table I and Figs. 2(b) and 4]. These PCS γ rays up to $\sim$ 12 MeV (or $\sim$ 35 MeV) could contribute somewhat to observed spectra in this energy range. The importance of these PCS γ rays is that they would acquire and escape with large polar coordinate momenta [cf. Fig. 4(c)]: thus supporting the jet formation process.

Yet, still before going on to discuss secondary processes, these energies of the escaping Penrose scattered particles are to be compared with maximum energies attainable for the popular "two-temperature" accretion disk models [40] (such as thin disk/ion corona): in these disk models, without Penrose processes occurring, the maximum particle energies attainable are $\sim$ 100 MeV [12]. However, when the Penrose processes, PCS and PPP ($\gamma\gamma \rightarrow e^-e^+$), are included, particles can escape with energies as high as $\sim$ 2 GeV.

Now proceeding with the discussion of secondary processes, it was mentioned above that the relativistic e^-e^+ pairs can give rise to observed synchrotron radiation of AGN. We can gain some insight into this claim and possibly find a way to test its validity by estimating the range of synchrotron frequencies generated by these PPP electrons, for various values of assumed magnetic field strengths, using

$$B \sim \frac{4\pi m_e c}{3e\gamma_e^2}\nu_{\rm syn} \tag{5.1a}$$

or

$$\nu_{\rm syn} \sim 4 \times 10^6 \gamma_e^2 B \tag{5.1b}$$

[41], where γ_e is the characteristic Lorentz factor of electrons radiating at synchrotron frequency $\nu_{\rm syn}$. For $B \sim 10^2$ gauss and scattered e^-e^+ pairs with mean energy $\sim$ 1 MeV, $\gamma_e \sim 2$, then $\nu_{\rm syn} \sim 10^9$ Hz (radio); and with the mean energy $\sim$ 200 MeV, $\gamma_e \sim 391$, then $\nu_{\rm syn} \sim 6 \times 10^{13}$ Hz (ir). On the other hand, for $B \sim 10^{12}$ gauss and scattered e^-e^+ pairs with mean energy $\sim$ 1 MeV, then $\nu_{\rm syn} \sim 10^{19}$ Hz (hard x rays); and with mean energy $\sim$ 200 MeV, then $\nu_{\rm syn} \sim 6 \times 10^{23}$ Hz (hard γ rays), corresponding to energies $\sim$ 3 GeV being radiated. Now the above synchrotron photons were radiated without including Eilek's γ rays to populate the photon orbits, serving as seeds particles, for these PPP processes. If, however, Eilek's particles are included, then from the PPP scattered pairs (of energies $\sim$ GeV), even higher synchrotron frequencies can be achieved, in some cases yielding synchrotron γ-ray energies as high as $\sim$ 270 GeV. Note that $B \sim 10^{2-5}$ gauss gives a typical range of values of the magnetic field strength assumed for the accretion disk of AGN [42–44]. However, the possibility of a higher field strength (say $\sim 10^{12}$ gauss), one associated with the black hole itself, should not be ruled out. I propose that such a field, like that of a Kerr-Newman black hole (with charge and rotation), could be important in the jets of AGN [45]. Thus, so we see, that, for appropriate ranges of an assumed magnetic field strength and the Lorentz factors given by the PPP electrons, using Eq. (5.1), synchrotron radiation can be radiated by the e^-e^+ pairs, from the radio region up to the hard γ-ray region of the electromagnetic spectrum. I mentioned this because it is a possibility that the observed x rays and γ rays of AGN may very well be synchrotron radiation, at least in part (the other part being predominantly due to PCS and secondary relativistic inverse Compton scattering by the escaping PPP relativistic e^-e^+ pairs, yielding γ-ray energies of the order of the pairs).

VI. CONCLUSION AND FURTHER INVESTIGATIONS

It has been shown through these Monte Carlo model calculations, in the ergosphere of a KBH, that (1) higher

energies are attainable than previously calculated [4,8,9] when PCS processes are present; (2) relativistic e^-e^+ pairs, agreeing with the observed spectra of AGN, can be produced at the photon orbit by PPP ($\gamma\gamma \rightarrow e^-e^+$), and that about 50% of these pairs can escape from the potential well (leading to synchrotron radiation); and (3) the momenta of the Penrose scattered particles naturally aid in the production of one-sided and two-sided polar jets. The occurrences of these Penrose processes do not depend on instabilities that may or may not be present in the accretion disk, but can operate in the rims of the classical thin disk accretion model surrounding a KBH [37]. Perhaps the instabilities that do occur in the disk should be attributed to the variabilities observed in AGN, the extremely high energy spectra, and responsible for the different species (or morphologies) of these celestial objects. In addition, I want to make it clear that the model presented in this paper does not rule out the physical processes existing in other prominent AGN models, particular relativistic beaming models [46], but only gives the possible role that can be played by the black hole, and thus, should be included as an important source of energy when modeling AGN.

Further investigations could include the PCS and PPP ($\gamma\gamma \rightarrow e^-e^+$) of nonradially infalling photons, i.e., photons that have azimuthal directions as well. The PPP ($\gamma p \rightarrow e^-e^+p$) should be investigated further, since the escaping pairs are predicted to emerge with energies $\sim$ GeV. However, the assumption that no recoil energy is given to the proton should probably not be used in integrating the cross section; and the infalling photons of this PPP process should have also azimuthal directions, instead of just radial directions (as were used in these present model calculations), so that the pairs may be allowed to escape. In addition, the interaction of the e^-e^+ pairs, produced in the PPP ($\gamma\gamma \rightarrow e^-e^+$) process, with the surrounding electromagnetic field, associated with the black hole and the plasma in an accretion disk, requires immediate investigation, as this may shed considerable light on the formation of the astrophysical jets of AGN [45].

Before closing, I want to mention that the observed energy spectra of AGN are very similar to the universal predicted photon spectrum, produced by these Penrose processes. In particular, the *Gamma Ray Observatory* (GRO), which observes in the range from 30 keV to 30 GeV, has measured energies up to $\sim$ 4 GeV for quasar 3C 279 [47], consistent with the spectra predicted by these Penrose processes. How well these Penrose spectra compare with AGN observations are addressed in another paper [38].

ACKNOWLEDGMENTS

I thank Dr. Jean Eilek, Dr. Richard Durisen, and Dr. Stuart Mufson for their astrophysical comments and suggestions. Also, I thank Dr. William Fowler and Dr. Roger Penrose for their encouragement. And finally, I thank Indiana University and University of Florida for their hospitality as this work was being completed. This work was supported in part by the National Research Council.

APPENDIX A: EQUATORIAL AND NONEQUATORIAL ORBITS

From the Kerr metric of Eq. (2.1), the Lagrangian (L_g) for geodesics [48],

$$L_g = \frac{1}{2} g_{\alpha\beta} \dot{x}^\alpha \dot{x}^\beta \ , \tag{A1}$$

can be found for a test particle in the field of a KBH, where $\dot{x}^\alpha \equiv dx^\alpha/d\lambda = P^\alpha$ (the contravariant four-momentum); λ is related to the proper time of the particle, τ ($\lambda = \tau/m_0$); and it is the affine parameter for massless particles, where $m_0 \equiv$rest mass=0. The scalar product of the four-momentum with itself gives the relation

$$P^\alpha P_\alpha = -m_0^2 = g_{\alpha\beta} P^\alpha P^\beta \tag{A2}$$

($c = 1$); then, from (A1),

$$L_g = -\frac{m_0^2}{2} \ . \tag{A3}$$

Using Eqs. (2.1)–(2.3), (2.6), (A1)–(A3), and the Euler-Lagrange equations of motion, the P_α's (the covariant four-momentum components) and the P^α's can be solved for, obtaining equations governing the orbital trajectory of a test particle in the field of a KBH:

$$\Sigma dr/d\lambda = \pm(V_r)^{1/2} \ , \tag{A4}$$

$$\Sigma d\Theta/d\lambda = \pm(V_\Theta)^{1/2} \ , \tag{A5}$$

$$\Sigma d\Phi/d\lambda = -(aE - L/\sin^2\Theta) + aT/\Delta \ , \tag{A6}$$

$$\Sigma dt/d\lambda = -a(aE\sin^2\Theta - L) + (r^2 + a^2)T/\Delta \ , \tag{A7}$$

where

$$T \equiv E(r^2 + a^2) - La \ , \tag{A8}$$

$$V_r \equiv T^2 - \Delta[m_0^2 r^2 + (L - aE)^2 + Q] \ , \tag{A9}$$

$$V_\Theta \equiv Q - \cos^2\Theta[a^2(m_0^2 - E^2) + L^2/\sin^2\Theta \tag{A10}$$

[21], in geometric units ($G = c = 1$). V_r and V_Θ are the *effective potentials* governing particle motions in r and Θ directions, respectively. For a circular orbit at some radius r, $dr/d\lambda$ must vanish both instantaneously and at all subsequent times (orbit at a perpetual turning point). Equation (A4) then gives the conditions for circular orbits:

$$V_r(r) = 0 \ , \quad V_r'(r) \equiv \frac{dV_r}{dr} = 0 \ . \tag{A11}$$

From Eq. (A9) and its derivative, I obtain the equations

$$V_r = [(r^2 + a^2)^2 - a^2\Delta]E^2 - 4MarLE - (\Delta - a^2)L^2 - \Delta Q - r^2\Delta\mu_0^2 = 0 \ , \tag{A12}$$

and

$$V_r' = 2(2r^3 + ra^2 + Ma^2)E^2 - 4MaLE + 2(M-r)L^2 + 2(M-r)Q + 2[\mu_0^2 r(Mr - r^2 - \Delta)] = 0 \ , \quad \text{(A13)}$$

where m_0 has been replaced with μ_0, the rest-mass-energy of a particle. The above equations can be solved simultaneously, yielding the conserved energy E and the conserved angular momentum L (as measured by an observer at infinity), for orbits of constant r not confined to the equatorial plane ($Q \neq 0$). If we define

$$\tilde{A} \equiv [(r^2 + a^2)^2 - a^2\Delta] \ , \quad \text{(A14)}$$
$$B \equiv 4Mar \ , \quad \text{(A15)}$$
$$C \equiv \Delta - a^2 \ , \quad \text{(A16)}$$
$$D \equiv (3r^4 - 4Mr^3 + a^2r^2)\mu_0 \ , \quad \text{(A17)}$$
$$F \equiv (r^2 - a^2)Q \ , \quad \text{(A18)}$$
$$G \equiv 3r^4 + a^2r^2 \ , \quad \text{(A19)}$$

then

$$E = \left(\frac{r^2L^2 + D + F}{G}\right)^{1/2} \equiv E^* \ , \quad \text{(A20)}$$

and

$$L = \left[\frac{-J - (J^2 - 4IK)^{1/2}}{2I}\right]^{1/2} \equiv L^* \ , \quad \text{(A21)}$$

where E^* and L^* are the conserved energy and azimuthal angular momentum of nonequatorial particle orbits (geodesics) in the curved spacetime of a KBH, and

$$I \equiv \frac{\tilde{A}^2 r^4}{G^2} - \frac{r^2}{G}(2\tilde{A}C + B^2) + C^2 \ , \quad \text{(A22)}$$

$$J \equiv \frac{(D+F)}{G}\left[\frac{2\tilde{A}^2r^2}{G} - 2\tilde{A}C - B^2\right] + 2\Delta(r^2\mu_0^2 + Q)\left[C - \frac{\tilde{A}r^2}{G}\right] \ , \quad \text{(A23)}$$

$$K \equiv \frac{\tilde{A}^2}{G^2}(D+F)^2 - \frac{2\tilde{A}\Delta}{G}(r^2\mu_0^2 + Q)(D+F) + \Delta^2(r^2\mu_0^2 + Q)^2 \ ; \quad \text{(A24)}$$

see Eqs. (A14)–(A19). Note that when $Q = 0$, Eqs. (A20) and (A21) reduce to the forms of (2.16) and (2.17), respectively. The energy expressed by Eq. (A20) versus $\sqrt{Q}(\equiv P_\Theta)$ is plotted in Fig. 1(a) for the photon orbit, and it is plotted in Fig. 1(b) for the electron orbits at $r_{\rm MB}$ and $r_{\rm MS}$.

APPENDIX B: THE GENERAL LORENTZ TRANSFORMATIONS

The Lorentz transformation for any four-vector $A_\lambda = (\vec{A}, A_4)$ is

$$A_\mu' = \sum_{\nu=1}^{4} L_{\mu\nu}A_\nu \ , \quad \text{(B1)}$$

where the primes represent the inertial coordinate system moving with uniform velocity $\vec{v}$ relative to the unprimed coordinate system. The inverse to this Lorentz transformation is

$$A_\mu = \sum_{\nu=1}^{4}(L_{\mu\nu})^{-1}A_\nu' = \sum_{\nu=1}^{4}(L_{\mu\nu})^t A_\nu' \ , \quad \text{(B2)}$$

where the last equality arises from a property of an orthogonal matrix $L_{\mu\nu}$; that is, the inverse $(L_{\mu\nu})^{-1}$ of $L_{\mu\nu}$ is equal to the transpose $(L_{\mu\nu})^t$ of $L_{\mu\nu}$. Upon evaluation of Eq. (B1), using the general form of the $L_{\mu\nu}$ matrix [49], the following Lorentz transformations are obtained for the vector A_μ' relative to the moving system in terms of the vector A_μ measured in the rest system:

$$A_1' = \left(1 + \beta_1^2\frac{\gamma^2}{\gamma+1}\right)A_1 + \beta_1\beta_2\frac{\gamma^2}{\gamma+1}A_2 + \beta_1\beta_3\frac{\gamma^2}{\gamma+1}A_3 - i\beta_1\gamma A_4 \ , \quad \text{(B3a)}$$

$$A_2' = \beta_2\beta_1\frac{\gamma^2}{\gamma+1}A_1 + \left(1 + \beta_2^2\frac{\gamma^2}{\gamma+1}\right)A_2 + \beta_2\beta_3\frac{\gamma^2}{\gamma+1}A_3 - i\beta_2\gamma A_4 \ , \quad \text{(B3b)}$$

$$A_3' = \beta_3\beta_1\frac{\gamma^2}{\gamma+1}A_1 + \beta_3\beta_2\frac{\gamma^2}{\gamma+1}A_2 + \left(1 + \beta_3^2\frac{\gamma^2}{\gamma+1}\right)A_3 - i\beta_3\gamma A_4 \ , \quad \text{(B3c)}$$

$$A_4' = i\beta_1\gamma A_1 + i\beta_2\gamma A_2 + i\beta_3\gamma A_3 + \gamma A_4 \ , \quad \text{(B3d)}$$

where β_1, β_2, and β_3 are the space velocity components. Similarly, we evaluate Eq. (B2) to get the inverse Lorentz transformation, that is, the vector in the coordinate system at rest in terms of the vector moving with relative velocity $\vec{v}$. It is found that

$$A_1 = \left(1 + \beta_1^2\frac{\gamma^2}{\gamma+1}\right)A_1' + \beta_1\beta_2\frac{\gamma^2}{\gamma+1}A_2' + \beta_1\beta_3\frac{\gamma^2}{\gamma+1}A_3' + i\beta_1\gamma A_4' \ , \quad \text{(B4a)}$$

$$A_2 = \beta_2\beta_1\frac{\gamma^2}{\gamma+1}A_1' + \left(1 + \beta_2^2\frac{\gamma^2}{\gamma+1}\right)A_2' + \beta_2\beta_3\frac{\gamma^2}{\gamma+1}A_3' + i\beta_2\gamma A_4' \ , \quad \text{(B4b)}$$

$$A_3 = \beta_3\beta_1\frac{\gamma^2}{\gamma+1}A_1' + \beta_3\beta_2\frac{\gamma^2}{\gamma+1}A_2' + \left(1 + \beta_3^2\frac{\gamma^2}{\gamma+1}\right)A_3' + i\beta_3\gamma A_4' \ , \quad \text{(B4c)}$$

$$A_4 = -i\beta_1\gamma A_1' - i\beta_2\gamma A_2' - i\beta_3\gamma A_3' + \gamma A_4' \ . \quad \text{(B4d)}$$

Now we write these transformations in the coordinate directions of the orthonormal tetrad used to derive the vector of Eq. (3.3). The corresponding space unit vectors at an instant of time are

$$\hat{\mathbf{e}}_x = \hat{\mathbf{e}}_1 \equiv \hat{\mathbf{e}}_r \ ,$$
$$\hat{\mathbf{e}}_y = \hat{\mathbf{e}}_2 \equiv \hat{\mathbf{e}}_\Theta \ , \quad \text{(B5)}$$
$$\hat{\mathbf{e}}_z = \hat{\mathbf{e}}_3 \equiv \hat{\mathbf{e}}_\Phi \ .$$

Thus, the following substitutions are to be made in Eqs. (B3) and (B4) to derive the Lorentz transformation used in the text:

$$\begin{aligned} &A_1 \equiv p_r \ , \quad A_1' \equiv p_r' \ , \\ &A_2 \equiv p_\Theta \ , \quad A_2' \equiv p_\Theta' \ , \\ &A_3 \equiv p_\Phi \ , \quad A_3' \equiv p_\Phi' \ , \\ &A_4 = i\frac{\varepsilon}{c} \ , \quad A_4' \equiv i\frac{\varepsilon'}{c} \ , \\ &\beta_1 \equiv \beta_r \ , \quad \beta_2 \equiv \beta_\Theta \ , \quad \beta_3 \equiv \beta_\Phi \ . \end{aligned} \tag{B6}$$

APPENDIX C: UNKNOWN ANGLES IN THE $\gamma p \to e^- e^+ p$ PROCESS

In this appendix, the equations of Eq. (3.79) are solved simultaneously for the unknown angles of Eq. (3.80a), in terms of the known angles of Eq. (3.80b).

From Eqs. (3.79c) to (3.79e) we find that

$$\theta_{\gamma p}^R = \theta_\gamma^R \ , \tag{C1}$$

$$\theta_{p_+}^R = \theta_{e^+}^R \ , \tag{C2}$$

$$\theta_{p_-}^R = \theta_{e^-}^R \ , \tag{C3}$$

where θ_γ^R is given by Eq. (3.81). Next substitute Eqs. (C1) and (C2) into (3.79g) to get $\theta_{e^+}^R$, and similarly, substitute Eqs. (C1) and (C3) into Eq. (3.79h) to get $\theta_{e^-}^R$. Thus we find that

$$\theta_{e^+}^R = \arccos[\cos\theta_\gamma^R \cos\theta_+^R + \sin\theta_\gamma^R \sin\theta_+^R \cos(\phi_{\gamma p}^R - \phi_1^R)] \ , \tag{C4}$$

$$\theta_{e^-}^R = \arccos[\cos\theta_\gamma^R \cos\theta_-^R + \sin\theta_\gamma^R \sin\theta_-^R \cos(\phi_{\gamma p}^R - \phi_2^R)] \ , \tag{C5}$$

where $\phi_{\gamma p}^R = 0$ (see text). Now solve Eq. (3.79f) for ϕ_2^R of Eq. (C5), yielding

$$\phi_2^R = \phi_1^R - \arccos\left(\frac{\cos\theta_*^R - \cos\theta_+^R \cos\theta_-^R}{\sin\theta_+^R \sin\theta_-^R}\right) \ . \tag{C6}$$

Finally, solve Eq. (3.79a) for $\phi_{e^+}^R$ and Eq. (3.79b) for $\phi_{e^-}^R$, thus Eq. (3.79a) gives

$$\phi_{e^+}^R = \phi_\gamma^R - \arccos\left(\frac{\cos\theta_+^R - \cos\theta_\gamma^R \cos\theta_{e^+}^R}{\sin\theta_\gamma^R \sin\theta_{e^+}^R}\right) \tag{C7}$$

and Eq. (3.79b) gives

$$\phi_{e^-}^R = \phi_\gamma^R - \arccos\left(\frac{\cos\theta_-^R - \cos\theta_\gamma^R \cos\theta_{e^-}^R}{\sin\theta_\gamma^R \sin\theta_{e^-}^R}\right) \ , \tag{C8}$$

where ϕ_γ^R is given by Eq. (3.81). Equations (C1) to (C8) completely solve Eq. (3.79) for the unknown angles Eq. (3.80a); Eqs. (C4), (C5), (C7), and (C8) give the polar and azimuthal angles of the scattered $e^- e^+$ pairs.

APPENDIX D: UNKNOWN ANGLES IN THE $\gamma\gamma \to e^- e^+$ PROCESS

In this appendix, the unknown space momentum angles of Eq. (3.119) for the $e^- e^+$ pairs are solved for in terms of the scattering angles θ_+^c, θ_-^c, and ϕ_+^c [see Eq. (3.105)]. Substitute Eq. (3.119a) into (3.119f) and solve for $\theta_{e^+}^c$ to get

$$\theta_{e^+}^c = \arcsin\left(\frac{-\cos\theta_+^c}{\cos\phi_{e^+}^c}\right) \ . \tag{D1}$$

Next, we solve for $\phi_{e^+}^c$. Upon substituting Eq. (D1) into (3.119d), applying some algebraic manipulation, and using the trigonometric identity $\sec^2\phi_{e^+}^c = 1 + \tan^2\phi_{e^+}^c$, I obtain a quadratic equation in $\tan\phi_{e^+}$, which has the solution

$$\phi_{e^+}^c = \arctan\left[\frac{-D_2 \pm (D_2^2 - 4D_1D_3)^{1/2}}{2D_1}\right] \ , \tag{D2a}$$

where

$$D_1 \equiv \cos^2\theta_+^c \sin^2\theta_+^c \ , \tag{D2b}$$

$$D_2 \equiv 2\cos\theta_+^c \sin\theta_+^c \sin\phi_+^c (1 - \cos^2\theta_+^c) \ , \tag{D2c}$$

$$\begin{aligned} D_3 \equiv\ & 1 + \cos^2\theta_+^c(\cos^2\theta_+^c - 2) \\ & + \sin^2\theta_+^c \cos^2\phi_+^c (\cos^2\theta_+^c - 1) \ . \end{aligned} \tag{D2d}$$

Equations (D1) and (D2) completely solve Eq. (3.119) for the unknown angles.

[1] B. Carter, in *Black Holes*, edited by C. DeWitt and B. S. DeWitt (Gordon and Breach, New York, 1973).
[2] C. W. Misner, K. S. Thorne, and J. A. Wheeler, *Gravitation* (Freeman, San Francisco, 1973).
[3] R. Penrose, Riv. Nuovo Cimento: Numero Speciale **1**, 252 (1969).
[4] T. Piran and J. Shaham, Phys. Rev. D **16**, 1615 (1977).
[5] D. Christodoulou, Phys. Rev. Lett. **25**, 1596 (1970).
[6] T. Piran, J. Shaham, and J. Katz, Astrophys. J. Lett. **196**, L107 (1975).
[7] K. S. Thorne, Astrophys. J. **191**, 507 (1974).
[8] T. Piran and J. Shaham, Astrophys. J. **214**, 268 (1977).
[9] T. Piran and J. Shaham, in *Physics and Astrophysics of Neutron Stars and Black Holes*, Proceedings of the

International School of Physics "Enrico Fermi," Varenna, Italy, 1975, edited by R. Giacconi and R. Ruffini (North-Holland, Amsterdam, 1977).
[10] M. J. Rees, Annu. Rev. Astron. Astrophys. **22**, 471 (1984).
[11] A. P. Lightman, Astrophys. J. **194**, 419 (1974); **194**, 429 (1974).
[12] J. A. Eilek, Astrophys. J. **236**, 664 (1980).
[13] J. A. Eilek and M. Kafatos, Astrophys. J. **271**, 804 (1983).
[14] D. Leiter and M. Kafatos, Astrophys. J. **226**, 32 (1978).
[15] M. Kafatos and D. Leiter, Astrophys. J. **229**, 46 (1979).
[16] W. Heitler, *The Quantum Theory of Radiation* (Oxford, London, 1954).
[17] R. K. Lang, *Astrophysical Formulae* (Springer-Verlag, Berlin, 1980).
[18] J. A. Eilek (private communication).
[19] R. P. Kerr, Phys. Rev. Lett. **11**, 237 (1963).
[20] R. H. Boyer and R. W. Lindquist, J. Math. Phys. **8**, 265 (1967).
[21] J. M. Bardeen, W. H. Press, and S. A. Teukolsky, Astrophys. J. **178**, 347 (1972).
[22] B. Carter, Phys. Rev. **174**, 1559 (1968).
[23] D. C. Wilkins, Phys. Rev. D **5**, 814 (1972).
[24] J. M. Bardeen, in *Black Holes*, edited by C. DeWitt and B. S. DeWitt (Gordon and Breach, New York, 1973).
[25] R. K. Williams, Ph.D. thesis, Indiana University, 1991.
[26] R. K. Wangsness, *Electromagnetic Fields* (Wiley, New York, 1979), p. 36.
[27] T. Piran and A. Kovetz, Lett. Nuovo Cimento **12**, 39 (1975).
[28] M. Demiańsk, *Relativistic Astrophysics* (PWN-Polish, Warszawa, 1985).
[29] C. Møller, *The Theory of Relativity* (Oxford University, Delhi, 1972).
[30] J. M. Jauch and F. Rohlich, *The Theory of Photons and Electrons* (Addison-Wesley, Cambridge, 1955).
[31] H. Bethe and W. Heitler, Proc. R. Soc. London **A146**, 83 (1934).
[32] M. Stearns, Phys. Rev. **76**, 826 (1949).
[33] B. Rossi and K. Greisen, Rev. Mod. Phys. **13**, 240 (1941).
[34] P. V. C. Hough, Phys. Rev. **74**, 80 (1948).
[35] E. J. Konopinski, *Electromagnetic Fields and Relativistic Particles* (McGraw-Hill, New York, 1981).
[36] J. A. Eilek, L. C. Caroff, and P. D. Noerdlinger, report, 1991 (unpublished).
[37] I. D. Novikov and K. S. Thorne, in *Black Holes*, edited by C. DeWitt and B. S. DeWitt (Gordon and Breach, New York, 1973).
[38] R. K. Williams, report, 1995 (unpublished).
[39] D. M. Eardley and A. P. Lightman, Astrophys. J. **200**, 187 (1975).
[40] S. L. Shapiro, A. P. Lightman, and D. M. Eardley, Astrophys. J. **204**, 187 (1976); A. P. Lightman and D. M. Eardley, Astrophys. J. Lett. **187**, L1 (1974).
[41] G. R. Burbidge, T. W. Jones, and S. L. O'Dell, Astrophys. J. **193**, 43 (1974).
[42] R. V. E. Lovelace, Nature (London) **262**, 649 (1976).
[43] I. D. Novikov and B. E. Stern, in *Structure and Evolution of Active Galactic Nuclei*, Proceedings of the International Meeting, Trieste, Italy, 1985, edited by G. Giuricin, R. Mardirossian, M. Mezzetti, and M. Ramella (Gordon and Breach, New York, 1986).
[44] J. A. Eilek, in *Supermassive Black Holes*, Proceedings of the Third George Mason Astrophysics Workshop, Fairfax, Virginia, 1986, edited by M. Kafatos (Cambridge University Press, New York, 1988).
[45] R. K. Williams (in preparation).
[46] R. D. Blandford, C. F. McKee, and M. J. Rees, Nature (London) **267**, 211 (1977); R. D. Blandford and A. Königl, Astrophys. J. **232**, 34 (1979); C. D. Dermer, R. Schlickeiser, and A. Mastichiadis, Astron. Astrophys. **256**, L27 (1992).
[47] R. C. Hartman *et al.*, Astrophys. J. Lett. **385**, L4 (1992).
[48] S. L. Shapiro and S. A. Teukolsky, *Black Holes, White Dwarfs, and Neutron Stars* (Wiley, New York, 1983).
[49] H. Muirhead, *The Special Theory of Relativity* (MacMillan, London, 1973).